This is to certify that the

dissertation entitled

"The Island-To-Percolation Transition
During Growth of Metal Films"

presented by

George William Jeffers, Jr.

has been accepted towards fulfillment
of the requirements for

Ph.D. degree in Physics

M. Dubson
Major professor

Date 10/24/94

THE ISLAND - TO - PERCOLATION TRANSITION DURING GROWTH OF METAL FILMS

By

George William Jeffers, Jr.

A DISSERTATION

Submitted to
Michigan State University
in partial fulfillment of the requirements
for the degree of

DOCTOR OF PHILOSOPHY

Department of Physics and Astronomy

1994

ABSTRACT

THE ISLAND - TO - PERCOLATION TRANSITION DURING GROWTH OF METAL FILMS

By

George William Jeffers, Jr.

The formation of percolating Pb films thermally evaporated onto SiO_2 substrates has been experimentally studied using electron microscopy. Pb does not wet SiO_2 so that compact, three-dimensional islands are formed during the initial stages of film growth. As these islands grow in size they eventually touch their neighbors and coalesce due to surface diffusion. Islands smaller than a critical radius, R_c, fully coalesce and form a single island with a compact shape. However, islands larger than this critical radius undergo a partial coalescence to form an elongated island. This crossover to partial coalescence produces a network of connected metal structures which increase in size until the percolation threshold is crossed. The main topics studied in this work are: 1) the film's area coverage at the percolation threshold, p_c, is often quite high ($p_c \gtrsim 80\%$) and 2) the factors controlling the size at which the crossover from full to partial coalescence occurs. The high values of p_c result from the combination of wiping during coalescence and the coalescence crossover which cause the larger droplets to effectively repel one another. The coalescence crossover is described by a Kinetic Freezing Model in which the crossover is due to a competition between the time for two touching islands to coalesce and the time for one of the islands to grow in size, due to continuing deposition, and make contact with a neighboring island. The predictions of this model are tested and some of the absent features are discussed.

Computer simulations of the profile decay of a corrugated crystalline surface due to surface diffusion are also investigated. A fast Monte Carlo algorithm is used to solve a (1+1)D system at low temperature. The results are significantly different than those predicted by the high-temperature continuum model.

To my family

ACKNOWLEDGMENTS

I would like to thank my advisor, Michael Dubson, for his advice and guidance during the course of this research. His knowledge and interest in physics and science in general have helped me to learn much over the last number of years.

Professor Phillip M. Duxbury and his graduate student, Xinhua Yu, have provided much in the way of theoretical justification dealing with this research.

I am thankful to my fellow labmates for much help in both research and non-research related matters as well as making the lab a friendly environment. These people are: Jeeseong Hwang, Evstatin Krastev, Lowell McCann, Richard Smalley, David Wollman, and Qifu Zhu.

Many of my fondest memories of graduate school at MSU involve the network of students and staff who helped one another maintain our respective levels of sanity while learning some physics at the same time. Most notable of this group are: Glenn Alers, Erik Hendrickson, Lilian Hoines, Mike Jaeger, Shang-Fan Lee, Ninamarie Levinsky, Catherine Mader, Paul "Rooster" McConville, Carl "Spike" Nelson, Raman Pfaff, and Mike Wilson.

I also wish to thank a small group of friends who were among the most important in my adjustment to MSU. Many enjoyable times were had with Crystal Cheatham, Kathy McCloud, and Geri Palka. I owe special thanks to Kathy McCloud for many reasons. Her love and support both during and after her time here at MSU have had a major impact on my life. Her presence in my life has profoundly affected my perception and understanding of life and people. Kathy will always occupy a special place in my heart and to her I extend my thanks, appreciation, and love.

Erik Hendrickson and Rooster McConville deserve extra acknowledgment for their support as friends, roommates, and colleagues. Their tolerance of my sometimes eccentric behavior has been greatly appreciated. Together we had a unique balance of work and play. For constant calming of my nerves I am indebted to Dirk, Lerxt, and Pratt.

Thanks are due Professors Norman O. Birge, Eugene Capriotti, Phillip M. Duxbury, and Michael R. Thoennessen for serving on my Guidance Committee.

For their skill, advice, and humor I am thankful to the staff of the PA Machine Shop staff: Tom Palazzolo, Tom Hudson, and Jim Muns. I am thankful to Stephanie Holland for her willingness to assist us sometimes helpless graduate students and for making our lives in graduate school less worrisome.

My deepest acknowledgments are extended to my parents, brother, and sister. It is largely due to their support throughout my life that I have completed this goal.

Finally, this work was supported by The MSU Physics and Astronomy Department, The MSU Center for Fundamental Materials Research, The National Science Foundation under Grant No. DMR-8857364, and by the Donors of The Petroleum Research Fund, administered by the American Chemical Society.

TABLE OF CONTENTS

LIST OF FIGURES

CHAPTER 1

INTRODUCTION

Background and outline of thesis

Surface diffusion plays the determining role in many areas of materials physics. The process of surface diffusion refers to the random migration of single atoms or clusters of atoms amongst the binding sites on a surface. This occurs during both the growth and decay of metallic structures and is the dominant mode of mass transfer for temperatures significantly below the melting temperature. Currently, a complete understanding of the surface diffusion process is lacking.

There is presently much activity, both experimentally and theoretically, directed at elucidating the role, and possible control, of surface diffusion. Much of this effort is centered on the growth of epitaxial films via Molecular Beam Epitaxy. These ultrathin films may be exploited to form electronic devices as well as formation of well-defined multilayered samples. The quality and roughness of these layers and interfaces is often determined by surface diffusion. However, surface diffusion plays a dominant role throughout the growth of metallic films. During growth of a metal film, surface diffusion effects the interaction of the incident vapor atoms with both the bare substrate and already existing deposit. This is particularly true when, during the course of growth, small islands of either metal or liquid deposit come into contact.

However, epitaxial film growth is the exception rather than the rule. Quite often, the deposit and substrate form a non-wetting system. That is, the deposit forms three-dimensional structures on the substrate rather than growing as successive monolayers. In such a case, the film proceeds through the following growth stages. The smaller, three-dimensional islands grow in size until contact is made with similar islands nearby. At this point the touching droplets either fully coalesce and maintain their compact nature, or they

partially coalesce and result in an elongated metal structure. Which coalescence behavior results depends on the size of the touching islands. In the partial coalescence case, a network of islands results which has a high degree of lateral connectivity. Electrical conduction across the sample becomes possible at the percolation threshold. With continuing deposition, the sample fills in any remaining empty channels and quickly completes formation of a continuous, hole-free film. The sequence just described generally occurs for metals deposited onto insulating substrates.

The stage of film growth near the point where a percolating structure occurs, is discussed in the bulk of this thesis. While much work has previously been performed by many groups regarding the initial nucleation and early stages of film growth, less work has concerned the intermediate to late stages of growth. The research described herein deals with the coalescence and percolation regimes just prior to the formation of a continuous film. The experimental techniques used are discussed in Chapter 2. Nucleation is not dealt with for two reasons. First, the features to be discussed occur well after initial island nucleation. Secondly, the experimental equipment used offers insufficient resolution to accurately study island sizes and densities near the onset of film growth.

There are two main features which will be discussed in relation to film growth. The first is the fact that when metal films deposited on insulating substrates form an electrically conducting structure there is an anomalously high metal coverage on the substrate. This area coverage, p_c, is the fraction of substrate covered by deposited metal. The coverages observed are substantially higher than the values predicted by a wide variety of numerical simulations of film growth. The second feature is the existence of a crossover in the structure of the film. Prior to this crossover the film contains many isolated, compact crystallites of deposit material. After the crossover the film contains many elongated, intermingling metal structures which form a connected, percolating structure. This crossover is signaled by a change in the coalescence behavior of two touching droplets. Smaller islands fully coalesce and maintain their compact appearance.

However, the larger islands only partially coalesce, thus forming structures which have an oblong shape. Many of these randomly oriented structures result in the percolating structure. In Chapter 3, I discuss these observations and simple models, the Interrupted Coalescence Model (ICM) and Kinetic Freezing Model (KFM), are presented which qualitatively explain these coupled features.

Our models explaining the large area coverage at percolation and the coalescence crossover are incomplete. Factors are absent which are believed to be very important to a thorough understanding of the growth process. Chapter 4 contains some thoughts on possible experiments which could be performed to quantify certain of these growth influences. One main effect on the film growth is the influence of any topological or chemical inhomogeneity of the substrate. This may result from either physical damage (such as scratching or ion bombardment of the substrate) or contamination of the substrate surface. The second important ingredient missing from the Kinetic Freezing Model discussed in Chapter 3 is the effect of grain boundaries which are known to be trapped within the interior of two coalescing islands. These grain boundaries are observed in all films which are past the crossover from full to partial coalescence.

Finally, extensive computer simulations, detailed in Chapter 5, were performed to study the effects of surface diffusion on the decay of a corrugated surface structure. For a given profile shape, there is only one adjustable parameter in these simulations, the step edge reflection coefficient, k. This temperature dependent parameter accounts for the asymmetry in the potential energy on a crystal surface near a monatomic step. This parameter alone determines the decay dynamics of the (1+1)D system studied. These simulations possess two unique features over most similar studies. First, these simulations were performed below the roughening temperature. Previously, theoretical and experimental efforts concentrated on the $T > T_{roughening}$ regime. Our results are markedly different than in this higher temperature region. Second, our simulations are novel in the sense that they bypass the normal Monte Carlo algorithm. Movement of

atoms is still random, however, the movement is "instantaneous." Once an atom is selected and given the opportunity to move, its actual movement is based on a specified probability distribution depending upon the atom's environment. The movement of any atom need not be continually followed throughout its entire random walk in moving from the initial to final positions. While many of these simulations required a large amount of computing time, the avoidance of tracking the entire movement yields a large reduction in computational time. The method was applied to a one-dimensional system with height $z = z(x, t)$ with t representing the simulation time. However, extension of this algorithm to three dimensions where $z = z(x, y, t)$ is not straightforward since each activated atom has a complicated terrain in which to move. Calculation of the relative probabilities in such a case is very complicated in analogy to the difficulty in calculating the resistance between any two points on a planar random resistor network.

CHAPTER 2

EXPERIMENTAL EQUIPMENT AND METHODS
Sample preparation, observation, and analysis

2.1 INTRODUCTION

In this chapter I will discuss the experimental details used in sample preparation, sample observation, image acquisition, and image analysis. A slightly modified commercial thermal evaporation system, described in Section 2.2, was used to deposit thin films of metal as outlined in Sections 2.3 and 2.4. Post-deposition annealing and cooling were performed prior to removal from the vacuum chamber. The area coverage and average size of the connected metal islands at percolation, the main quantities of interest, were obtained from Scanning Electron Microscope (SEM) images using the image digitization technique described in Section 2.6. The digitized images were analyzed, using programs written in the QuickBASIC programming language. The analysis procedure will be discussed in Section 2.7.

2.2 THERMAL EVAPORATION SYSTEM

Many different techniques exist for producing thin films of metallic, insulating, magnetic, and superconducting materials. The simplest and perhaps oldest of these methods is thermal evaporation. The basic idea of this method is that the material to be deposited is heated to a temperature to cause significant evaporation. When performed in a chamber where the pressure is low enough that the mean free path of the evaporated material is comparable to, or larger than, the source to sample distance, the evaporated material travels ballistically and will condense upon the substrate (the material which the

sample is grown on). This condensation process clearly depends on such parameters as: chamber pressure, supersaturation of the vapor above the substrate (related to the deposition rate), substrate material, and substrate temperature. In subsequent sections of this chapter, details of the experimental control of these parameters will be described.

All samples to be discussed in this thesis were prepared via thermal evaporation in our deposition system [EDWA] which is shown in Figure 2.1. As there are many elements to this system, the following paragraphs will describe these individually.

The source of metal to be deposited (in wire or pellet form) rests in the dimple of a high melting point metal (generally W or Mo) boat [MATH]. Passage of a large current, generally in the range 50 to 100 amps through the boat results in Joule heating sufficient to evaporate the metal in the boat, but not the boat itself. This current and, hence, the source temperature and deposition rate, are manually controlled using a variable transformer connected to the metal boat. Care must be taken so that the boat and metal do not form an alloy (such as in the case of Al and W) which would result in a film of unknown stoichiometry. As the films to be discussed were Pb, a W boat was used for which alloying was not relevant [HANS58]. Other sources of heat to evaporate the deposit, such as a crucible (boron nitride or quartz), which sits in and is heated by a wire basket, may also be used. This technique is possible with Pb due to the low melting point of Pb. Higher melting point materials are more difficult to deposit using a crucible setup due to a poor thermal link between the wire basket and the crucible. Our source holds enough Pb so that up to five samples, of varying thicknesses, could be prepared in one pumpdown cycle without breaking vacuum. One problem encountered with our sources was stability of the deposition rate. The deposition rate was generally constant to within roughly 5%. These fluctuations could often be lowered by means of a longer pre-melt of the deposit during steadying of the deposition rate. An enclosed, isothermal effusion crucible cell source (Knudsen cell) offering extreme deposition rate control could also have been used. Efforts to construct such a cell will be mentioned in Chapter 4.

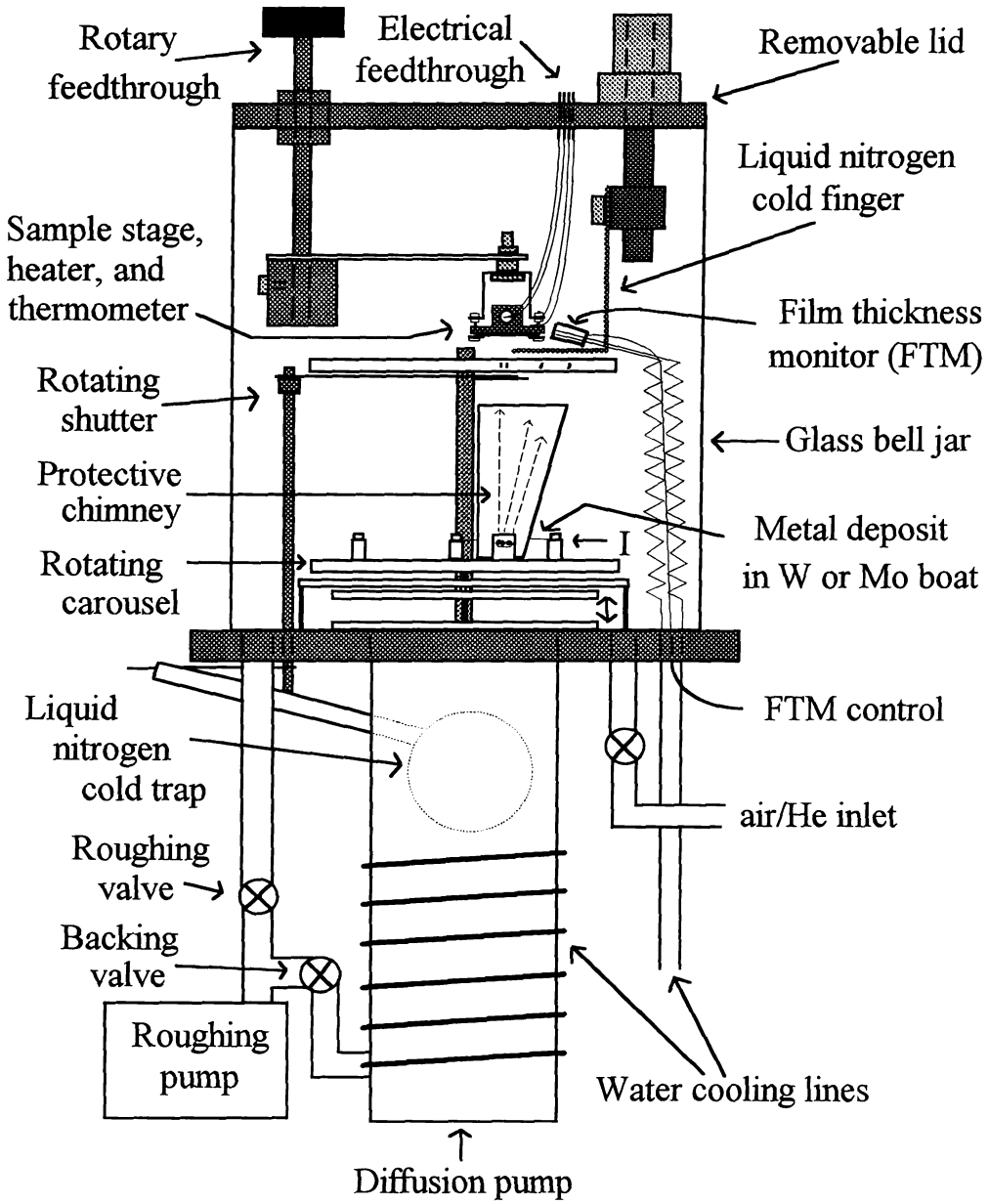

Figure 2.1 Diagram of thermal evaporation system, described in the text, used in sample preparation. Diagram is not drawn to scale.

One difficulty associated with thermal sources is that the high temperatures required to evaporate the deposit metal also heat regions of the evaporator near the source. The outgassing of these heated parts causes a pressure rise in the chamber. Depending upon the composition and cleanliness of these nearby surfaces, foreign species may be desorbed and integrated into the sample. This might happen if, for example, following the deposition of a low melting point material, a high melting point material was evaporated from the same position. To minimize contamination of the vacuum chamber and samples, Pb films were prepared with the source surrounded by an Al sheet metal chimney extending to just below the sample. This chimney restricts the evaporated deposit to only strike the sample and film thickness monitor. Additionally, the area directly below the source was covered with Al foil. These simple measures served the dual purpose of shielding the sample from stray material as well as covering the nearby surfaces from being coated with Pb, which has a fairly low melting temperature of $T_M = 601\ K = 328\ °C$.

A film thickness monitor (FTM) is used to measure the deposition rate and total film thickness during deposition. A FTM consists of a vibrating piece of quartz which has its resonant frequency changed due to adsorption of material upon its surface, similar to a mass on a spring. This measured frequency shift is combined with parameters (density and acoustic impedance) of the deposit material and a geometry factor (to account for the position of the FTM relative to the sample) to yield the deposition rate and total thickness. Most thicknesses quoted in this thesis are nominal thicknesses. That is, they are generally correct *relative to one another.* The absolute thickness, however, is only known to an accuracy of roughly five to ten percent. The Physics and Astronomy Department has a surface profilometer [SLOA] which was used to measure some film thicknesses and calibrate the FTM. This apparatus operates by moving a sharp stylus of radius $\sim 5\ \mu m$ over the surface to be measured and recording the vertical deflection. However, because Pb is a very soft material the stylus tends to "plow" into the Pb, resulting in meaningless

thickness measurements. The FTM was, however, calibrated by depositing harder materials such as Ag in the same geometry and measuring their thicknesses with the profilometer. However, as our evaporation system was often used by people who required different sample geometries from my own, the FTM was repeatedly moved. While care was taken during setup to return the FTM to the same position, thickness variations undoubtedly existed from run to run. As a check on the calibration of the FTM, several films were viewed "edge on" in the Scanning Electron Microscope (SEM) with a resolution of 10 to 20 nm. This method, where the sample is viewed with the incident electron beam parallel to the substrate plane, allows determination of the average film thickness. To do this, samples were either tilted or the substrate is cleaved through the sample spot and mounted vertically inside the SEM. Thicknesses measured in this fashion were found to be within roughly 20% of the indicated thickness using the FTM. This 20% discrepancy is partly due to the uncertainty in determining the average thickness of a discontinuous film when viewed "edge-on."

The pumping system on our thermal evaporator consists of a rotary vane mechanical pump and a diffusion pump. The mechanical pump serves two purposes: initial pumping of the chamber (from atmosphere down to $\sim 5 \times 10^{-3}$ mbar) and backing of the diffusion pump. The diffusion pump is equipped with a "cold trap" which could be filled with liquid nitrogen (LN_2) to prevent backstreaming of pump oil into the chamber. Typical base pressures prior to deposition were in the low to mid 10^{-7} mbar range. Often, the pressure was less than the 10^{-7} mbar lower limit of the Penning pressure gauge.

Prior to sample deposition, the source was outgassed during the process of setting the deposition rate. This process of steadying the deposition rate generally took about five minutes. After degassing the source, the deposition took place in a vacuum of 5×10^{-7} to 5×10^{-6} mbar. The "cold trap" was always filled prior to, and during, sample deposition in order to reduce sample contamination from hydrocarbons present in the pump oil and other compounds in the chamber.

Nearly all of the samples were prepared while mounted on a substrate holder/heater stage suspended from a rotary feedthrough in the removable lid of the evaporation system. The heatable sample holder will be described below. The rotary feedthrough enables preparation of multiple samples during one pumpdown and deposition cycle. Samples consist of small (≈3 mm diameter) spots on substrates to be detailed further in Section 2.3. Roughly 10 cm directly above the source is located an Al plate with a small aperture defining the sample pattern. The substrate holder is located about 1 cm above this aperture. Due to the separation of the aperture and the substrate, the samples have a thickness gradient. The thickness profile is such that the average quoted thickness occurs at the center of the sample and decreased monotonically to zero along a radius of the sample spot. This "shadow effect" occurs because different positions on the substrate are exposed to varying amounts of the source. The advantage of this scheme is that for most samples *all stages of growth were present on the same sample*. That is, different portions of the sample range from zero thickness up to a percolating region near the center of the spot. In Section 2.5 this useful feature will be exploited.

A diagram of the heatable substrate holder is shown in Figure 2.2. Substrates are clamped to the smoothed surface of a Cu block which has a resistive heater inside and a Pt resistance thermometer on the surface. The heater is a 35 W resistive cartridge heater which is more than adequate to reach the desired sample temperatures. The Cu block, with a mass of 50 g, may be heated to roughly 675 K with 7 W of power. The block was designed such that the heater-to-block contact could be tightened prior to every sample preparation to ensure a good thermal link between the heater and sample stage. The thermometer, a Pt Thin Film Detector (TFD) [OMEG], was also routinely tightened to the Cu block's surface by pressure from a stiff stainless steel clip. The sample temperature was monitored and controlled by a standard temperature controller [LAKE] which allows temperature control to much better than 1 K. Two terminal measurements of the thermometer's resistance are adequate as the lead resistance corresponds to less than 1 K.

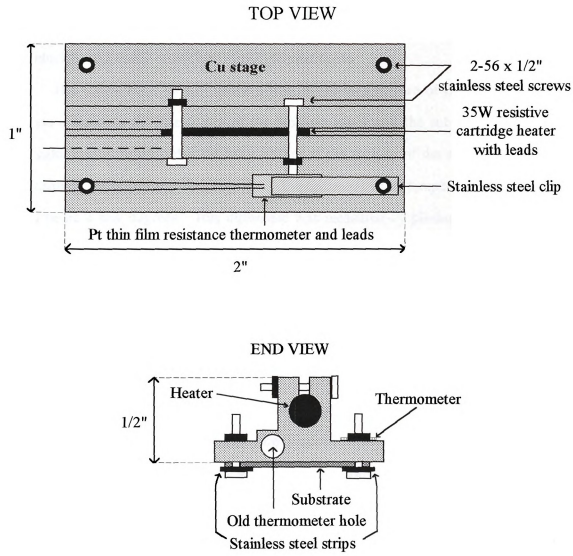

Figure 2.2 Diagram of heatable Cu substrate stage.

The sample is mounted to the Cu block by two stiff stainless steel bars which are tightened against the sample to push it into contact with the heated block. These practices of ensuring good heater, thermometer, and sample contact to the sample stage were a result of early problems encountered with the stability and reproducibility of the sample temperature during and after deposition. The above design was found to yield reproducible and easily controlled sample temperatures.

The temperature of real concern here is the temperature of the *substrate surface* because it governs the interaction of the incident vapor and the substrate. Simple heat flow calculations indicate that the temperature of the surface of the substrate and the Cu block should differ by much less than 1 K. Experimentally this temperature difference was found to be a few degrees. This difference was measured by placing two TFD's on the sample stage. One TFD was placed on the surface of the Cu block while the second TFD was located atop the substrate, and their resistance's were measured simultaneously during heating and cooling.

Since the substrate temperature is so important, it is necessary to make sure that the temperature is stable during sample deposition. A plot of substrate surface temperature increase due to radiative heating caused by exposure to a heated, empty boat is shown in Figure 2.3. It can be seen from Figure 2.3 that the incident radiation from the empty boat has a small effect on the sample temperature. A similar test with metal deposit incident upon the substrate was also performed. The temperature rise in this case was roughly the same as for the case of an empty boat in agreement with calculations of the heating due to the incident metal vapor. Thus, the sample temperature during deposition was constant to within ≈ 5 K.

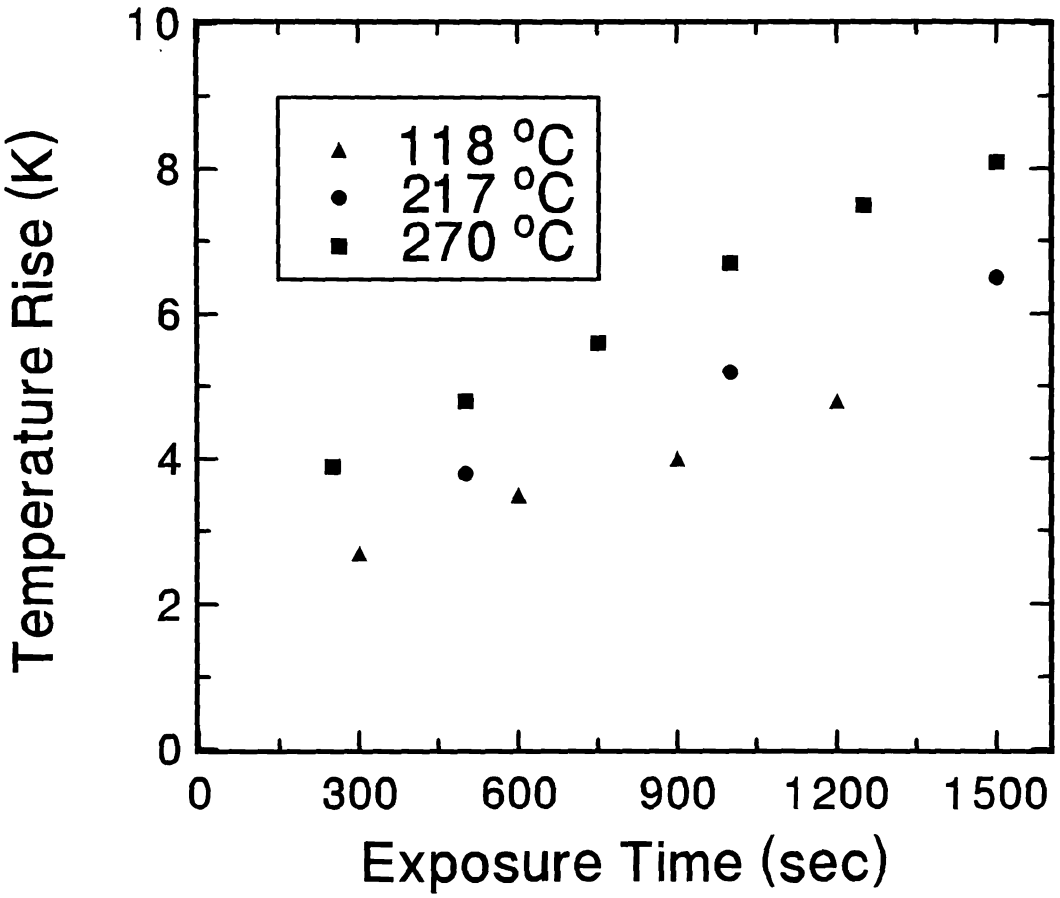

Figure 2.3 Substrate temperature rise due to exposure to a heated, empty evaporation boat. The different traces correspond to different substrate temperatures at time zero as shown in the legend.

Mounted inside the chamber, near the sample, is a "cold finger" consisting of a Cu block connected to a LN_2 reservoir. This "cold finger" is used for cooling samples following deposition and as a small cryopump near the sample. Because the sample morphology is very sensitive to the rate of sample cooling following deposition, the "cold finger" is used primarily for the former purpose. In early experiments, samples were allowed to cool via radiation, in vacuum, by turning off the heater's power supply. This resulted in a cooling rate of about 1 K/minute. This slow cooling rate allowed the samples to anneal as will be discussed further in Chapter 3. To achieve a faster cooling rate, a new method of cooling was implemented. Immediately after deposition, the hot sample block was rotated over the LN_2 cooled "cold finger." Within a few seconds of this, the source power was terminated, the diffusion pump isolated from the chamber, and the chamber backfilled with He_2 gas to a pressure of roughly 10^{-3} mbar. The presence of the He_2 gas, which has a very high thermal conductivity, provides a good thermal link between the hot Cu block and the "cold finger." The separation of the sample block and the cooled surface was roughly 1 cm, which is approximately the mean free path at 10^{-3} mbar. This simple scheme increased the cooling rate to roughly 20 K/minute. This increased cooling rate produced a dramatic change in the sample morphology as will be discussed in Section 3.3. Once the samples were cooled to near room temperature (about 10 to 20 minutes after the "quench" began), the chamber was vented with N_2 gas and the samples removed. Since Pb oxidizes rapidly, exposure of the samples to air resulted in the rapid growth of a native oxide which "freezes in" the morphology and prevents any further evolution of the film morphology. During deposition, the "cold finger" was cooled with LN_2 and located near the sample to act as a cryopump. Because of this, the chamber pressure fell. However, the pressure (and hence the contamination rate) near the sample were decreased by an unknown amount.

2.3 SUBSTRATE PREPARATION

The substrates used were single crystal Si wafers with a thin native oxide of amorphous SiO_2. Substrates were cleaved from p-type Si (100) wafers [ZITI] with the following characteristics: test grade, resistivity of 14 – 22 $\Omega \cdot cm$, and a thickness of 19 – 21 mils. Optical ellipsometry [OHRI92] was performed, in the Michigan State University Engineering Department, on a bare substrate to determine the amorphous SiO_2 layer thickness. This thickness was found to be roughly 3.5 – 4.0 nm. Another test piece was imaged using an Atomic Force Microscope [AFM] in the Center For Electron Optics at Michigan State University. The rms roughness, according to the AFM image, was 0.1 nm. Since we were interested in metal on insulator growth no attempt was made to remove the amorphous oxide layer. Two identical samples were grown on Si (100) and Si (111) with the results (both qualitatively and quantitatively) being indistinguishable. Thus, it is only the insulating layer which controls the morphology and not the structure of the underlying semiconducting substrate. For instance, any effects such as strain at the Si surface are invisible to the deposit due to the presence of the oxide layer. Glass slides cannot be used as substrates since an electrically conducting substrate is needed to allow sample viewing with an SEM. An insulating all-glass substrate would become charged under the electron beam. However, the insulating oxide layer on our Si wafers was thin enough to be transparent to the high energy incident electron beam.

The substrates were carefully cleaned, after cleavage, without removing the oxide, according to the following procedure:

- Rinse in acetone
- Ultrasonic cleaning in acetone for roughly 2 minutes
- Rinse in methyl alcohol
- Rinse in de ionized water
- Soak in hot MICRO [MICRO] for 10 minutes at above 80 °C

- Rinse repeatedly with de ionized water to remove the MICRO cleaner
- Dry with N_2 gas and optically inspect for signs of debris
- One of two final steps before insertion in the vacuum chamber
    a) Pass through the flame of a Bunsen burner to remove residual organic contaminants
    b) Place in a UV/ozone cleaner for 10 to 15 minutes

After cleaning, the samples were mounted on the sample stage and placed in the vacuum chamber as soon as possible. This was generally five minutes or so after the flame or UV/ozone cleaning step was completed. The flame cleaning and the UV/ozone cleaning methods produced films which were nearly identical in appearance when viewed with both the naked eye and the SEM. As it was faster and easier, the flaming method was usually employed. Once the substrates were in vacuum and the chamber pressure below about 10^{-5} mbar, the heater was turned on and the substrate was heated to near 675 K for anywhere from 2 to 12 hours. The SiO_2 layer is stable to far higher temperatures. The duration of this bake cycle had no effect upon the resultant films. Thus, it was reduced to roughly 2 hours in the interests of saving time. This was the final substrate cleaning step prior to film deposition.

Surface contamination is a very important issue in surface controlled processes. Unfortunately, we have no *in situ* surface analytical equipment, such as Auger Electron Spectroscopy or a residual gas analyzer with which to characterize the surface contamination present on the samples. Our only estimate of contamination is based on the pressure during deposition and sample appearance from visual and SEM inspection.

2.4 FILM DEPOSITION

Following the substrate preparation procedure outlined in Section 2.3 the sample temperature is lowered to the desired deposition temperature a couple of hours prior to film deposition. These few hours are needed to allow the heater stage to cool to the

deposition temperature. This deposition temperature range was 300 K (room temperature) to 500 K. This highest temperature is 83% of the bulk melting temperature, 601 K, of Pb. After allowing the sample to achieve the desired temperature, setting the FTM parameters, and degassing of the source (Pb, In, or Sn usually), the sample was ready to be prepared. By moving a shutter the substrate is exposed to the molten metal source. The substrate is exposed to the deposit until the desired sample thickness is obtained. After deposition, or after a post-deposition annealing, the samples were quench cooled as described in Section 2.2. For most samples, the deposition rate was a constant value between 0.2 nm/s and 20 nm/s and the total thickness was generally 100 to 4000 nm. Thus, the total deposition time was usually between ten seconds and ten minutes for each sample. During all sample preparations the deposition rate was held nearly constant. Variations often occurred, but the average deposition rate was usually within about five percent of the desired value. A complete sample preparation cycle typically required between six and sixteen hours depending upon the time necessary to achieve a satisfactory vacuum in the evaporation chamber.

Depending upon the thicknesses, up to five samples could be prepared in one pumpdown cycle with control over the temperature and deposition rate of the individual sample spots. The size of the substrate and the need to have all the samples on a single substrate, yet separated from one another, limited the number of samples per run. Before the importance of the sample cooling rate was realized, several samples were prepared on one substrate at differing temperatures. This was accomplished by depositing the highest temperature sample, cooling to the next highest temperature, depositing sample number two, and so on. While feasible, this method proved unsatisfactory because of the effective annealing due to the slow cooling already mentioned. Thus, few of these results will be mentioned. Once samples began being prepared using the He_2 gas "quenching" method, described in Section 2.2, all the samples prepared in a single pumpdown were prepared at the same temperature. By holding the deposition temperature constant, the parameter

varied in such sample sequences is the annealing time following deposition. The results obtained from samples prepared in this manner will be discussed in Chapter 3.

Sample thicknesses were chosen so that the center of the film was slightly past percolation and the percolation threshold occurred just off-center of the sample. These thicknesses, generally found by trial and error, were nominally 100 nm to 150 nm for Pb on a 300 K substrate and roughly 4000 nm or more for substrates above 475 K. Typical deposition rates for most samples were 5 to 6 nm/s. To achieve these deposition rates, with the W boats we use, a power of roughly 250 to 500 W of Joule heating in the boat is required.

After cooling the samples to near room temperature, they were removed from the vacuum chamber. If necessary the substrate could be cleaved to separate the samples from one another. In any case, the samples were placed in a desiccator until inserted into the SEM for observation. Samples were also refrigerated after removal from the evaporator and/or after viewing with the SEM to lower any time induced morphology change. With these methods, the appearance of the samples did not change over a period of months.

2.5 SAMPLE OBSERVATION

In this section I will give a brief description of the Scanning Electron Microscope (SEM) used in all sample observations to be discussed. Many factors make the SEM a logical instrument to use in this type of work. Most importantly an SEM allows a wide range of sizes to be investigated with a single instrument. Our instrument, a Model SX-40A manufactured by International Scientific Instruments [ISI], has a resolution of roughly 6 nm, at best, and the maximum field of view is a few millimeters. Equipped with a motorized stage for sample movement, this SEM can effectively map an area of several square centimeters. This feature was especially beneficial when viewing multiple samples

covering the full extent of a single substrate. All such samples could be imaged in one pumpdown cycle. Typical operating parameters were a beam energy of between 15 and 30 keV, a spatial resolution of roughly 10 nm, specimen current ~10 pA, and a working distance of 8 to 10 mm. The SEM is pumped by a mechanical pump and a diffusion pump. The diffusion pump was equipped with an LN_2 cold trap. The base pressure of the instrument was in the high 10^{-6} mbar range.

Usually, observations were made with the plane of the samples perpendicular to the electron beam. This allowed views of the sample along the same direction as the incident vapor flux, which were necessary to determine the percolation and island size values desired. Typically, four images were taken at or near the percolation threshold, of different positions on each sample to obtain "average" information. The location of these pictures was determined visually on the SEM monitor screen. Samples could also be rotated about both the polar and azimuthal axes. The polar rotation ability was especially useful for orienting the substrate plane nearly parallel to the incident electron beam (perpendicular to the incident vapor flux during deposition). Normally these observations were done on samples which had been cleaved after deposition (though sometimes before) to obtain cross-sectional views of the morphology, film thicknesses, and crystallite/substrate contact angles.

This instrument was adequate for routine sample viewing. However, it severely restricted quantitative analysis of the samples. As described in the following sections, this difficulty was overcome via computerized image acquisition and analysis.

2.6 DIGITIZED SEM IMAGE ACQUISITION

The biggest drawback of older, analog SEM's is that they produce analog images, with hard copies in the form of black and white Polaroid photographs. While such pictures are easy to create and store, many disadvantages exist. These photographs limit

analysis to being performed by hand. Another option for image analysis, which we considered until the following method was implemented, was to digitize the Polaroid photographs with a CCD camera and use commercially available analysis packages. These Polaroid pictures are also non-erasable and relatively expensive. Once the picture is exposed, it can't be changed. Thus, any errors in contrast or brightness setting, focus, or astigmatism may result in a useless picture. Our instrument uses Polaroid Type 52 film which costs roughly $1.50 per picture. For these reasons, especially the difficulty of obtaining quantitative information, we implemented a technique to obtain digitized images.

Scanning electron microscopes create images using secondary electrons created in the interaction of the incident electron beam and the sample. After an electron from the incident beam strikes the sample, secondary electrons, with energies less than 50 eV, are emitted from a small region near the surface of the sample. Inside the SEM chamber is a secondary electron detector (SED). This detector consists of a fluorescent material covered by a thin Al film held at a positive 10 kV and a photomultiplier tube. Secondary electrons are attracted to the Al film and upon striking the fluorescent material create one or more photons which are directed down a light pipe onto the photomultiplier tube. Because the number of emitted secondary electrons is related to the tilt of the sample surface relative to the incident beam and not the sample height, SEM micrographs generally lack three dimensional information.

The signal from the SED is used to create identical images on two separate monitor screens. One of these screens is viewed directly by the SEM operator. The second screen is a short persistence monitor inside the SEM console. When a Polaroid photograph is taken, it is of this second screen.

To obtain digitized images we intercept the SED voltage signal between the photomultiplier tube and the photograph screen. This signal is digitized using a 12-bit A/D board [DATA] in a personal computer and stored on diskette [DUBS92]. Care must be taken to sample the signal at the correct frequency so that each image line is

synchronized with its neighboring scan lines. Thus, proper record must be kept for the beginning and end of the image, as well as the start of a new line. A schematic diagram is shown in Figure 2.4.

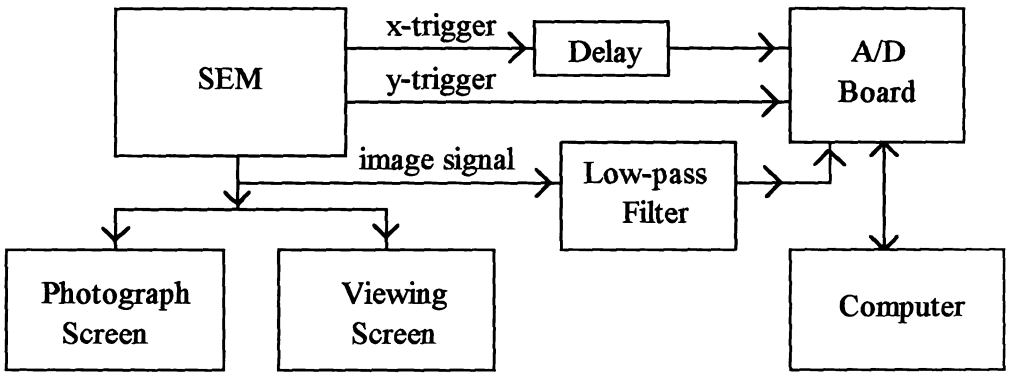

Figure 2.4 Schematic diagram of digitized image acquisition circuit.

When in "photo mode" the SEM produces a 2048 line scan in roughly 70 seconds. This corresponds to a rate of 33 ms/line. The 12-bit A/D board used can digitize points at a rate of up to 20 kHz which corresponds to 512 points in 25.6 ms. This is very convenient given the 33 ms/line scan rate. The A/D board was installed in a 286 class PC, running DOS with 640 kB of RAM. After loading DOS and the QuickBASIC (the programming language used) program in RAM, only enough RAM remained to hold about a 512 (x) by 480 (y) image (at 2 bytes/pixel). This corresponds to an image size of 480 kB. The originally 2048 line scan is cut to 480 lines by ignoring the first 128 lines of the scan and saving the rest of the image in four line bunches. That is, each line in the recorded image is, in fact, the sum of four (of 1920) scan lines. In the horizontal direction, a short (~3 ms) delay is placed at the start of every "new line" trigger. This acts to postpone the recording at the start of each new line. The resulting image is actually a nearly square portion of the originally rectangular image.

As illustrated in Figure 2.4, there are two trigger signals which control when the A/D board is digitizing the SED image signal, which is between −5 V and +5 V. Prior to being digitized by the A/D board, this signal is filtered by a low pass RC filter with a corner frequency of 10 kHz. Because we are sampling at 20 kHz, the *sampling theorem* [PRES86] allows a maximum signal frequency of 10 kHz without loss of information. The y-trigger first signals the start of a new frame for recording. It is this signal which begins the A/D board's digitization after a built in software delay to center the digitized image relative to that displayed on the viewing monitor. The start of a new scan line is signaled by the x-trigger. After the y-delay, the software begins summing four line bundles together before sending this data to the computer's RAM. The y-trigger signal also terminates the digitization process by providing an end of frame signal. The delay box in the schematic acts similarly to the software delay mentioned above. To obtain a digitized image of the center portion of the SEM image a certain amount must be ignored before recording data for each line. This delay box has a maximum delay of roughly 6 ms. A 3 ms delay serves to capture the center image portion. Once the end of frame trigger is received the program is terminated and SEM operation is returned to normal.

Some important computing problems were overcome in the course of developing this digitization technique. The QuickBASIC programming language running on an 8 MHz 286 class PC is too slow to process data produced by the A/D board at 20 kHz. Therefore, the code to record the data to RAM was written in Assembly language. Were the program run on a faster 386 PC or a 486 PC, this might not have been necessary as these machines (16 MHz to 66 MHz) may be quick enough to write the data directly to RAM. Another problem with using QuickBASIC is its difficulty manipulating arrays larger than 64 kB. As the images are 480 kB, this is clearly a problem. To overcome this limitation the image is split into eight segments. The first seven of these segments are 64 kB each with the eighth segment being 32 kB. The benefits of this segmenting are twofold. First, the time required to save the segmented image from RAM to floppy disk

was roughly 15 seconds, compared to the nearly three minutes required when the image was saved as a sequential binary file. Secondly, the bottom portion of the image could easily be ignored when performing the image analysis. The image produced by the SEM contains a region at the bottom which contains image information such as beam accelerating voltage, image magnification, scale bar, and photograph number. This bottom portion of the image must be dropped for analysis purposes.

With images successfully digitized from the SEM and saved on disk, computerized analysis could be performed. An example of such a digitized image of one of my samples is shown in Figure 2.5. Figure 2.5 shows a 400 nm Pb film evaporated on a 423 K substrate at 6 nm/s. The analysis programs used to determine various image properties will be described in the next section.

2.7 IMAGE ANALYSIS PROGRAMS

Simple computer programs written in the QuickBASIC programming language were utilized to extract quantitative information from the digitized SEM images. The original 512 (x) by 480 (y) image was reduced to a size of 510 by 382 for analysis purposes by removing the status bar and a small portion of the image area. The desired information from most images were values for the area coverage of metal on the substrate at percolation and the average width of the connected metal islands. This section will describe these programs.

2.7.1 MEASUREMENT OF p_c

Percolation is the point at which a connected path spans the extent of a sample. This connected path would allow electrical conduction in the case of a thin metal film. The methodology used to obtain images of our samples near the percolation threshold was

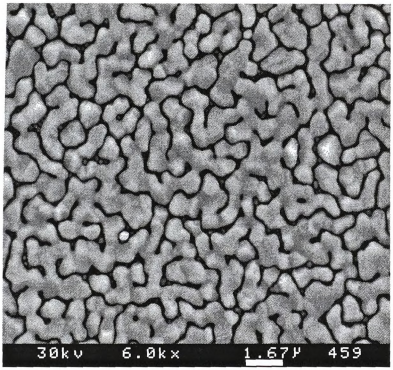

Figure 2.5 Sample digitized image of a 400 nm Pb film on a 423 K substrate using the digitization technique outlined in Section 2.6.

described in Sections 2.5 and 2.6. In order to determine if a connected path exists a criterion is needed to determine if a section belongs to this connected path.

Images were taken near regions of the sample where the percolation threshold had just been reached. Since the samples have a thickness gradient, it is possible to find locations on the sample where the scan area changes from not having a connected path of metal islands to a stage where this path is present. Due to array size limitations, the analysis programs are restricted on how complicated the image can be, in terms of number of occupied pixels and perimeter length of the islands. Thus, after some experience I determined an optimum magnification to use on the SEM depending on the size of the structures being observed Once this magnification was determined, finding image locations was a matter of looking around the sample until a percolating region was located. The actual determination of whether or not a spot was percolating was performed visually. To obtain average results, typically images were taken of four different percolating regions on each sample.

During the digitization process, pixel intensity values from 0 to 4095 are produced. A distinction must be made as to which pixels are part of the metal structure. An intensity histogram of the image enables this distinction to be made. Such a histogram is shown in Figure 2.6. The original image from which this histogram is produced is shown in Figure 2.5. The horizontal axis is pixel intensity grouped into 512 equal bins while the vertical axis is the number of pixels falling within the corresponding intensity bin. The striking feature of this plot is the double peaked structure. This structure is easily understandable in terms of the substrate (low intensity) and the metal deposit (high intensity). Consider a checkerboard where all squares are of two different colors. The intensity histogram of such a structure consists of two peaks, one at the intensity of each color. In the real images, however, these peaks are spread out due to the range of intensities near each peak. In addition to black (the substrate) there are light grays, dark grays, etc.... The horizontal scale is set with intensity bins 0 and 511 determined by the minimum and

maximum pixel intensities in the image. Using this histogram, it is easy to set a criterion for separating substrate from deposit. This is conveniently done by setting a threshold at the minimum intensity bin, as indicated by the arrow in Figure 2.6, lying between the two peaks. This threshold is used to convert the image into a binary image. Such a binary image is shown in Figure 2.7 which is created from the original SEM image in Figure 2.5. Pixels with intensity larger than the threshold setting are automatically set to a value of one (deposit) while those pixels with intensities below the threshold setting are set to zero (substrate). In Figure 2.7 black sites represent the deposit. The resulting two color image is used for subsequent analysis.

Before further analysis, single pixel noise in the images is eliminated. If a pixel is assigned value zero (unoccupied) in the binary image but has four nearest neighbors which are all value one (occupied), this lone pixel is changed to be occupied. The opposite of this is handled as well.

A simple counting of occupied pixels is then used to determine the area coverage p_c. The coverage at percolation, p_c, is defined as the number of occupied pixels divided by the total number of pixels in the image. A quoted value of p_c for a given sample is the average coverage determined from two to four different images of the same sample, taken at various positions on the sample.

2.7.2 DETERMINATION OF ISLAND WIDTH R_c

We define R_c as the average half width of the metal islands near the percolation threshold. This dimension is close to the radius of compact islands at the full to partial coalescence crossover. More importantly, this is a consistent, reproducible criterion for R_c. With the binary image resulting from the determination of p_c this quantity is easy to measure. The determination of R_c relies on the use of the well-known "forest fire" or "tree burning" algorithm.

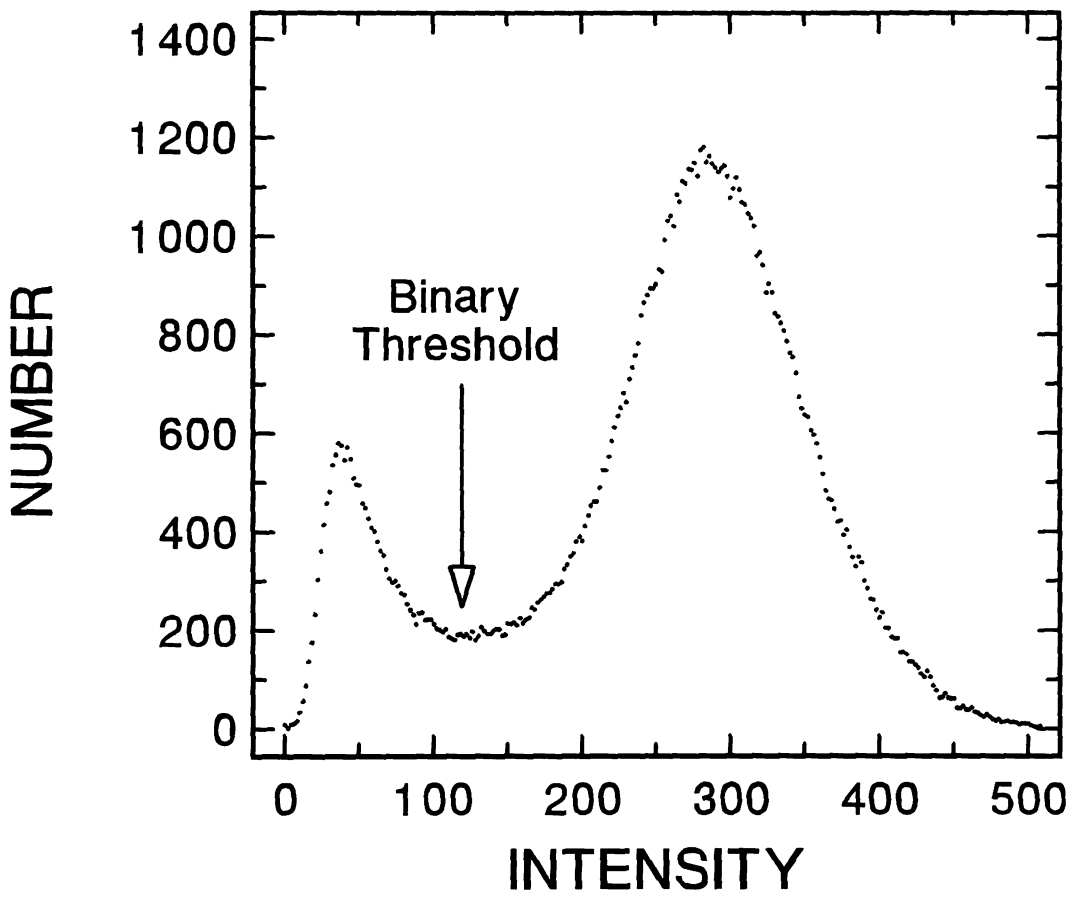

Figure 2.6 Intensity histogram for the Pb sample shown in Figure 2.5. The arrow determines the threshold for creating a binary image.

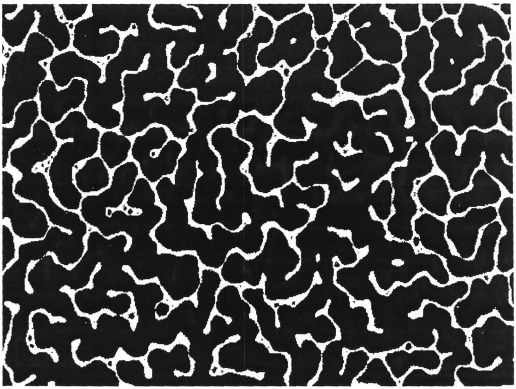

Figure 2.7 Binary image of the top 384 lines of Figure 2.5 using the intensity histogram shown in Figure 2.6.

Beginning with the binary image the perimeter of the connected metal structures must be found. This is done by checking every occupied pixel in the image for the following condition: are there one, two, or three occupied nearest neighbors? If this condition is true, the selected site is a perimeter site and its pixel value changed to three. Having one occupied nearest neighbor assures the site belongs to a cluster, while it must have less than four occupied neighbors to ensure the site is located on an island perimeter. This step results in selection of all the sites lying along the cluster perimeters.

The R_c determination is based upon counting the number of cycles needed for the perimeters to "burn" the metal islands. After setting the perimeter on fire, as described in the previous paragraph, a cycle consists of the following sequence. Pixels are labeled as unoccupied (pixel value 0), occupied and "unburnt" (value 1), "burning" (value 3) or "burnt" (value 0). In each cycle of the fire, pixels which are burning become burnt, and unburnt pixels become burning. This cycle continues until all unburnt sites become burnt. Since, from our determination of p_c, we know the total number of occupied sites to begin with, we merely need monitor the number of these sites which are burnt during each subsequent cycle. From this information we may form a consistent definition of R_c. A plot of the percentage of burned sites versus cycle number is shown in Figure 2.8. The conversion from cycle number to physical distance in the real film is accomplished by knowing the magnification of the original image. This information is specified in the status bar area which is created with every SEM image. This relation between pixel distance and physical distance is: 1 pixel = [170.8/(image magnification)] μm. The condition used to define R_c is when 95% of the occupied sites have been burned by the forest fire as indicated by the intersection of the two solid lines shown in Figure 2.8. The interpolated cycle number at this point is converted to a physical distance and set equal to R_c.

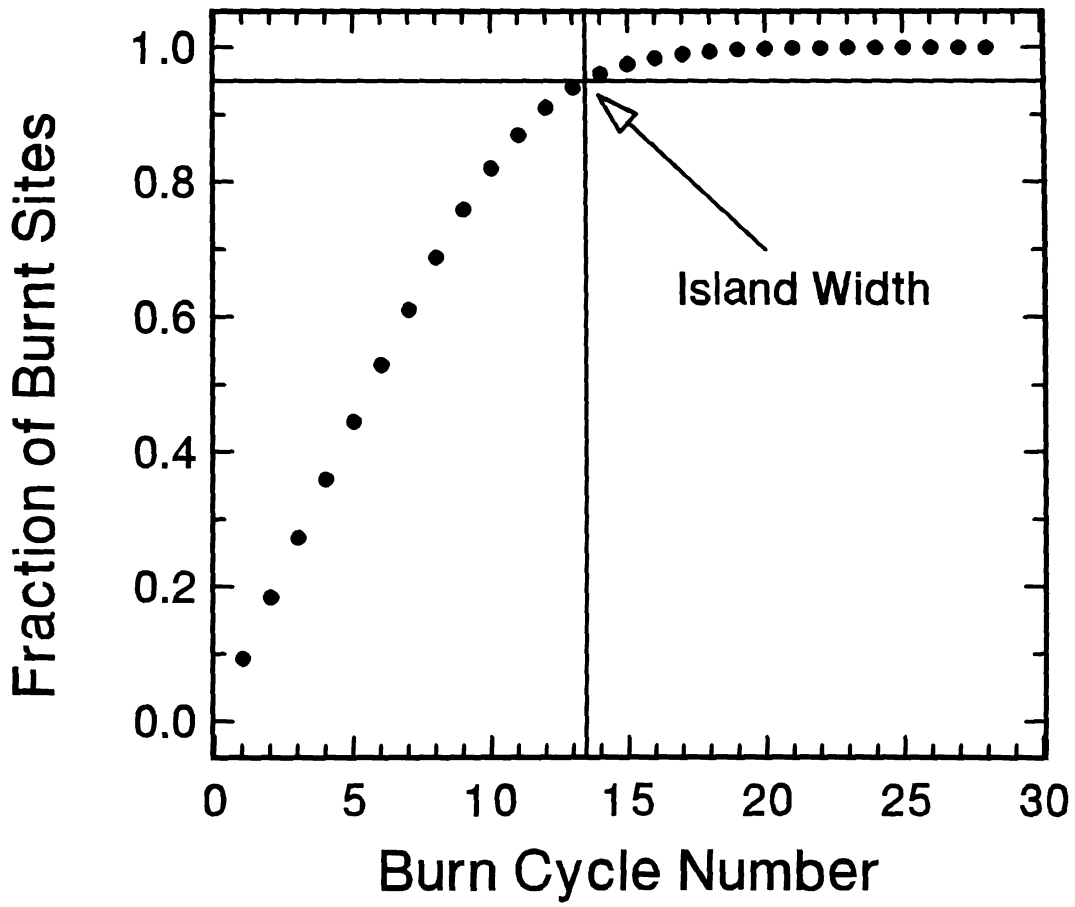

Figure 2.8 Percent of sites burned during the forest fire algorithm vs. cycle number for the binary image shown in Figure 2.7.

2.7.3 COMPRESSION PROGRAMS

Although the raw binary image files are 480 kB, this size may be reduced by a factor of roughly six, by saving the image in a different file format, for archival purposes. Once the image is saved to floppy disk it may be easily read into various QuickBASIC programs. Once the image is displayed on a VGA color monitor, commercial programs called GRABSCRN and RAW2GIF [GRAB] are used to convert the screen image into a GIF file. GIF refers to a standard image file format. The GRABSCRN program effectively takes a raw "snapshot" of the computer monitor (actually the video memory). This raw monitor image information is converted to the GIF format using the RAW2GIF program. Once in this standard format, the image can be read into a desktop publishing program (we use Publisher's Paintbrush [PUBP]). Such a program has image editing capabilities as well as the ability to print high quality images on a compatible printer. In our case, the printer used was a Hewlett-Packard [HEWL] HP4 laser printer. This software/printer combination produces 600 dpi publication quality images.

Using these methods the original SEM images are obtained in hard copy form and as a roughly 80 kB file. For archival purposes and later analysis, the original image files are also saved to floppy disk. This is because, without knowing the compression format used by GIF files, the original images cannot be fully reconstructed from the compressed files. Even if the GIF format were known, some image information might be lost during image reconstruction.

2.8 SUMMARY

In this chapter I have discussed all aspects of sample preparation relevant to the results to be presented and discussed in Chapter 3 of this thesis. Although the experimental techniques used are not overly complicated or difficult, significant problems

were encountered. The most important of these problems were: rapid sample cooling, obtaining quantitative information from the samples, and production of high quality image output for both storage and hard copy production. These obstacles required a non-trivial amount of time and effort to overcome.

The importance of sample annealing due to slow sample cooling is one which should have been appreciated earlier in the course of this research. However, once this effect was realized, a very simple solution was instituted. The sample was "quench cooled" at a selected time after deposition was completed. The simple method used involved heater power termination, vacuum chamber isolation, and the high thermal conductivity of He_2 gas at a pressure of roughly 10^{-3} mbar. This technique is described in Section 2.2 and its results will be discussed in Chapter 3. This improvement in sample preparation produced reliable and reproducible results.

Overcoming the difficulties inherent in the Polaroid photographs produced by our SEM was a major advancement for the purposes of this research. As described in Section 2.6 the technique employed was direct digitization of the secondary electron detector signal and recording of this output to computer. Not only did this method allow subsequent computerized analysis, as outlined in Section 2.7, but the throughput of image production increased. Images were created, quantitatively analyzed, and printed in a matter of minutes. The beauty of this arrangement is that all of the components used were either already present or produced here in our laboratory. Qifu Zhu handled perhaps the most difficult portion of implementing this technique -- coding of the Assembly language program needed to record data quickly enough.

Some of the experimental difficulties present in this research will be further discussed in Chapter 4. Chapter 4 will deal with some of our planned remedies to various problems encountered as well as future directions of this research which could be pursued. Since the stage of film growth studied in this research has received little attention previously, the goal was to obtain a qualitative understanding of the physics controlling

the coalescence and percolation of film growth. As the results of Chapter 3 will show, this goal was achieved.

CHAPTER 2 REFERENCES

AFM The AFM used was a Nanoscope III Scanning Probe Microscope by Digital Instruments, 520 Montecito St., Santa Barbara, CA 93103.

DATA Data Translation A/D-D/A board, model DT-2811-PGH.

DUBS92 M. A. Dubson and Q. Zhu, Rev. Sci. Instrum. **63,** 4461 (1992).

EDWA Edwards High Vacuum, Manor Royal, Crawley, West Sussex RH10 2LW, England.

GRAB GRABSCRN and RAW2GIF are shareware programs.

HANS58 M. Hansen and K. Anderko, *Constitution of Binary Alloys*, (McGraw-Hill, New York, 1958), p. 1117.

HEWL Hewlett-Packard Company, 11311 Chinden Boulevard, Boise, ID, 83714, (208) 323-6000.

ISI International Scientific Instruments, Inc., now Topcon Technologies, 6940 Koll Center Parkway, Pleasanton, CA 94566, (510) 462-2212.

LAKE Temperature controller Model DRC 91C from Lake Shore Cryotronics, Inc., 4 E. Walnut Street, Westerville, OH 43081, (614) 891-2243.

MATH Evaporation boats obtained from R. D. Mathis, 2840 Gundry Ave., Long Beach, CA 90806, (310) 426-7049.

MICRO MICRO is a cleaning solution available from International Products Corporation, P. O. Box 70, Burlington, NJ 08016, (609) 386-8770. A typical mixture is 5% MICRO in de ionized water, heated to about 90 °C.

OHRI92 M. Ohring, *The Materials Science of Thin Films*, (Academic Press, San Diego, 1992).

OMEG Pt thin film resistance thermometer from OMEGA Engineering, Inc., P. O. Box 4047, Stamford, CT 06907-0047, (800) 826-6342.

PRES86 W. H. Press, B. P. Flannery, S. A. Teukolsky, and W. T. Vetterling, *Numerical Recipes: The Art of Scientific Computing*, (Cambridge University Press, Cambridge, 1986).

PUBP Publisher's Paintbrush by ZSoft Corporation, 450 Franklin Road, Suite 100, Marietta, GA 30067 (404) 428-0008.

SLOA Model DEKTAK IIA from Sloan Technology Corporation, P.O. Box 4608, 602 East Montecito St., Santa Barbara, CA 93103, (805) 963-4431.

ZITI Si wafers obtained from Ziti Incorporated, 970-A University Ave., Los Gatos, CA 95030, (408) 395-2115). This company is now known as Silicon Quest International, 2904 Scott Boulevard, Santa Clara, CA 95054, (408) 496-1000.

CHAPTER 3

THE ISLAND - TO - PERCOLATION TRANSITION DURING GROWTH OF METAL FILMS
Experimental observations of Pb on SiO_2 film growth

3.1 INTRODUCTION

Thin film growth is, in most cases, a poorly understood process. One such important case is that of metal films deposited by physical vapor deposition on insulating substrates. It is this situation which forms the majority of this chapter's contents. In this chapter I will summarize my experiments concerning the growth of metal films on insulating substrates as well as some of the many computer simulations which motivated this research.

The results presented here are for Pb films thermally evaporated onto clean SiO_2 substrates at different substrate temperatures and deposition rates. The two major effects studied are: 1) the very high area coverage which these metal films exhibit at the percolation threshold, and 2) the crossover from full coalescence of smaller crystalline islands to partial coalescence of larger islands. These two features and the general sequence of events during film growth are discussed in Section 3.2.

Qualitative descriptions of both these features are presented and compared to experimental results. These two effects are not independent, however. It is shown, for instance, that the large area coverage is a direct result of the existence of the crossover in coalescence behavior. This is supported by computer simulations of an Interrupted Coalescence Model (ICM) described in Section 3.3. Section 3.4 contains information regarding the film morphologies, percolation coverages, and full to partial coalescence crossover sizes. A Kinetic Freezing Model (KFM) is presented in Section 3.5 and its

predictions are compared in Section 3.6 to my experimental results. The KFM views the crossover as being due to a competition between droplet growth (due to adsorption from the vapor) and the coalescence of two touching droplets. The differences between the KFM's predictions and the experimental results, as well as some weaknesses of the KFM, are discussed in Section 3.7 in the context of what features are missing from the KFM. Section 3.8 is a brief summary of our findings.

3.2 FILM GROWTH SEQUENCE AND FEATURES

Metals deposited on insulating substrates do not immediately form a continuous monolayer film. Instead, the film often grows in what is known as the Volmer-Weber growth mode [LEWI78, PASH64, 65]. This growth mode is characterized by the formation of isolated three-dimensional structures (here termed "islands") which eventually touch as illustrated in Figure 3.1.

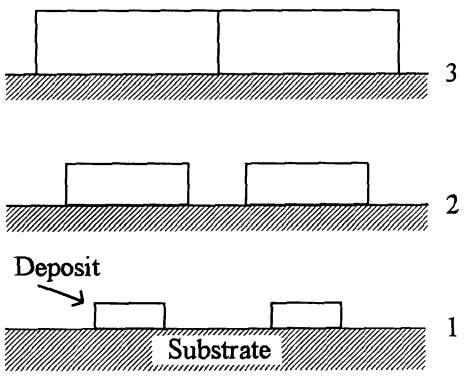

Figure 3.1 Schematic illustration of three-dimensional Volmer-Weber island growth.

This growth process, as all others, proceeds from an early stage of nucleation. Here, small, stable clusters of material are formed which act as preferential growth sites on the substrate. As the average film thickness increases, these structures accumulate atoms

and increase in height and width. The island size and density increase until they begin touching nearby islands. When these islands come into contact they undergo either full or partial coalescence, resulting in an increase in the average island size and a decrease in the total number of islands.

Full coalescence is the process whereby two compact islands touch and grow together to form a larger, but still compact, island. An example of this process is the touching of two water droplets. While the material volume is conserved, the surface area changes in order to minimize the total surface energy. For the case of liquid droplets, where the surface energy is isotropic, on a substrate, the shape which minimizes the surface energy is the cap of a sphere with the angle of contact between the droplet and the substrate given by Young's equation [OHRI92]. Non-liquid islands behave similarly except that in a crystal system the surface energy is anisotropic and the equilibrium shaped islands contain facets.

Under the experimental conditions studied here, coalescence of solid metal islands is predominantly due to surface diffusion which is driven by gradients in the surface curvature (or, equivalently the chemical potential) [PASH66] of the material. Other methods of mass flow exist such as volume diffusion, evaporation-condensation, and viscous flow. Volume diffusion and evaporation-condensation are negligible until close to the melting point. Calculations [HERR51] indicate, that for particle sizes larger than roughly 50 nm, the surface stress is much smaller than the yield stress needed to cause viscous flow of dislocations. For the case of two touching islands, the curvature gradient is strongest at the connection point of the two islands so that material is drawn into this "neck region." Intuitively, this can be understood in terms of where a wandering atom would feel the most binding. This location is at the bottom of a groove.

One important feature of the full coalescence process is *wiping*. Wiping refers to the fact that a portion of the substrate is wiped clean during the coalescence event. Regions of the substrate which were originally covered by one of the two droplets are left

bare following coalescence. If deposition is taking place, then this clean substrate now provides a location in which new islands may nucleate. Thus, this cycle of growth and coalescence is a recurring event. Wiping always creates empty regions with a size comparable to the radius of the initial islands involved in the coalescence event.

The coalescence and wiping process is shown in Figure 3.2. Two droplets which touch quickly grow together, by formation of a neck, to form a cigar shaped island. This partial coalescence stage then slowly proceeds on to full coalescence as shown at the right in Figure 3.2. The shaded regions in the full coalescence portion of Figure 3.2 indicate the regions of the substrate which were initially covered by the two touching droplets.

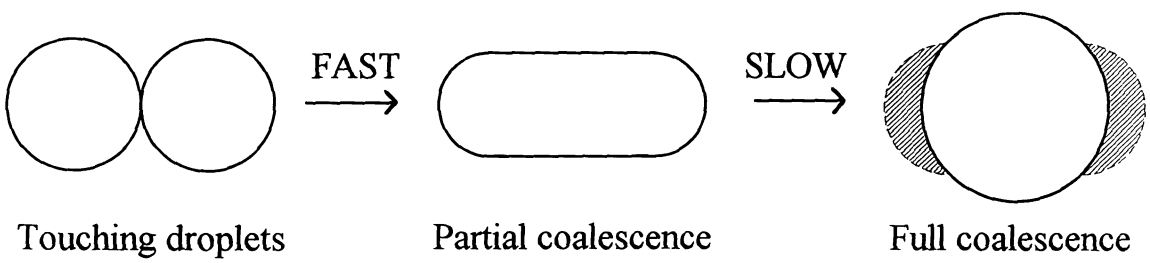

Figure 3.2 Coalescence and wiping process.

This full coalescence process does not continue until the film is hole-free. Instead, at some point during growth the islands fail to fully coalesce once they are touching. In this case, typically only the partial coalescence stage shown in Figure 3.2 is completed.

An effect of this crossover from full to partial coalescence is illustrated by the two images in Figure 3.3. These two images are of the same sample which is roughly 50 nm of Pb on oxidized Si (100) at room temperature. However, as mentioned in Chapter 2 all of our samples have a thickness gradient so that the right side of Figure 3.3 (a) is thinner than the left side. By how much the average thickness differs in these two regions is unknown. The point of this image is to illustrate, qualitatively, the stages of film growth from compact islands to a percolating structure. The right side of Figure 3.3 (a) shows a large

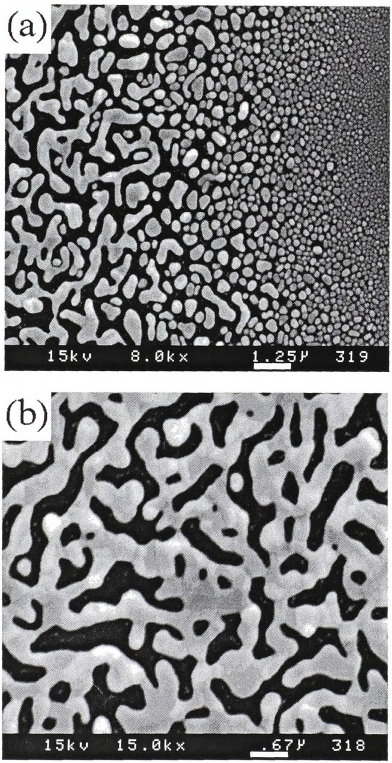

Figure 3.3 Growth evolution of Pb on insulating SiO_2 substrates. (a) Compact islands to elongated structures (from thin (right) to thicker (left) deposits). (b) Percolation threshold which occurs at a higher film thickness than in (a), with $p_c \approx 63\%$.

number of small islands with nearly uniform sizes and shapes. Actually, there exist many smaller islands between these which are unresolved in the micrograph. This stage of growth is known as the "Breath Figure" state in analogy to the patterns resulting from the condensation of warm water vapor on a cold surface [BEYS86, 91]. This structure is produced by many generations of complete coalescence and wiping. As the thickness increases (to the left in Figure 3.3 (a)) full coalescence of islands ceases. This results in the elongated "wormy" structure becoming apparent in the left side of the image. With their larger size, these islands quickly join together with their neighbors and cause the film to percolate as shown in Figure 3.3 (b) which was taken further to the left of the region in Figure 3.3 (a).

Two important features are present in Figure 3.3. The first is the area coverage of $p_c \approx 63\%$, at the percolation threshold for the image in Figure 3.3 (b). This value of p_c is in the range of that predicted by various random percolation models and, as such, is not particularly high. Samples will be discussed which have a much larger value of p_c as they were prepared under different conditions. As this is what we first noticed and interested us in film growth it will be discussed first in this chapter. The second feature is the crossover from full to partial coalescence of the islands. This transition is interesting since it determines the characteristic length scale of the percolating film. Knowledge of the factors controlling this crossover would be useful in advancing our understanding of film growth. The crossover will be discussed in the latter portions of this chapter. Neither of these issues in film growth has been adequately addressed.

Many authors have studied the geometrical and transport exponents of real metal films and compared them to the predictions of percolation models [STAU85]. These exponents include those governing the correlation length, the fractal dimension, and the electrical conductivity. Measurement of these exponents by film morphology analysis yields values which are in agreement with those found in two-dimensional pure percolation models [KAPI82, LAIB82, VOSS82]. While these experimental results show agreement

with computer simulations, in terms of quantitative exponents, they fail, on the other hand, to exhibit certain characteristics of real films. In particular, they do not exhibit important features such as wiping, full coalescence, and a high value of p_c.

Extensive computer simulations have been performed in our laboratory over the last number of years in efforts to develop simulations which accurately mimic the growth of real metal films. The majority of this work was aimed at determining the scaling exponents of various models of growth [WOLL93]. Simulations incorporating attractive nearest-neighbor interactions with different deposition and post-deposition annealing scenarios were studied. One of the main results of these studies is that the percolation coverage never exceeded roughly 60% for a wide class of simulations. This is surprising since pure percolation models also have p_c in the 60 to 70% range. As stated earlier, the geometric and transport exponents agreed very well with simple two-dimensional pure percolation models with no interactions.

A simple model was developed which shows that the high values of p_c are a direct result of the crossover from full to partial coalescence [YU91]. This model is described in the following section.

3.3 INTERRUPTED COALESCENCE MODEL

In this section we argue that the high value of p_c observed in real films (higher than that predicted by random percolation models) arises naturally from the existence of the full to partial coalescence crossover. A general model of film growth involving only immediate, full coalescence was developed by Family and Meakin [FAMI88a, 88b, 89]. I will refer to this as the Family and Meakin Model (FMM). Hemispherical droplets of radius R_0 are deposited at random on a two-dimensional substrate. If two droplets, of radii R_1 and R_2 touch they instantaneously coalesce with conservation of volume and center of mass according to the rule,

$$R^3 = R_1^3 + R_2^3 \tag{3.1}$$

which results in a single droplet of radius R. This model predicts a bimodal droplet size distribution which agrees with that observed by Carr *et al* [CARR] for the size distribution of Sn droplets thermally deposited onto a heated sapphire substrate. This model is applicable to the early stages of film growth when the "Breath Figure" structure is still present as shown in Figure 3.4. However, there is a serious feature absent from this model. The FMM has no percolation transition. Since coalescence is always present, percolation will only occur when one large droplet spans the entire sample surface.

It is for this reason that Duxbury and Yu developed the Interrupted Coalescence Model (ICM) [YU91] as an extension of the FMM. As the name implies there is an interruption in the coalescence behavior of two droplets. In this model individual droplets of radius R_0 are still deposited at random on a substrate. Imagine two touching droplets of radii R_1 and R_2. If R_1 and/or $R_2 < R_c$ (R_c is a parameter to be described shortly) then coalescence takes place according to the rule expressed in equation (3.1). However, should R_1 and R_2 be larger than R_c then there is no coalescence. Thus, R_c corresponds to the critical droplet radius for the transition from full to partial coalescence. The pure percolation case corresponds to $R_c/R_0 < 1$. Indeed, for $R_c/R_0 < 1$ the ICM predicts that $p_c = 0.676 \pm 0.002$ which is in agreement with the predicted result [GAWL81]. The radii R_1, R_2, R_c, and the system size L may be expressed in terms of the unit length R_0.

A sample morphology produced by the ICM for the case $R_c/R_0 = 8$ is shown in Figure 3.5. The major difference between Figure 3.5 and the image in Figure 3.3 (a) occurs in the neck region where two droplets touch. In real films these indentations fill in very quickly as they are regions of high binding energy and curvature gradient. Also, real films and the ICM exhibit wiped regions near the perimeters of the larger droplets. The simulation in Figure 3.5 is at the percolation threshold and has a p_c of roughly 82%. Only droplets of size $R > R_c$ lie along the percolation path (the infinite cluster).

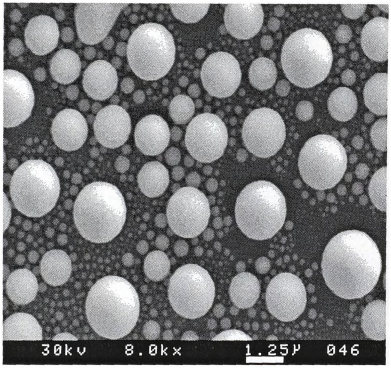

Figure 3.4 "Breath Figure" stage which occurs in the early stages of metal film growth. This image is of a Pb film on a 483 K SiO_2 substrate.

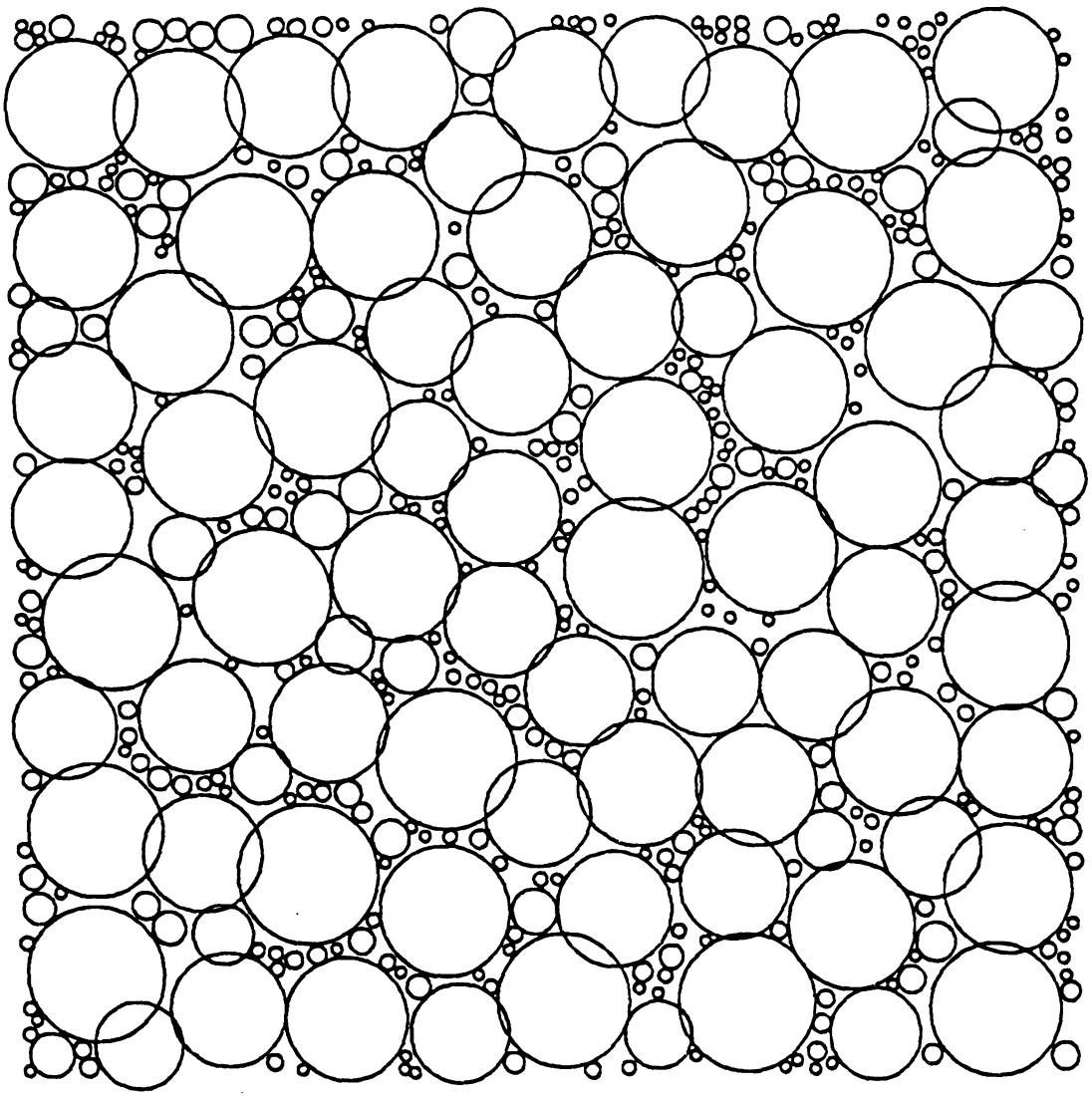

Figure 3.5 Percolation pattern resulting for 3D droplets on a 2D substrate using the ICM with $L/R_0 = 200$ and $R_c/R_0 = 8$. The coverage is 82%.

Since only the large droplets lie along the percolation path we can understand the relatively high value of p_c obtained using this model. In the "Breath Figure" morphology, the large droplets appear to act as repelling islands -- they tend to be as far apart as possible. This apparent repulsion is not due to any direct energetic interactions. It is caused by many generations of coalescence and wiping which leave gaps, between droplets, which are comparable in size to the droplet radius. As an example of the high values of p_c, consider a square lattice with identical disks at each vertex. If we now simultaneously increase the radius of all these disks by the same amount, eventually each disk will come into contact with its neighbors. At this point the coverage will be $p_c = \pi/4 \approx 79\%$. If we use a triangular lattice, the most densely packed structure, instead, the disks will touch when $p_c \approx 91\%$. Since these simulations are performed on a continuum substrate and have droplets of varying sizes, a quantitative prediction of p_c is not possible. However, the large droplets still behave as a system of repelling objects causing p_c to increase.

For the case of three-dimensional droplets on a two-dimensional substrate the ICM predicts that p_c saturates at roughly 80% for $L/R_0 = 66$ and $R_c/R_0 \gtrsim 3$ when averaged over 100 trials. This length scale is much different than that of real films. Real films exhibit the crossover from full to partial coalescence at sizes $\sim 300R_0$ with R_0 an atomic radius. Were R_c equal to roughly $300R_0$ the simulations would require an intolerable amount of time to complete. The pattern shown in Figure 3.5 required a few hours of CPU time on a Convex mainframe computer. Thus, although quantitatively inaccurate, the ICM provides a simple intuitive explanation of the experimentally observed high p_c based on the observed existence of a crossover from full to partial coalescence in actual films.

3.4 FILM MORPHOLOGY AND PERCOLATION

As mentioned in Section 3.2 real films exhibit larger values of p_c than predicted by various computer simulations. An example of this is shown in Figure 3.6 which shows a 500 nm thick Pb film, deposited at a rate of 6 nm/s, onto a 453 K amorphous SiO_2 substrate. This sample was "quench cooled" within a few seconds after completion of the deposition. This particular sample has $p_c = 83.9 \pm 0.3\%$. This film consists of metal "wormy" structures which are of nearly uniform height separated by long, narrow, intertwining channels. These channels are populated by many small islands which are not resolved in this micrograph. Additionally, the islands appear to repelling their neighbors on all sides. It is the long channels and the apparent "repulsion" which result in the values of p_c being so high. Similar growth behavior and film structure has been observed for Ag films on Mica [BASK94] where networked island morphologies with coverages of roughly 66% to 89% were found.

The same general appearance shown in Figure 3.6 occurs near percolation for substrate temperatures from room temperature up to about $T_0 = 460\ K = 0.77T_{melting}$. The major difference between samples prepared in this temperature range is the length scale. Lower temperature samples require a smaller thickness to reach percolation and the width of the metal islands at the percolation point is also less than for higher substrate temperatures. Figure 3.7 shows a plot of p_c versus substrate temperature for samples deposited at 6 ± 0.3 nm/s. It is clear from this figure that there is no overall trend to p_c with temperature. Individual points have uncertainties which are roughly the same size as the symbols and were averaged over two to five images taken of each sample near the percolation threshold. The anomalously large values of p_c observed for samples prepared with $T_{substrate} \gtrsim 460$ K is, as we shall see, a result of a significant difference in the sample morphology.

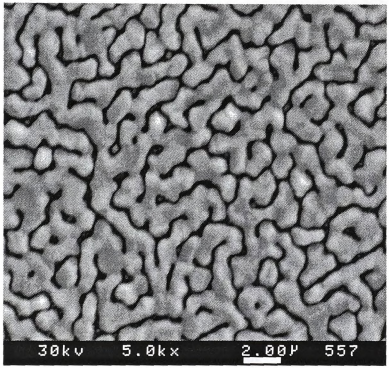

Figure 3.6 Percolation pattern of a 500 nm thick Pb film deposited at 6 nm/s onto a 453 K SiO_2 substrate. This film was quenched immediately following deposition. The coverage is ≈84% and the average metal island width is 1 μm.

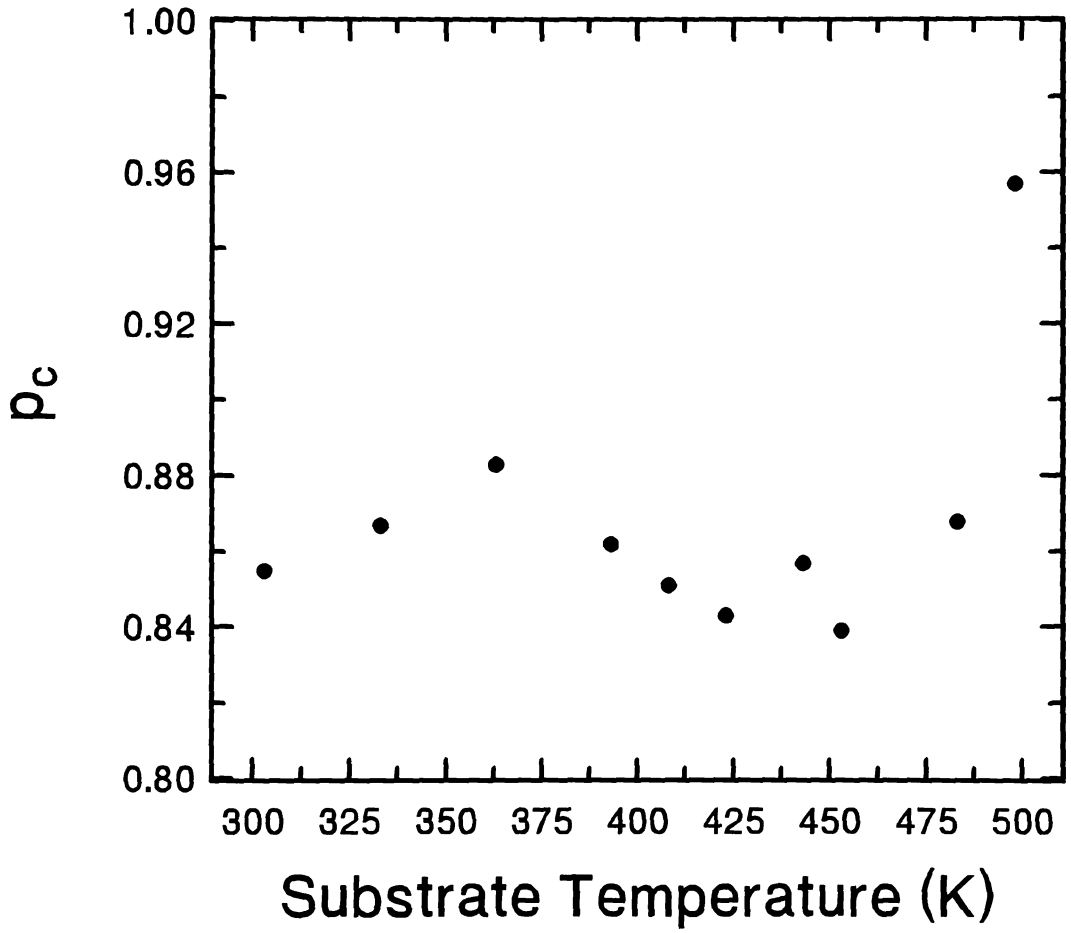

Figure 3.7 Area coverage at percolation, p_c, as a function of substrate temperature for Pb films deposited at 6 nm/s.

An example of the difference in morphology above and below T_0 is seen by comparing Figure 3.6 to Figure 3.8. Figure 3.8 is a 1600 nm thick Pb film evaporated at a rate of 6 nm/s onto a substrate held at 463 K. This image contains regions which appear similar to both the early "Breath Figure" stage as well as other portions which more resemble the percolation structure shown in Figure 3.6. It is important to notice the scale difference between Figures 3.6 and 3.8. This complicated morphology complicates determination of the percolation point. For this reason, values of p_c and R_c for samples with $T > T_0$ are very uncertain.

There have been numerous studies on the equilibrium crystal shape (ECS) of Pb crystallites [HEYR83, 87, 89, METO82a, 82b, 89a, 89b] as well as of Au and In crystals. There is a difference in the resultant crystal shape depending on the starting shape of the crystallites. Pb condensed on a room temperature substrate and then annealed results in ECS's which are cubo-octahedra with a contact angle between the substrate and the crystallite of roughly 110°. On the other hand, Pb condensed onto graphite substrates at 473 K form flat. triangularly shaped, tabular crystallites which require hundreds of hours of annealing before showing substantial morphological change. This symmetric shape results from the Pb crystallites being epitaxially oriented with their {111} faces parallel to the {00·1} planes of the substrate.

For substrate temperatures below T_0 my films show a flat, tabular island shape with an average height-to-radius ratio near 1.0 and a contact angle $\theta_c \approx 135°$ to be present during the early stages of film growth and through the percolation crossover. However, for $T > T_0$ droplets form spherical caps with a height-to-radius average of 1.7 and $\theta_c \approx 145°$ which are present until near the percolation threshold. These structures resemble the "Breath Figure" shown in Figure 3.4. Near percolation, the film structure contains regions of "near-equilibrium shaped" islands as well as areas of connected metal islands.

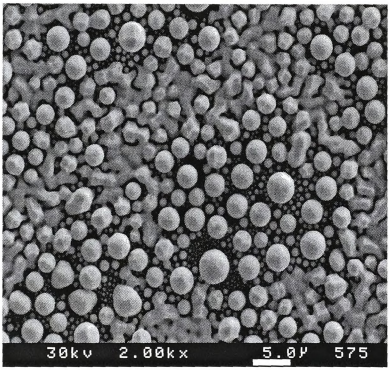

Figure 3.8 Film morphology of a 1600 nm Pb film prepared at T = 463 K > T_0. The structure is discussed in the text.

Examples of this dual morphology are shown in Figures 3.8 and 3.9. Figure 3.9 shows a 3470 nm Pb film deposited at 6 nm/s on a 498 K SiO_2 substrate. The large faceted droplets appear quite similar to the cubo-octahedral ECS of Pb. These large crystals are not all of uniform orientation since the substrate is amorphous. However, x-ray scattering measurements of a few of my samples indicates that the (111) face is generally parallel to the substrate. This is expected with the growth of face centered cubic materials, such as Pb, since the (111) face has the lowest surface energy.

An interesting aspect of Figure 3.9 is that most of the larger crystals are extremely faceted. Although some of these crystallites resemble the ECS it is not possible, without more orientation information, to claim whether or not these are ECS crystals. We don't believe these are ECS crystals. The cause of the faceting is because these crystals have not coalesced recently. Thus, they have had time to begin approaching the ECS but not enough time to reach the ECS. Other droplets of similar size appear to be spherical as they have recently coalesced with a nearby droplet, as evidenced by the denuded zone near their perimeters. This combined with continuing deposition results in the very faceted crystals shown in Figure 3.9. It has been shown that crystals approach their ECS more quickly if incident vapor is still present due to the constant flux of material. This trend has been observed in my samples since the tops (exposed to the incident vapor) of crystallites appear more faceted than do the lower portions (which are effectively shielded from the vapor). Metois and Heyraud [METO82a] found that on the order of four hours is needed to anneal roughly 5 μm Pb crystallites to their cubo-octahedral ECS. The deposition time for the sample in Figure 3.9 was 9.7 minutes. Thus, we should not, perhaps, even expect the crystallites to resemble the ECS. Also, if these crystals are approaching the ECS, smaller crystallites should more closely resemble the ECS which they do not. Additionally, contamination is known to strongly influence surface diffusion [METO82b]. The studies of Heyraud and Metois were performed under UHV conditions. In particular, the presence of O_2 was found to significantly increase the surface diffusion of Pb. On the

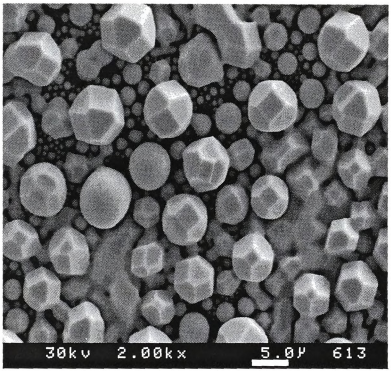

Figure 3.9 A film prepared with T = 498 K which is well above T_0. The film is 3470 nm thick with a deposition rate of 6 nm/s.

other hand, my samples are prepared in a vacuum of roughly 10^{-7} to $5x10^{-6}$ mbar. The samples of the above authors were also prepared in a different method: deposition at room temperature followed by an annealing process (instead of observing as-grown films) onto a very different substrate. Thus, the faceted crystallites in Figure 3.9 are not ECS crystals, but are a result of the growth conditions.

As mentioned in Chapter 2 the sample cooling rate following deposition was found to strongly influence the resultant film morphology. This effect is illustrated by the four images shown in Figure 3.10. This sequence of images shows samples which are identical in thickness, deposition rate, and substrate temperature, but with various annealing times, t_{anneal}. Each sample is 400 nm of Pb evaporated onto a 423 K substrate. Immediately following deposition, but prior to quench cooling at roughly 20 K/minute, each sample was allowed to sit for a) 0, b) 1.2, c) 2.3, and d) 4.5 minutes at the deposition temperature. The deposition time, t_c, of each of these samples was roughly 1.1 minutes so that these annealing times correspond to 0, 1, 2, and 4 times the deposition time. The four images shown are of four different samples prepared successively in one pumpdown cycle. Each of these images was taken at the center of the sample spot. Similar behavior is seen at the percolation thresholds of each sample. The height of the islands in the later images are probably thicker than those in the earlier images if we imagine each image evolving from the structure of the previous sample. This is because to decrease their lateral extent, as is evident in Figure 3.10, the islands must grow in the vertical direction. Were this annealing allowed to continue the islands would eventually break up into isolated droplets which would then approach the final ECS.

From Figure 3.10 it is clear that p_c is strongly effected by annealing. The image in Figure 3.10 (d) is reminiscent of the morphology observed in early samples which were cooled slowly. During annealing, surface diffusion and coalescence events continue to occur. Thus, slow cooling and annealing produce similar results.

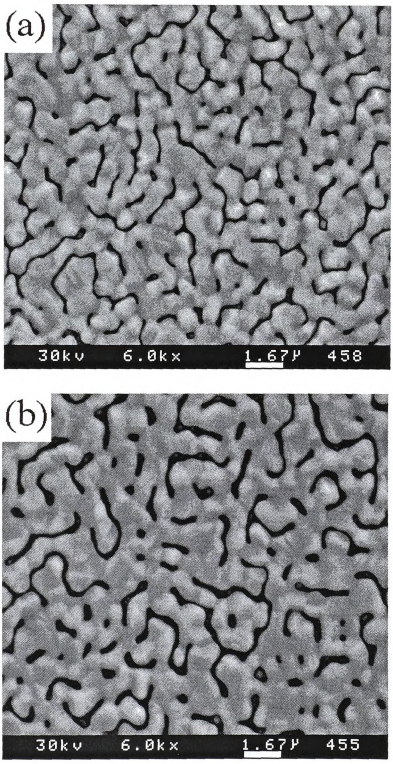

Figure 3.10 Sequence of images illustrating the effects of annealing on the film's final morphology and percolation coverage. Each film is 400 nm of Pb deposited at 6 nm/s onto a 423 K substrate. Annealing times are (a) 0 and (b) 1.2 minutes.

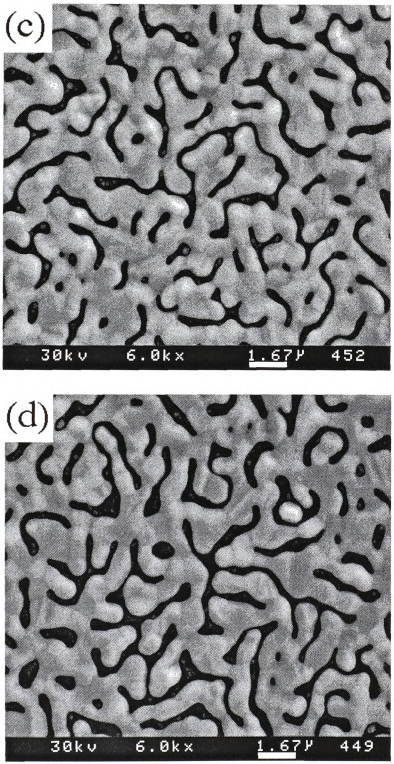

Figure 3.10 (cont.) Images with annealing times of (c) 2.3 and (d) 4.5 minutes. The deposition time for each sample was 1.1 minutes.

The percolation coverages of the four samples in Figure 3.10 (but taken at the percolation threshold), and others, at a substrate temperature of 423 K, are shown in Figure 3.11 as a plot of p_c vs. the ratio t_{anneal}/t_c where t_{anneal} is the annealing time following deposition and t_c is the deposition time to reach the percolation threshold. The three different symbols in Figure 3.11 correspond to samples prepared at different deposition rates. In addition, each of these different deposition rates requires a different thickness to reach percolation. This will be discussed further in a later section of this chapter. Higher deposition rate samples require a lower thickness to reach percolation. Thus, although the incident vapor flux is larger, the total amount of deposit is lower. However, p_c turns out to be fairly independent of deposition rate. Since samples receive no incident vapor flux during annealing it is not surprising that samples with different deposition rates show a common behavior in how p_c drops as t_{anneal}/t_c increases.

The percolation threshold is a result of the existence of the crossover from full to partial coalescence of touching islands. The important length scale at which this crossover occurs is denoted by R_c. Islands having a radius smaller than R_c will undergo full coalescence whereas islands larger than R_c only complete the partial coalescence stage. Thus, this size should be given strictly by the radius of the largest droplets in "Breath Figure" images such as that shown in Figure 3.4. We decided, however, to determine R_c using the film morphology at the percolation threshold since using "Breath Figure" images could be ambiguous. The reasons for this decision were many. First, the half width of the connected structures of deposit material at percolation is not significantly different from the radius of the largest droplets in the "Breath Figure" stage. Secondly, since we were already interested in the percolation threshold, the analysis program used to find p_c was easily modified to include determination of R_c as discussed in Section 2.7. Finally, the method used is simple and yields consistent results.

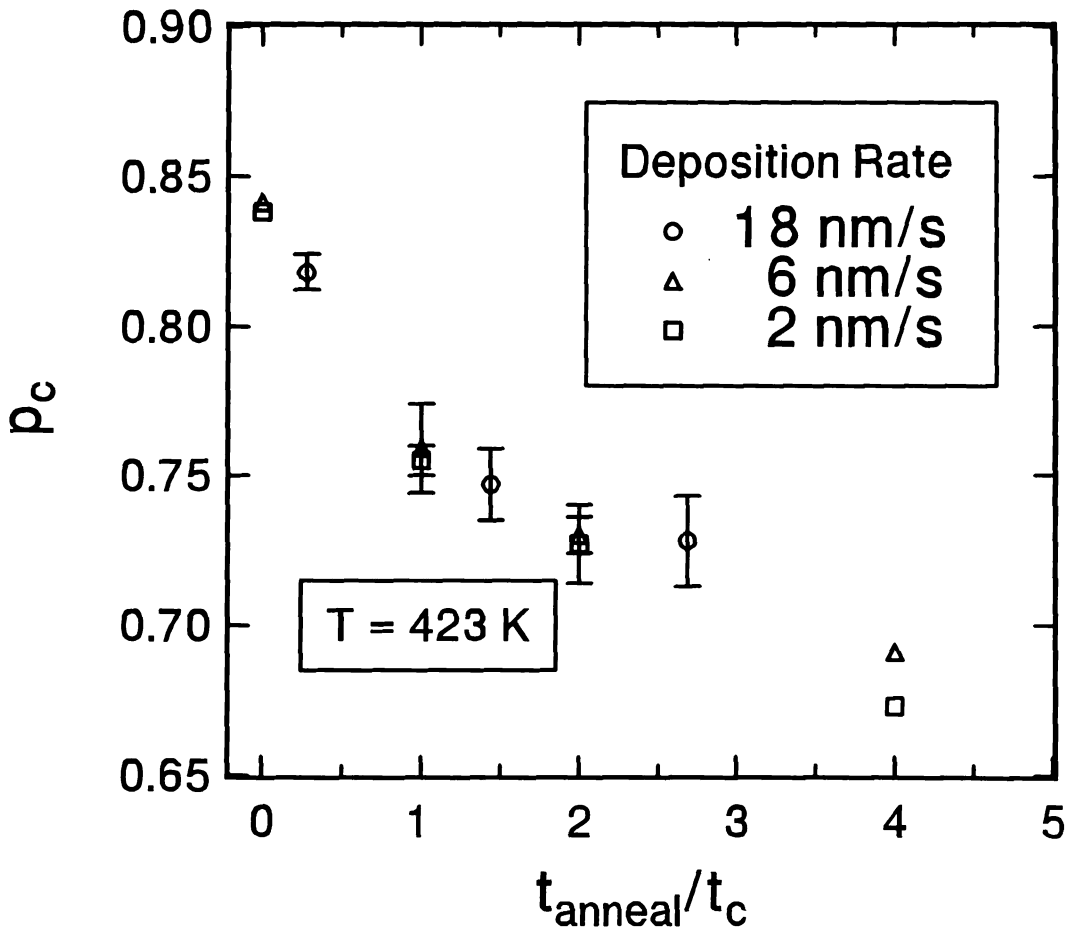

Figure 3.11 Percolation coverage vs. ratio of anneal time to deposition time for Pb samples with different deposition rates. All samples were prepared on 423 K substrates.

From the same images used to produce the p_c vs. substrate temperature data, shown in Figure 3.7, the resultant metal structure ("worms") half widths vs. substrate temperature data is displayed in Figure 3.12. The uncertainties in R_c, determined from multiple images of each sample, for $T < 460$ K are much smaller than the data symbols. In fact, the uncertainties are generally ~ 0.01 μm. However, the uncertainties in R_c for the higher temperature samples is a result of the already mentioned morphology change near 460 K. As illustrated in Figure 3.9, the simultaneous presence of percolating regions and "Breath Figure" areas obstructs the percolation point and causes our algorithm to be inappropriate in such situations.

At a constant deposition rate the crossover radius R_c increases with rising substrate temperature. This behavior is in agreement with the Kinetic Freezing Model (KFM) to be presented in the following section. In the KFM, the full to partial coalescence crossover is a result of the competition between film growth and droplet coalescence. Surface diffusion is an activated process which increases at higher temperatures. A constant deposition rate holds the droplet growth rate steady, allowing surface diffusion to become more influential in coalescence. That is, increased surface diffusion allows droplet coalescence to occur with less opposition from vapor deposition. As will be discussed in Sections 3.6 and 3.7, the KFM is incomplete. Other influences are present during film growth which effect the coalescence process and crossover. Aside from the competition between coalescence and deposition these other effects can act to pin, or inhibit, the coalescence process.

The dramatic change in the measured values of R_c above T_0 is definitely a result of the morphology transformation at this temperature. However, we do not fully understand the cause of this morphology change. Were this change due to an increased solubility of Pb in the SiO_2 then the Pb would tend to spread out more on the substrate rather than "balling up" as is observed. Simple calculations indicate that Pb is not easily soluble inside the amorphous SiO_2 network. SiO_2 is also extremely stable ($T_{melting} \gtrsim 1300$ K) over the

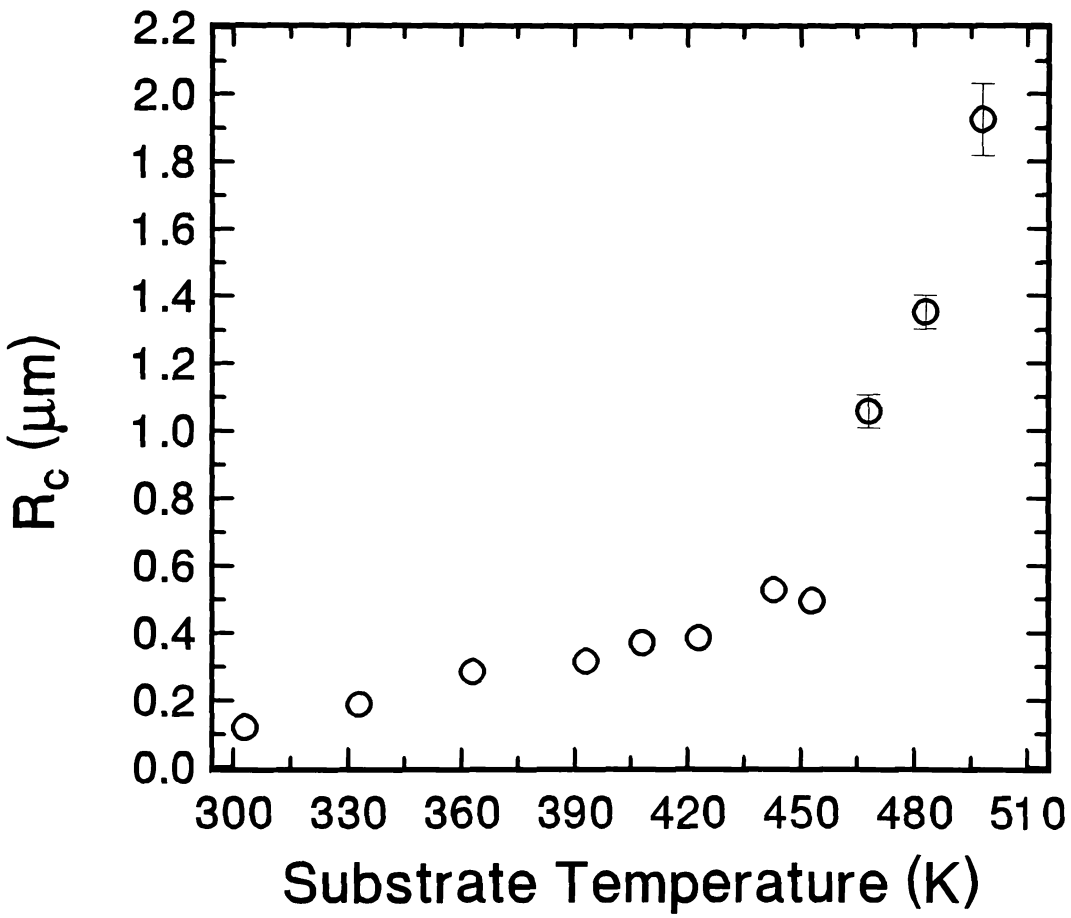

Figure 3.12 Crossover radius R_c vs. substrate temperature for Pb samples evaporated at 6 nm/s onto SiO_2 substrates.

range of temperatures studied. Another possible cause of this morphology change is due to substrate contamination. Prior to sample deposition, the substrate is heated to 675 K. However, the deposition temperatures are lower than this so that residual contamination, such as pump oils, may be readsorbed on the substrate. The temperature T_0 may correspond to a temperature where some of this contamination is desorbed from the substrate. This would leave the substrate surface cleaner, thus reducing pinning of the coalescence process. Unfortunately, with no quantitative contamination information available on our vacuum system, this is only speculation. This was one reason for pursuing the UHV deposition system which will be discussed in Chapter 4.

3.5 KINETIC FREEZING MODEL

I will now discuss our model [JEFF94] to explain the full to partial coalescence crossover. This model is based on the fact that during film growth there are two main competing processes occurring. These two processes are coalescence and deposition. Coalescence tends to decrease the system connectivity (recall the argument about the large droplets acting as though they repel each other). On the other hand, deposition of further material acts to increase the lateral extent (termed "spreading") of the droplets already present on the substrate. Both of these actions have a characteristic time scale which depends on the droplet size. The process having the shorter completion time will be dominant. The crossover from full to partial coalescence occurs when the coalescence time changes from being smaller than the deposition time scale to being larger. At this transition, when two islands are touching they will grow to touch neighboring islands before they have fully coalesced. This results in a connected, percolating system. The deposition of material is effectively freezing the coalescence kinetics, thus creating a non-equilibrium morphology.

For two touching droplets to coalesce via surface diffusion requires a time τ_{coal}. A complete analytical theory covering the entire coalescence process is lacking at present, but enough is known for our purposes. The dynamics of the early "neck-filling" stage have been studied [KING55] as well as the regime near the final stages of coalescence. This work begins with some of the ideas to be presented in Chapter 5, most importantly that a surface curvature gradient is the driving force for surface diffusion. The result most germane to my purposes here is that due to Nichols and Mullins [NICH65, 66]. These authors numerically solved the relevant partial differential equations, as first derived by Mullins [MULL57, 59], governing the entire coalescence process. Their results during the initial "neck-filling" stage are that the time required to reach the intermediate "neck-filling" stage $x/R_0 = 0.3$ is very rapid, $\sim 10^{-5}(R_0)^4/B$ where $B = D_s\gamma_0 N_0 \Omega^2/k_B T$, x is the radius of the metal bridge between the two droplets and R_0 is the initial droplet radius. In performing these studies the surface diffusion constant D_s and the surface energy γ_0 were both assumed to be isotropic. The number of surface sites per unit area N_0 is related to the atomic volume Ω through $N_0 = \Omega^{-2/3}$. To reach the stage labeled "partial coalescence" in Figure 3.2 requires a time of $0.166(R_0)^4/B$ while a time of $0.890(R_0)^4/B$ is needed to complete full coalescence.

We can estimate order of magnitude values for these times by taking Au as an example. For Au, $\gamma_0 = 1450$ erg/cm^2, $\Omega \approx 10^{-23}$ cm^3, and $D_s \sim 10^{-7}$ cm^2/s when $T \approx 675$ K. For Au droplets of radius 100 nm, neck elimination and complete coalescence each require much less than one second to complete. Smaller metal islands will have correspondingly shorter coalescence times. This has been verified experimentally. Full coalescence of droplets has been observed using *in situ* electron microscopy during film growth. Coalescence events do, indeed, occur on the scale of fractions of a second for the smaller islands.

From the times given above for the various stages of coalescence it is obvious that the final approach to equilibrium during the late stages of coalescence is very slow. The

majority of the material movement occurs until shortly after the neck is eliminated (the partial coalescence stage in Figure 3.2). Thus, we take a reasonable value of 0.4 as the prefactor. That is, we define the effective coalescence time to be

$$\tau_{coal} = 0.4 \frac{k_B T}{D_s \gamma_0 \Omega^{4/3}} R^4. \tag{3.2}$$

We now consider the second major influence on the droplets in the film, namely growth due to adsorption from the vapor. We view this from the "Breath Figure" stage shown in Figure 3.4. That is, since it is the large droplets which dominate the percolating infinite cluster we consider their growth. In particular, the growth time of interest is that required for these large droplets to increase in size enough to touch neighboring droplets of similar size. Since these larger droplets generally exhibit a denuded zone near their perimeters due to the wiping which occurred during their last coalescence event, accretion of smaller islands at their perimeters is small. In addition, to take this effect properly into account would require one to make further assumptions about the nucleation rate and island size distribution in these wiped regions.

Up to the percolation threshold we have observed the films prepared below T_0 to maintain a constant height-to-radius ratio $\alpha \approx 1$. After many generations of coalescence, a "Breath Figure" stage is reached where the large droplets have a coverage $p \approx 0.57$ [DUXB]. The average thickness of deposited material after a time t at deposition flux J (#/cm^2·sec) of atoms having atomic volume Ω is $J\Omega t = h_{avg}$. However, since the film forms three dimensional islands the average thickness is less than the maximum droplet height. A film, consisting of islands of radius R, with coverage p has an average height of roughly $p\alpha R$.

Since it is the percolation threshold which attracts our interest we concentrate on the case when $R = R_c$. Further, we envision the situation where two droplets of radius R_c have just come into contact. The time we seek is that needed for one of these two droplets to increase its radius to the point where it contacts more neighbors. When this

happens a connected network of metal "worms" will form. The time to reach the stage where the islands have an average radius R is given by

$$t = \frac{\alpha p}{J\Omega} R \tag{3.3}$$

where p is the substrate coverage fraction and takes into account the fact that the film is not of constant height. In the "Breath Figure" stage $p \approx 0.57$. Now, in order for the large islands to touch their neighbors, their projected area on the substrate must increase by roughly 1/p which corresponds to a radius increase to $R' = Rp^{-1/2}$. Thus,

$$t' = \frac{\alpha p_c}{J\Omega} R' = \frac{\alpha p_c}{J\Omega\sqrt{p}} R \tag{3.4}$$

is the time needed to grow to a size R'. The *spreading time* τ_{spr} is the difference between t' and t, under the assumption of constant deposition rate, so that

$$\tau_{spr} \approx 0.5 \frac{\alpha}{J\Omega} R. \tag{3.5}$$

At the crossover between full and partial coalescence the premise of the KFM is that $\tau_{spr} = \tau_{coal}$. Equating the expressions in equations (3.2) and (3.5) with $R = R_c$ yields.

$$R_c^3 \approx \frac{\alpha D_s \gamma_0 \Omega^{1/3}}{k_B T J}. \tag{3.6}$$

This equation may be rearranged and expressed in a manner more easily compared to the experimental measurements. During sample deposition the time required to deposit each film, t_c, is recorded and the films are prepared to slightly past the percolation threshold. All positions on each sample have the same deposition time, but, due to the thickness gradient mentioned in Chapter 2, different locations experience different deposition fluxes J. Since, from equation (3.3), $J\Omega t_c = \alpha p_c R_c$ equation (3.6) may be expressed as

$$\frac{k_B T R_c^4}{D_s \gamma_0 \Omega^{4/3}} \approx t_c. \tag{3.7}$$

Given the approximations involved in arriving at this expression it is estimated to be correct to within roughly a factor of two. This relatively large uncertainty has little impact on the comparisons to be drawn with the experimental results.

3.6 PREDICTIONS OF THE KINETIC FREEZING MODEL

Equation (3.7) carries two predictions which may be tested experimentally. These predictions are: (1) the deposition time dependence of R_c and (2) that average surface diffusion constants D_s may be inferred. These two predictions will be discussed separately in the following two subsections.

3.6.1 R_c DEPENDENCE ON DEPOSITION TIME

The most evident feature of equation (3.7) is the prediction that $R_c \sim (t_c)^{1/4}$ at constant temperature. To test this prediction, R_c was measured for samples prepared with various deposition times t_c. Films prepared with higher deposition rates percolate at lower thicknesses than do films deposited at lower rates. Some of the samples required on the order of ten seconds to deposit. This short deposition time combined with the importance of careful quenching of the sample would have made preparation of these samples much more difficult if the He "quench" method had not been used. The deposition time dependence of R_c was measured carefully at two temperatures. Both temperatures were below T_0 and yielded similar results. Figure 3.13 shows a log-log plot of our R_c vs. t_c data at T = 408 K and 423 K for different deposition rates which vary over one decade from about 2 to 20 nm/s. With $R_c \sim (t_c)^{1/\beta}$, the KFM predicts $\beta = 4$. The data of Figure 3.13 displays a weaker dependence with $\beta_{avg} \approx 7.5$. We attribute this discrepancy to two important factors missing from the KFM, namely grain boundaries and substrate roughness, as will be discussed in Section 3.7.

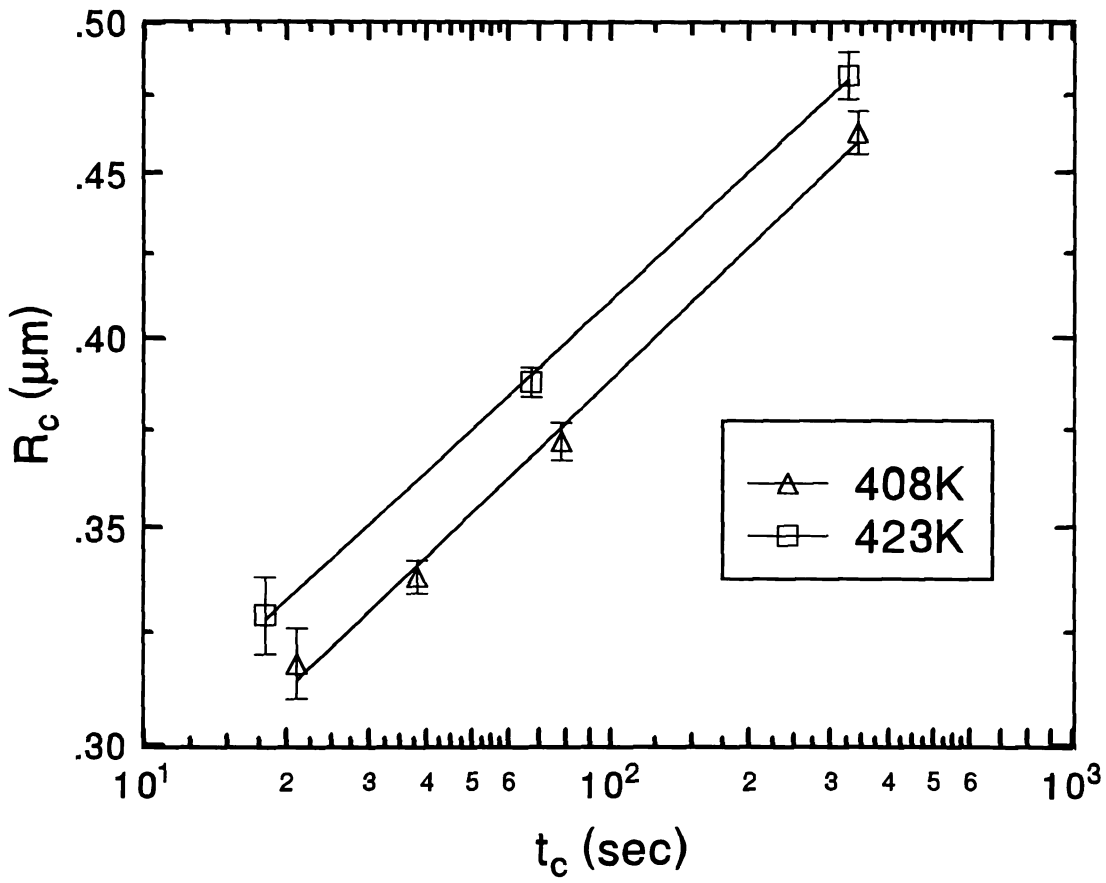

Figure 3.13 Log-log plot of the radius R_c vs. deposition time t_c needed to reach percolation for Pb films. The lines are power law fits to $R_c \sim (t_c)^{1/\beta}$ with $\beta \approx 7.4$ (408 K) and $\beta \approx 7.6$ (423 K).

3.6.2 INFERRED SURFACE DIFFUSION CONSTANTS D_s

Using equation (3.7) and the experimentally measured values of R_c, t_c, and T we may solve for the surface diffusion constant D_s. These values of D_s are averaged over all crystal faces present on the crystallites during growth. Different crystal surfaces possess different values of D_s due to the varying surface structures. For instance some faces are isotropic in two dimensions while other faces consist of "channeled" structures so that D_s on these surfaces may be anisotropic as well. If the KFM is qualitatively reasonable then our estimated values of D_s should roughly agree with other experimental measurements on specific crystal faces.

In order to calculate D_s we need values of Ω and γ_0 in equation (3.7). The atomic volume of Pb is 3.0×10^{-23} cm^3. While the surface energy of a crystal is, in general, anisotropic, in the KFM the surface energy is assumed to be isotropic with a value γ_0. We have chosen to use the surface energy $\gamma_0 = 480$ erg/cm^2 [MELF56, ZANG88] which is the surface energy of liquid Pb in equilibrium with its vapor.

Equation (3.7), the above values for Ω and γ_0, along with my experimentally measured values of R_c and t_c yield the estimated values of D_s shown in Figure 3.14. These data are obtained from the same samples studied to make Figure 3.12. D_s is plotted vs. $T_{melting}/T$ since surface diffusion is an activated process which is expected to follow an Arrhenius type behavior of the form $D_s \sim D_0 \exp(-aT_{melting}/T)$ with $aT_{melting}$ proportional to the surface diffusion energy barrier. The two solid lines in Figure 3.14 indicate the range of previously measured values of D_s on fcc metals [BONZ83]. Considering the estimations involved in the KFM there is surprisingly good agreement of D_s with other studies. This is especially true since some of the previous studies used UHV environments with well cleaned and characterized samples. The upturn in my D_s values for $T \gtrsim 460$ K is a result of the inapplicability of the KFM in this temperature range.

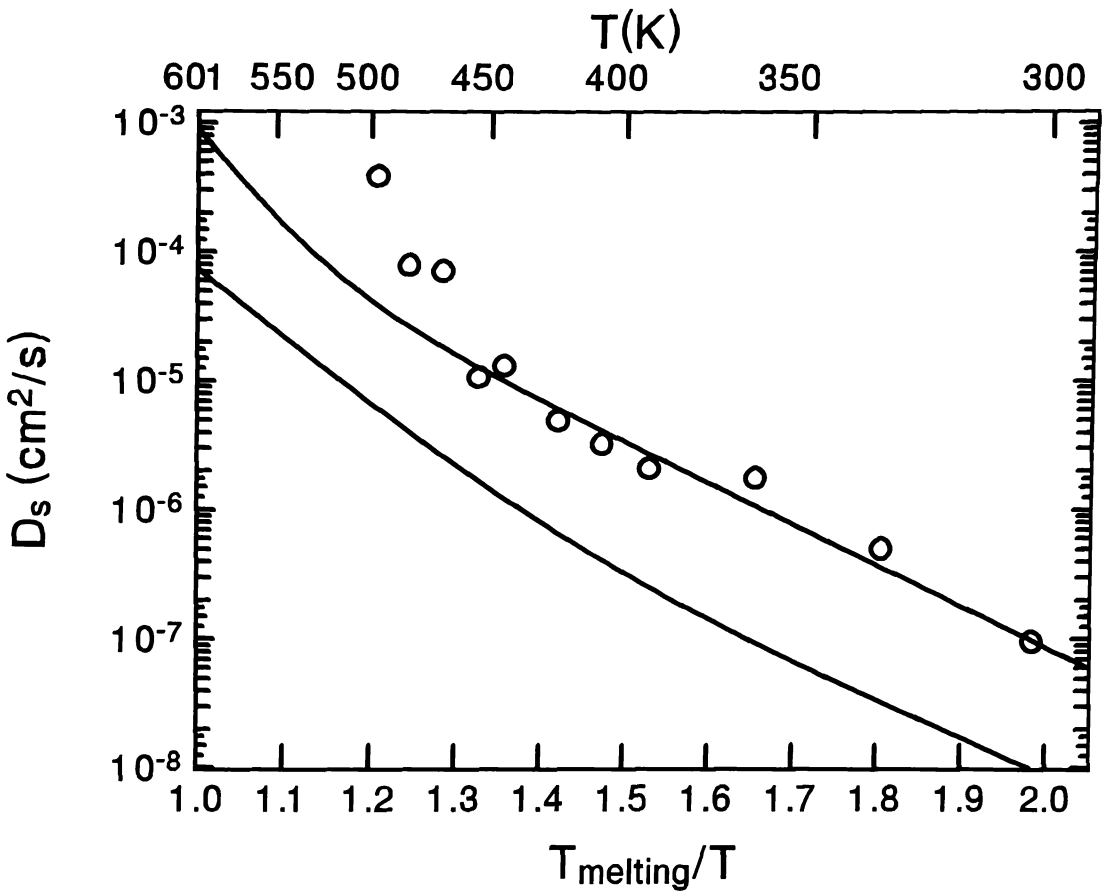

Figure 3.14 Plot of inferred D_s values as a function of $T_{melting}/T_{substrate}$. The solid lines show the range of D_s values measured on fcc metal surfaces [BONZ83].

3.7 MISSING INGREDIENTS OF THE KFM

The Kinetic Freezing Model is merely a "zeroeth order" approach. There are many important factors which have been neglected. As already mentioned, both the surface free energy γ_0 and the surface diffusion constant D_s are, in general, actually anisotropic. These were taken to be isotropic in the KFM. Two important elements missing from the KFM are the presence of substrate inhomogeneity and the trapping of grain boundaries within the interior of two coalescing droplets.

Roughness of the substrate can act to pin the droplet perimeters, thus impeding the coalescence. This is because during coalescence the droplet perimeter is effectively "dragged" across the substrate surface. If the surface is rough then more energy will be required to move the perimeter. Thus, unless the system has a high enough temperature to overcome this pinning action, coalescence will cease at a stage earlier than predicted by the KFM. This pinning may be caused by either topological or chemical inhomogeneity on the substrate surface. Since the amorphous substrates we used were determined, via AFM, to have a mean roughness of roughly 0.1 nm, chemical contamination is most likely the more important factor in these samples.

Some experimental observations indicate chemical contamination of the substrates to be present. Occasionally, samples which were prepared otherwise identically (cleaning, deposition rate, pressure, and thickness) exhibited different morphologies when viewed either optically or with the SEM. Also, some samples appeared to be strongly inhomogeneous. For example, regions of some films appeared to be percolating (or at least very well connected) while other regions of the same film were still in the compact island stage. This was not due to positions of differing thickness resulting from the thickness gradient on the samples. This effect is, we believe, due to nonuniform cleaning of the substrate. Prior to insertion of the cleaned substrates in the vacuum chamber, regions could be occasionally noticed which were obviously contaminated. This might

have been caused by incomplete dissolution of one of the cleaning agents used in cleaning the substrates, such as acetone or the MICRO cleaner.

Substrate inhomogeneity is only partly responsible for the formation of the metastable elongated metal structures. In forming a compact island from an initially elongated structure the surface energy gain (assuming isotropic γ_0) scales as R^2 with R being the island radius whereas the pinning energy is proportional to R, the perimeter length. Thus, it is doubtful that substrate pinning alone prevents full coalescence.

However, we know that grain boundaries are present during coalescence. The droplets form predominantly with the (111) face parallel to the substrate. But, the azimuthal orientation (about an axis normal to the substrate) is random due to the amorphous substrate. Thus, when two crystalline metal islands come into contact and begin to coalesce, a grain boundary forms in the interior of the composite island which extends through the bulk and down to the substrate. This causes the formation of a grain boundary groove to form at the surface of the metal islands. These grain boundaries are visible in images such as those in Figure 3.10. The boundaries are evidenced by regions of the elongated metal islands which narrow slightly near the grain boundary groove location. Removal of such a grain boundary from the intersection of two droplets requires a certain amount of energy. Often, the system temperature and the gain in surface energy if coalescence were completed is insufficient. In such a case, the grain boundary halts the coalescence process.

A large number of the grain boundaries created between two coalescing islands are high angle boundaries. Such high angle grain boundaries have a surface energy, γ_b, of roughly one-third the surface energy, γ, of the droplet material. It is possible to calculate the total energy of two compound islands with such an interior high angle grain boundary [DUXB94]. Such a plot is shown in Figure 3.15 which shows the total energy of two coalescing droplets, initially of the same radius but subject to a constant volume constraint, with a grain boundary trapped in the middle. In this plot, the dihedral angle, Ψ,

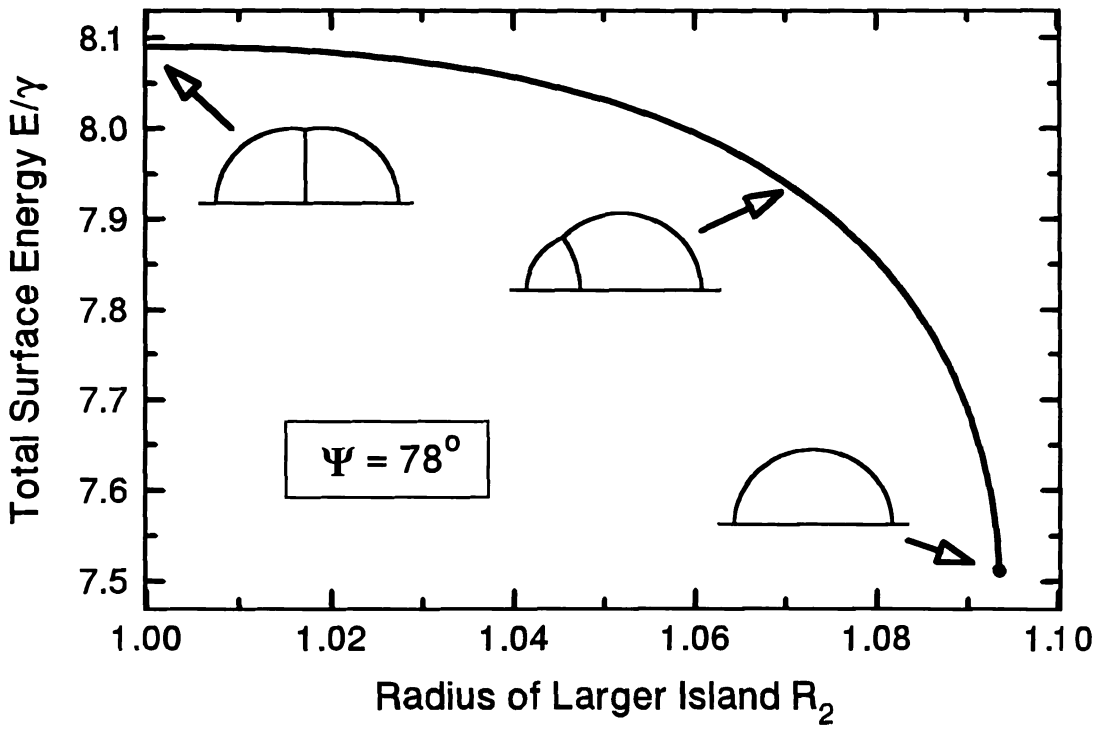

Figure 3.15 Surface energy of two coalescing droplets with an interior grain boundary having a dihedral angle, Ψ, of 78 degrees. The coalescence stage is shown in the accompanying schematic diagrams.

of the grain boundary is 78 degrees. The x-axis, labeled R_2, is the radius of the larger droplet in terms of the initial radius of each droplet. The equilibrium condition $\gamma_b = 2\gamma\cos\Psi$ causes the formation of the grain boundary groove and results in $\gamma_b \approx \gamma/3$ for $\Psi \approx 80°$. The important feature of this plot is the very slight gradient near $R_2 \approx 1$. This produces a small driving force for coalescence which can, thus, be pinned by weak substrate pinning along the island perimeter. A similar plot of surface energy vs. droplet size for the case of no grain boundary has a much larger driving force for coalescence since there are no impeding factors. Thus, substrate pinning and grain boundary pinning are not totally separate and a complete theory incorporating both effects is still lacking.

3.8 SUMMARY

In this chapter I have attempted to describe the growth and structure of thin metal films evaporated onto insulating substrates. A complete understanding of film growth in these systems requires explanation of many factors. These include the anomalously high area coverage at the percolation threshold, the island size for crossover from full to partial coalescence, sample annealing effects, as well as the effects of substrate inhomogeneity and grain boundaries.

Through a variety of computer simulations it was found that the keys to achieving a large value of p_c (as is observed in actual films) are coalescence, wiping, and the existence of the transition from full to partial coalescence. This ingredient yields values of p_c larger than ≈ 0.6 which could not be produced with normal lattice simulations.

Once the cause of high p_c was qualitatively understood, the size at which full coalescence ended was studied. For $T \lesssim 0.75T_{melting}$ this size, R_c, was found to have a weak temperature dependence. A simple *Kinetic Freezing Model* was presented which offers an intuitive understanding of this full to partial coalescence crossover. This viewpoint, that the coalescence time and the droplet growth time change dominance, is

not complete in that substrate and grain boundary effects are neglected. For temperatures above $T_0 \approx 460$ K the film morphology undergoes a change we do not fully understand. The significant change from a fairly uniform appearance to films with a dual structure may be due to an alteration in the substrate behavior (e.g. contamination or surface energy).

It was also found that the percolation coverage as well as the film appearance is dependent on the sample cooling rate. While even short annealing treatments have a significant influence on p_c, surprisingly little effect on R_c is observed. While p_c decreases during annealing the perimeter of the connected metal islands becomes much smoother as coalescence events continue after the end of deposition if the sample is still hot.

Finally, some ideas were presented on how the missing ingredients of the KFM might effect the results. These absent features are the presence of substrate roughness or inhomogeneity and grain boundaries which are trapped in the interior between two coalescing droplets. Neither of these issues is easily taken into account. However, we have made some initial progress in this direction.

A simple plot may help to sum up much of what has been discussed in this chapter. This plot, shown in Figure 3.16, shows the same data presented in Figure 3.12 in a different form. Here, R_c is taken as the independent variable and the corresponding substrate temperature T_c is that temperature at which the sintering stage (neck-filling) gives way to full coalescence. At a given R_c a certain substrate temperature is needed to overcome the effects of deposition and allow completion of coalescence. While coalescence of two solid droplets has been termed "liquid-like" since it is so rapid, Figure 3.16 shows that bulk melting of the droplets is negligible. Only droplets of size $\lesssim 10$ nm have their melting points significantly reduced below the bulk melting temperature of 601 K.

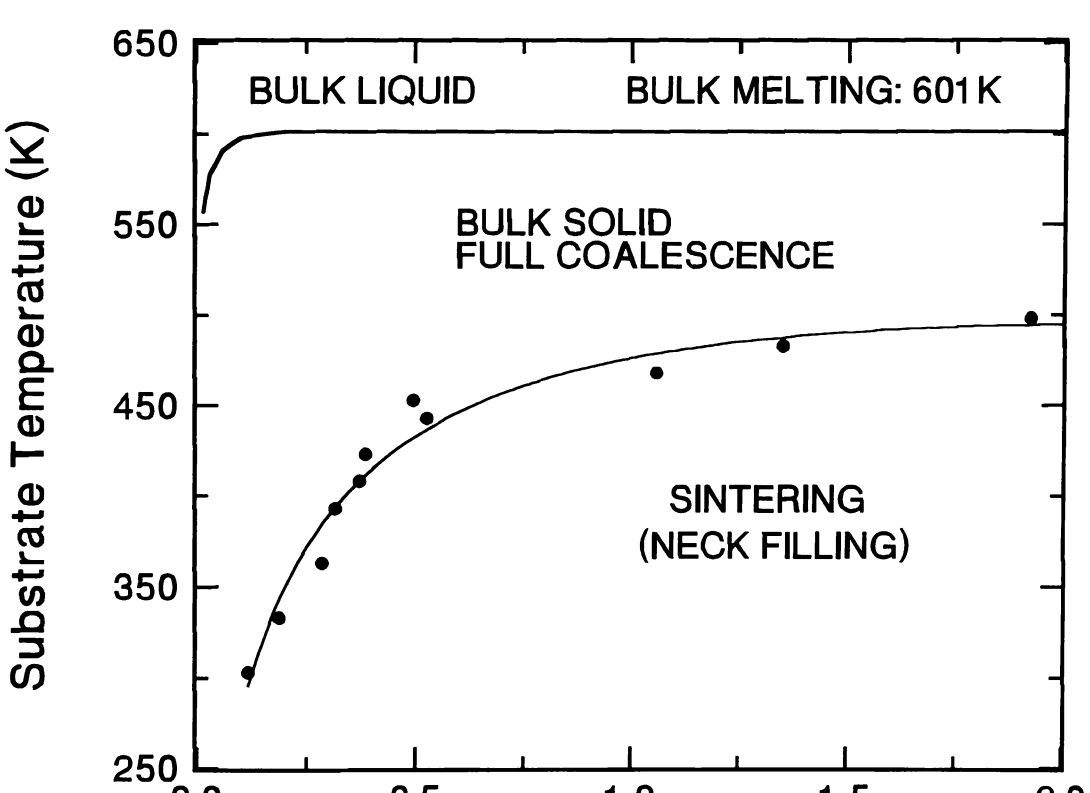

Figure 3.16 Plot of substrate temperature vs. R_c showing the different coalescence regimes. These Pb samples were deposited at 6 nm/s.

CHAPTER 3 REFERENCES

BASK94 A. A. Baski and H. Fuchs, Surface Science **313**, 275 (1994).

BEYS86 D. Beysens and C. M. Knobler, Phys. Rev. Lett. **57**, 1433 (1990).

BEYS91 D. Beysens, A. Steyer, P. Guenon, D. Fritter, and C. M. Knobler, Phase Transitions **31**, 219 (1991).

BONZ83 H. P. Bonzel, in *Surface Mobilities on Solid Materials: Fundamental Concepts and Applications*, edited by V. T. Binh, NATO ASI Series, Series B, Physics, Vol. 86, (Plenum Press, New York, 1983), p. 195.

CARR G. L. Carr, B. Caldwell, F. Family, and P. Meakin, (unpublished).

DUXB P. M. Duxbury and X. Yu, (unpublished).

DUXB94 P. M. Duxbury, M. Dubson, X. Yu, and G. Jeffers, Europhys. Lett. **26**, 601 (1994).

FAMI88a F. Family, in *Random Fluctuations and Pattern Growth: Experiments and Models*, edited by H. E. Stanley and N. Ostrowsky, NATO ASI Series, Series E, Applied Sciences, no. 157, (Kluwer Academic Publishers, Netherlands, 1988), p. 345.

FAMI88b F. Family and P. Meakin, Phys. Rev. Lett. **61**, 428 (1988).

FAMI89 F. Family and P. Meakin, Phys. Rev. A **40**, 3836 (1989).

GAWL81 E. Gawlinski and H. E. Stanley, J. Phys. A: Math. Gen., **14**, L291 (1981).

HERR51 C. Herring, in *The Physics of Powder Metallurgy*, edited by W. E. Kingston, (McGraw-Hill, New York, 1951), Chapter 8.

HEYR83 J. C. Heyraud and J. J. Metois, Surf. Sci. **128**, 334 (1983).

HEYR87 J. C. Heyraud and J. J. Metois, J. Crystal Growth **82**, 269 (1987).

HEYR89 J. C. Heyraud, J. J. Metois and J. M. Bermond, J. Crystal Growth **98**, 355 (1989).

JEFF94 G. Jeffers, M. A. Dubson, and P. M. Duxbury, J. Appl. Phys. **75**, 5016 (1994).

KAPI82 A. Kapitulnik and G. Deutscher, Phys. Rev. Lett. **49**, 1444 (1982).

KING55 W. D. Kingery and M. Berg, J. Appl. Phys. **26**, 1205 (1955).

LAIB82 R. B. Laibowitz, E. I. Alessandrini, and G. Deutscher, Phys. Rev. B **25**, 2965 (1982).

LEWI78 B. J. Lewis and J. C. Anderson, *Nucleation and Growth of Thin Films*, (Academic Press, New York, 1978).

MELF56 D. A. Melford and T. P. Hoar, J. Inst. Metals **85**, 197 (1956).

METO82a J. J. Metois and J. C. Heyraud, J. Crystal Growth **57**, 487 (1982).

METO82b J. J. Metois, G. D. T. Spiller, and J. A. Venables, Phil. Mag. A **46**, 1015 (1982).

METO89a J. J. Metois, S. Nitsche, and J. C. Heyraud, Ultramicroscopy **27**, 349 (1989).

METO89b J. J. Metois and J. C. Heyraud, Ultramicroscopy **31**, 73 (1989).

MULL57 W. W. Mullins, J. Appl. Phys. **28**, 333 (1957).

MULL59 W. W. Mullins, J. Appl. Phys. **30**, 77 (1959).

NICH65 F. A. Nichols and W. W. Mullins, J. Appl. Phys. **36**, 1826 (1965).

NICH66 F. A. Nichols, J. Appl. Phys. **37**, 2805 (1966).

OHRI92 M. Ohring, *The Materials Science of Thin Films*, (Academic Press, San Diego, 1992).

PASH64 D. W. Pashley, M. J. Stowell, M. H. Jacobs, and T. J. Law, Phil. Mag. **10**, 127 (1964).

PASH65 D. W. Pashley, Adv. Phys. **14**, 569 (1965).

PASH66 D. W. Pashley and M. J. Stowell, J. Vac. Sci. Technol. **3**, 156 (1966).

STAU85 D. Stauffer, *Introduction to Percolation Theory*, (Taylor and Francis, London, 1985).

VOSS82 R. F. Voss, R. B. Laibowitz, and E. I. Alessandrini, Phys. Rev. Lett. **49**, 1441 (1982).

WOLL93 D. A. Wollman, M. A. Dubson, and Q. Zhu, Phys. Rev. B **48**, 3713 (1993).

YU91 X. Yu, P. M. Duxbury, G. Jeffers, and M. A. Dubson, Phys. Rev. B **44**, 13163 (1991).

ZANG88 A. Zangwill, *Physics At Surfaces*, (Cambridge University Press, Cambridge, 1988).

CHAPTER 4

POSSIBLE FUTURE DIRECTIONS
Further experiments related to thin film growth and structure

4.1 INTRODUCTION

Clearly, the film growth work presented in this thesis is incomplete. A small portion of a very large parameter space has been studied with much remaining. The two most obvious directions which could be pursued as extensions of this work concern the factors absent in the Kinetic Freezing Model. These are substrate inhomogeneity and the influence of grain boundaries upon the sample growth and morphology. Other issues such as deposit material and deposition rate are more specific and, thus, of lower priority.

4.2 SUBSTRATE INHOMOGENEITY

One very important factor in this research has been the sample preparation conditions. The background pressure during sample deposition was in the range 10^{-6} to 10^{-7} mbar. A pressure of 10^{-6} mbar corresponds to roughly one monolayer of contamination coating the sample surface every second [OHAN89]. This issue is mainly relevant at the deposit-substrate interface. The deposition rates of generally $\geq$ 2 nm/s correspond to at least six monolayers of deposit material being added to the sample surface every second which is larger than the contamination rate. Thus, it is possible that a significant number of impurities are trapped within the film during growth. In addition, although the deposit materials are usually of 99.999% purity, this small impurity concentration may be significant if it is able to migrate to the surface of the growing film. Contamination from regions of the vacuum chamber which are heated by the deposition

source, as discussed in Section 2.2, probably influence the film's composition. However, metals of higher purity are more difficult and much more costly to obtain. In order to significantly reduce the background contamination present in the vacuum chamber, use of an improved vacuum system is necessary.

Modern vacuum technology enables the background pressure to be significantly diminished with the proper equipment. Design and construction of such a system was pursued during this research and will be described briefly below.

Ultrahigh vacuum can be fairly easily achieved these days. Diffusion pumps such as that on our evaporation system have a lower ultimate pressure typically $\sim 10^{-8}$ mbar. Completely oil-free environments require the use of either ion pumps or turbomolecular pumps. I designed a UHV sample deposition system centered around the ideas of using a stainless steel chamber and an ion pump to achieve pressures below 10^{-9} mbar, thus reducing the present contamination rate by roughly a factor of 1000. The stainless steel chamber is necessary since baking of the system (to outgas the chamber's interior) is required to reach such low pressures. In addition to the pumping elements, this system was to contain similar features as the present evaporator. These were to include two deposition sources, a film thickness monitor, and sample stages. Very precise control of the deposition rate can be obtained through use of a Knudsen effusion cell such as those used in Molecular Beam Epitaxy (MBE) systems. However, this extreme controllability is quite expensive, on the order of $10,000. Since this was outside our available funds, we were going to attempt building a small enclosed source in hopes of mimicking the isothermal environment of the effusion cell. Since flux control was not a major problem in the existing setup, this approach was deemed adequate. Due to the long times required for pumpdown to the ultimate pressure before deposition (roughing, baking, pumping) it was desired to have multiple sample stages located in the chamber. Additionally, these stages would have a small thermal mass and very rapid heating and cooling rates compared to the present heater stage. This feature could also prove useful for future

experiments requiring fine temperature control. A technique [SCHW93] whereby two thin film thermometers (TFD's) are used on each stage was tested. In such an arrangement, one TFD is used as the sample heater while the other is used as the thermometer. Because of the small size of these thermometers (10.2 x 3.3 x 0.5 mm^3), use of two of these enabled a very small, light sample stage to be fabricated. Rather than a "big Cu block" all that is needed is a small support structure, the two TFD's, and the substrate. A prototype stage was assembled with a mass of only 5 grams. The thermal response of this structure was much better than the present stage. Starting at room temperature this heater could be stabilized at a temperature of 100 °C in roughly half a minute with an input power of roughly 0.1 W. The cooling rate was about 30 K/minute without use of a "cold finger" as in the present quenching method. With an improved design these numbers could undoubtedly be improved. The plan was to suspend at least three of these sample stages in the chamber on a rotary feedthrough to enable each sample to be prepared independently of the others. After deposition the samples would be analyzed in the same manner presently used.

Since substrate inhomogeneity can be topological as well as chemical, an *in situ* device for sample roughening and cleaning was also considered. Using an ion mill gun, the sample could be bombarded by ion doses of various ionic species, energy, and duration times. Again, this equipment was quite expensive. Fortunately, an ion milling system already exists within the department which we planned to use, instead, for substrate surface roughening prior to insertion of the samples into the evaporation chamber. Tests were performed with various ion treatments using this system. Surface topology deformations ~ 0.1 μm were easily formed on SiO_2 substrates as observed with an SEM. Much smaller dimensions are undoubtedly achievable with more detailed tests. Typical dimensions in the percolating films are presently ~ 0.1 to 1 μm so that smaller dimensions would be needed.

These above ideas could also be applied to the case of an insulating, crystalline substrate such as quartz (SiO_2) or sapphire (Al_2O_3). Generally, metals do not wet insulating surfaces. However, if the lattice parameters are close enough, more nearly layer-by-layer growth than that observed on amorphous substrates might be achieved.

4.3 GRAIN BOUNDARY AND COALESCENCE STUDIES

The second major issue of concern is that of grain boundaries and the effect of their presence on the coalescence process. A few ideas as to how to study these issues are presented below.

Since the substrates used are amorphous, crystalline islands grow with random orientations. Variations exist in the crystallite's orientation both in terms of what face is parallel to the substrate and the azimuthal rotation. Both of these factors determine the orientation of the grain boundary which is formed when two crystallites touch and begin to coalesce. If pinning by such a grain boundary is important, quantitative information on the boundary's mobility would be useful in learning to control film growth.

Two single crystal regions with an interior grain boundary have an electron diffraction pattern characteristic of the two orientations present. These two crystal orientations may be observed using a Transmission Electron Microscope (TEM). Since different composite islands will contain different grain boundaries and orientations, data on many different islands would be required to obtain information regarding the average orientation. This might be achieved, inside a TEM, through the use of selected area diffraction where the diffraction information from a small area of the sample is investigated. There are two problems with this approach. First, the random orientation will complicate determination of one or both crystal alignments. Secondly, use of a (TEM) would limit the material thicknesses which could be studied. Sample thicknesses of roughly 10 nm or greater are not compatible with the TEM's such as that in the Physics

Astronomy Department since the maximum beam energy of roughly 100 keV is insufficient to penetrate such thicknesses, particularly in a dense material such as Pb. A similar measurement could be made using electron channeling. However, channeling also requires further initial orientation information. We also have no access to a microscope with channeling capabilities.

Another method, involving the use of x-ray scattering, might be used to obtain information regarding the crystallite orientation distribution, but not that of the grain boundaries. The x-ray system in the Michigan State University Chemistry Department has rotation capability about one axis which allows normal θ - 2θ scans. Thus, two scans might be needed with the sample rotated 90° about the substrate normal during the successive scans. Through measurement of the relative intensities of different Bragg peaks, quantitative information could be obtained regarding the orientation distribution which could be correlated with the film morphology. A drawback of this technique is that long collection times might be necessary. Because the film is not continuous and contains many crystals (of very small size relative to the x-ray beam diameter) of different orientations, the signal to noise ratio would be small. Access to an x-ray goniometer with rotation capability about the polar and azimuthal axes would simplify this approach considerably.

A method also exists whereby information about the grain boundary pinning strength and diffusion may be obtained. The idea is to observe the coalescence process inside an electron microscope. Lead is a good candidate for this type of experiment due to its low vapor pressure; little material would contaminate the SEM chamber, especially the electron beam column. Using photolithography, a sample could be prepared which consists of two metal islands which just touch. This sample would be mounted on a heatable stage inside an SEM. By adjusting the temperature, the process of coalescence could be controlled while imaging the process. The grain boundary formed between these two crystals can be easily detected in the SEM image. Once formed, observations could

be made of the boundary's movement, particularly the time and temperature dependencies for movement out of the compound island. This could provide information about the grain boundary's pinning and migration energies. As the process of coalescence is generally quite fast, a few precautions must be taken. The droplet size could be made large enough so that the coalescence occurs on a time scale compatible with observation. This would also be a continuous process so that a more efficient imaging scheme would be needed than the present snapshots which are taken. This could be done by splitting the electron detector signal to a video system (or another monitor) which could be videotaped at speeds of roughly 1/30 second. There are also potential problems with this method. The sample would have to be cleaned once inside the SEM chamber to eliminate contamination produced after removal from the evaporation chamber. This could be done using either *in situ* UV/ozone cleaning or gas jet cleaning. Gas jet cleaning relies on the interaction of a gas jet, which is directed onto the sample, with the incident electron beam to clean the sample surface. Because the SEM reaches an ultimate pressure comparable to that inside the evaporation chamber, the coalescence dynamics should be similar *if the initial contamination can be eliminated.*

An alternative approach for studying some aspects of grain boundary dynamics is to use an STM and compatible materials. This could be done for Au or Ag on a graphite substrate. For a given substrate temperature during deposition these metals will have a smaller grain size than Pb which would enable inspection of many more crystallites using the STM. Also, graphite is not an insulating, amorphous substrate. The film growth would be different since ordered island structures might be produced as have been observed for Pb on graphite [METO82]. The STM we have in our laboratory would limit real time observations of the coalescence process because the image acquisition time is at least 15 seconds or more.

4.4 SUMMARY

The possible experiments presented in this chapter are insufficient to fully understand the growth of metal films on insulating substrates. However, they are experiments which we have considered performing as we feel the results could prove beneficial in light of some of the results observed during the course of this research. Additionally, we are unaware of experiments of this nature having been previously performed.

Numerous experiments were performed in the 1960's dealing with film nucleation and structure [PASH66, INUZ69]. These were mainly *in situ* experiments where the sample was observed during deposition inside the chamber of an SEM or TEM. The presence of the electron beam was found to increase the island nucleation rate most likely due to the increased contamination produced by the interaction of the electron beam with hydrocarbons in the chamber [CHRI60]. Other studies have dealt with the crystallite alignment's relative to the substrate and its behavior during coalescence. The resulting structure of films prepared *in situ* or observed after removal from a thermal evaporation system were found to be similar [PASH64]. These types of experiments are more complicated than observing *ex situ* to the deposition chamber and yield similar results.

Were the experiments discussed in this chapter carried out they may help to quantify various parameters controlling continuous film formation. Controlled experimentation may lead to the production of high quality, perhaps technologically useful, films.

CHAPTER 4 REFERENCES

CHRI60 R. W. Christy, J. Appl. Phys. **31**, 680 (1960).

METO82 J. J. Metois and J. C. Heyraud, J. Crystal Growth **57**, 487 (1982).

INUZ69 T. Inuzuka and R. Ueda, J. Vac. Sci. Technol. **6**, 379 (1969).

OHAN89 J. F. O'Hanlon, *A User's Guide To Vacuum Technology*, Second edition (John Wiley & Sons, New York, 1989).

PASH64 D. W. Pashley, M. J. Stowell, M. H. Jacobs, and T. J. Law, Phil. Mag. **10**, 127 (1964).

PASH66 D. W. Pashley and M. J. Stowell, J. Vac. Sci. Technol. **3**, 156 (1966).

SCHW93 R. B. Schwarz and J. B. Rubin, Rev. Sci. Instrum. **64**, 1292 (1993).

CHAPTER 5

PROFILE DECAY DUE TO SURFACE DIFFUSION AT LOW TEMPERATURE

Computer simulations of mass transport on a stepped surface

5.1 INTRODUCTION

We have performed computer simulations of the decay of a sinusoidal profile in (1+1)D in an attempt to obtain a better understanding of the dynamics controlling surface diffusion on a corrugated surface below the roughening temperature. While Monte Carlo simulations of profile relaxation have been previously performed [JIAN89, SELK93] in this temperature regime, neither conclusive evidence of faceting nor the decay time scaling relation has been found. Monte Carlo simulations which rely upon analytical results for a one-dimensional random walk are discussed. These analytical results, derived via rate equations in Section 5.3, or using an electric circuit analogy in Section 5.7, determine the various movement probabilities for individual atoms depending upon their local environment. Thus, atom motion is "instantaneous," eliminating the need to track an atom's entire random walk. The simulations are a novel attempt to study surface diffusion dynamics below the roughening temperature. Long-ranged step-step interactions are absent in our model. However, a contact interaction is present because steps of like sign cannot cross in this solid-on-solid model. This interaction leads to an entropic repulsion between steps. The results differ from those for the high temperature (above the roughening temperature) regime. Similarities between this model and other studies are discussed.

5.2 BASIS OF THE SIMULATION ALGORITHM

Most simulations of film growth and/or surface diffusion are based upon the Monte Carlo algorithm. The method is called Monte Carlo as it is based upon randomly chosen events. As an illustration of this method consider the motion of a single atom, initially at the origin, random walking among the sites of a square lattice, which are allowed to have different binding energies. Furthermore, restrict the atom's motion to its nearest neighbor sites which determine the local energy landscape. One possible question of interest is how long this single adatom will take to move a certain distance from the origin or to a given position. At each movement opportunity four possible jump directions exist. The direction in which to attempt a jump is chosen randomly. The actual decision to jump is based upon the Boltzmann factor, $e^{-\beta\Delta E}$, where $\beta = (k_B T)^{-1}$ and ΔE is the binding energy difference between the final and initial sites, $\Delta E = E_{final} - E_{initial}$. Should this energy difference be less than or equal to zero the walker is allowed to move to the final position. That is, movement to a position of equal or higher binding energy occurs with probability one if that direction is chosen. However, some sites have lower binding energies so that these sites are energetically costly to occupy. This is where the Boltzmann factor becomes necessary. If $\Delta E \geq 0$ the walker moves to the final position with a probability of $e^{-\beta\Delta E}$. Comparison of a random number, which is uniformly distributed in the range $0 < r < 1$, to this Boltzmann factor determines whether the movement occurs. If the random number is less than $e^{-\beta\Delta E}$ the move is allowed. This cycle of allowing the walker to move is continued until the adatom reaches the desired location. This algorithm is easily extended to the case with more than one adatom present. Then, individual walkers are interrogated in random order after the completion of the previous walker's journey or after a single movement attempt by the previous adatom.

Monte Carlo methods may be very inefficient in cases where the only points of interest are the starting and finishing positions. The reason for this inefficiency arises from

the need to track the entire random walk of the diffusing atom. Our simulation algorithm avoids the need to follow each random walker through its entire journey. Instead, the relevant probabilities (to be discussed in Section 5.3) for different types of movement can be calculated for every walker based on its local environment. This feature results in a large decrease in the necessary computational time.

The basis of our model [DUBS94a] is that a wandering adatom on a crystal surface experiences a different local environment near a monatomic step than when located on a flat terrace. This may be understood simply by the difference in numbers of nearest neighbors (NN) and next nearest neighbors (NNN) between these respective positions. Figure 5.1 demonstrates this for both a triangular and a square lattice. Also shown are the position dependent binding energies for adatoms on both surfaces.

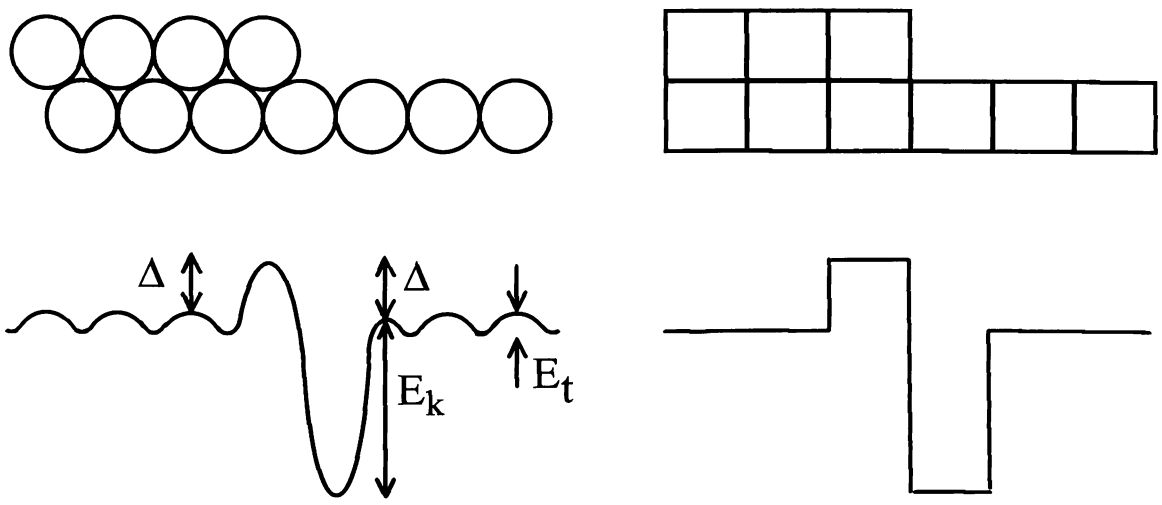

Figure 5.1 Binding energy diagrams near a monatomic step for the triangular and square lattices. Δ is the Schwoebel barrier. E_k and E_t are described in the text.

A barrier, denoted by Δ, exists between the last binding position on the top side of the step and one position to its right. This so-called Schwoebel barrier [SCHW66, 69] makes it more difficult for an atom to move down to the next terrace. Embedded atom

calculations [LIU93] confirm the qualitative form of this adatom potential. Also shown in Figure 5.1 are the terrace corrugation energy barrier, E_t, and the binding energy of a kink site, E_k. The Schwoebel barrier arises from a missing NNN to the last binding site on the upper terrace relative to a site one position to its left.

Some controversy exists over the nature and size of the Schwoebel barrier. Field Ion Microscopy (FIM) has been the primary experimental tool for observing the influence of this barrier upon surface diffusion of single adatoms. In 1966 Ehrlich and Hudda [EHRL66a] were the first to observe an adatom reflecting from the top side of a step edge. This occurred for W adatoms on different crystal faces of a W surface. The amount of reflection depended upon the step direction and it was concluded that an energy barrier of $\approx$0.06 eV more than the energy barrier for open-terrace diffusion could cause the observed behavior. Tsong measured [TSON72] Δ and E_t for Re diffusion on W(123) at 364 K and found $\Delta \approx 0.05$ eV and $E_t \approx 0.88$ eV. Thus, in this case Δ is small compared to the diffusion barrier E_t which is usually $\gtrsim$0.5 eV. Fink and Ehrlich [FINK84] discovered that for W and Re adatoms on W(211) there exists a preferential binding of the adatom at the first or second topside binding position from the step. However, they did not look at adatoms descending down a step so that no information regarding the Schwoebel barrier was determined. In a series of papers [WANG91, 93a, 93b] Wang and Ehrlich studied the behavior of Ir and W adatoms near the boundaries of Ir clusters of differing sizes using FIM. Their results show that a step acts as a funnel for migrating adatoms. That is, adatoms approaching an ascending step experience a gradually decreasing energy barrier as they approach the step. This causes an increased flux of atoms to the step edge On the other hand, an atom approaching a descending step also feels a decreasing energy barrier close to the step edge, but not at the edge. At the step edge the barrier to move down the step is larger. The authors above also observed that the size of the terrace is important. Small terraces show complicated behavior near their centers due to possible long range effects of the step edges. Kunkel *et al* [KUNK90] and

Bott *et al* [BOTT92] postulated Schwoebel barrier effects to explain their observations of reentrant layer-by-layer growth of Pt on Pt(111) homoepitaxial films. While being far from completely understood, the Schwoebel barrier has been experimentally shown to influence adatom behavior near step edges.

The system used for the simulations to be discussed here is a (1+1)D solid-on-solid (SOS) square lattice at low temperature. The (1+1)D means the height z of the system is characterized by z(x, t) where x is the horizontal direction in Figure 5.1 and t is time. Such a system is physically unattainable as it would require a stack of matter one atom wide, but is meant to mimic the behavior of a full three-dimensional system having straight, parallel grooves in the y-direction. Our algorithm is most applicable to a (1+1)D system. Here, low temperature means: 1) terrace atoms (those with two in-plane NN) are not allowed to activate and become walkers on the surface and 2) there is only one walker present on the surface of the sample at any time. These two restrictions prohibit roughening of the surface and island nucleation.

Kink site atoms are the only atoms in these simulations which are allowed to activate and become random walkers on the surface. Kink site atoms are those located at the end of a terrace and have one less in-plane NN than other surface sites. Neglecting the activation of atoms embedded in terraces (with two in-plane NN's) keeps this (1+1)D system from roughening which would otherwise occur at non-zero temperatures for a one-dimensional system. The roughening temperature T_R is that temperature at which a given crystal face can no longer maintain a faceted surface. At and above T_R terrace atoms activate without effecting the total system free energy so that the facet which was present below T_R becomes lost. The roughening temperature concept will be discussed in more detail later. Since the model is at low temperature and we are neglecting the effects of evaporation-condensation, the total number of atoms in the system is conserved. Evaporation-condensation and volume diffusion are also negligible [PASH66] for temperatures well below the melting temperature as is the case here.

The energies controlling the temporal dynamics are the terrace diffusion energy, E_t, and kink site activation energy, E_k, as shown in Figure 5.1. Since $E_k \gg E_t$, kink site activation times are much longer than the diffusion times of atoms on open terraces. In order for the random walk time of a single adatom on a flat, open terrace, τ_{diff}, to be very fast compared to the kink site activation time the condition which must be satisfied is $L^2 e^{\beta E_t} \ll e^{\beta E_k}$ where L is the terrace width in units of the lattice constant. This condition leads to $\beta \gtrsim \ln(L^2)/E_k$ since E_t is small compared to E_k. With $L \approx 10 - 100$ this yields $k_B T < E_k/10$. Recent calculations [LIU92] estimate, for low-index Ni surfaces, $E_k \approx 0.7 - 0.8$ eV so that $T \lesssim T_{melting}/2$ corresponds to a single walker on a terrace at any given time. Experimentally, detachment times are found [BART93, POEN92] to be much longer (roughly 100 to 1000 times) than diffusion times. Thus, an atom random walks over a terrace in a time much faster than the time between subsequent kink detachment events, τ_{det}. In addition, these two processes occur simultaneously so that the time unit may be taken as τ_{det}. If there are N active sites (kink sites which may move) the average time between kink site activation events is $\tau = \tau_{det}/N = 1/N$. Thus, after an atom is moved the simulation time is incremented by an amount $\tau = 1/N$.

5.3 MOVEMENT TRAJECTORIES AND PROBABILITIES

Figure 5.2 shows a typical portion of a stepped surface encountered during the decay process along with the relevant distances and possible movement trajectories of the solid kink site atom shown. The position one lattice spacing to the right of the kink site is a *well site* as it is a position of higher binding energy than anywhere else on a terrace. Well sites are empty surface sites with two NN and two NNN's. L_l and L_r denote the terrace widths to the left and right, respectively, of the activated atom. The trajectories labeled 1, 2, r, and *l* indicate the four different possible paths which might be taken by the activated atom.

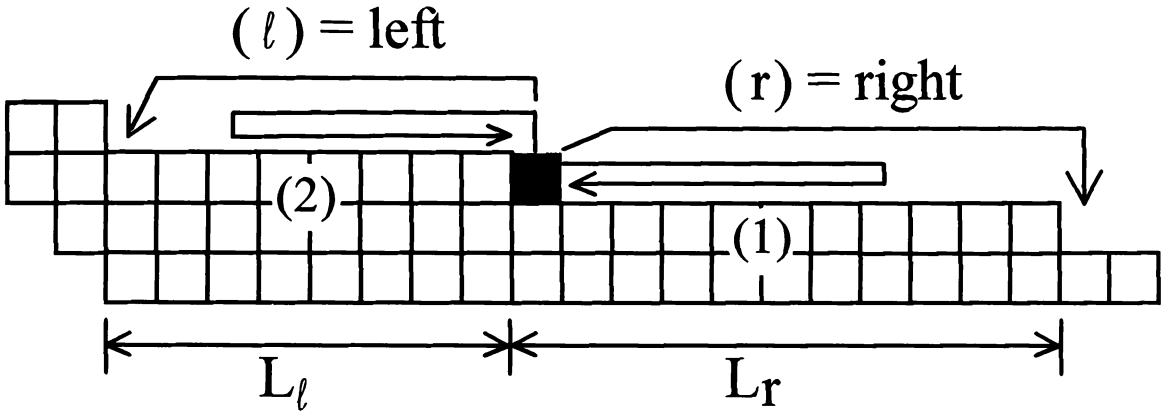

Figure 5.2 Typical environment of an activated kink site atom (shown as the solid square). The four possible movement trajectories and the terrace widths, as discussed in the text, are also shown.

An activated atom such as that shown in Figure 5.2 will follow one of four trajectories. Path number 1 involves activation of the atom out onto the terrace, a subsequent random walk on this terrace, including possible reflections due to the Schwoebel barrier at $+L_r$, and finally a return to the original site. Path 2 is similar to path 1 except that here the kink site activates up onto the top terrace. After a meandering random walk on this upper terrace the atom finally overcomes the barrier near where it started and returns to its original position. Paths 1 and 2 result in no contribution to the net mass flow of the system as structurally the system is unchanged after either of these two movements. Path r results in the activated atom passing over the barrier at $+L_r$ and incorporation into the step edge at $+L_r$. Finally, path ℓ entails movement onto the upper terrace and inclusion at the well site located at $-L_\ell$. In all that follows the four paths 1, 2, r, and ℓ will be designated by the subscripts 1, 2, r, and ℓ, respectively.

Due to the presence of the Schwoebel barrier near a kink site, activation out onto the lower terrace (to the right in Figure 5.2) is more likely than activation up onto the upper terrace (to the left in Figure 5.2). As can be seen in Figure 5.1, activation to the upper terrace requires the atom to overcome a barrier which is larger, by an amount Δ,

than that to activate onto the lower terrace. Activation out onto a terrace occurs with probability O while activation onto the upper terrace has a probability U. Clearly, U and O must satisfy the condition that $U + O = 1$. The barrier presence causes $O \geq U$ with the ratio of the two probabilities given by the Boltzmann factor, $U/O = e^{-\beta\Delta}$. This barrier also acts to reflect walkers incident from the upper terrace side since at the step edge the walker sees a larger barrier, again by an amount Δ, to move down the step than to reflect. Thus, we define the reflection coefficient, k, via $U/O = e^{-\beta\Delta} = 1 - k$. Since $U + O = 1$, $O = 1/(2 - k)$ and $U = (1 - k)/(2 - k)$. If, for example, $\Delta = 0$ then $U = O = 1/2$. For the measured value [TSON72] of $\Delta = 0.052$ eV for Re on W(123) at 364 K, $k \approx 0.8$ is found.

The behavior of a one-dimensional random walker in the presence of reflecting and/or absorbing barriers has been solved exactly by Chandrasekhar [CHAN43, EHRL66b]. Our method is much simpler than Chandrasekhar's in that straightforward rate equations are used to determine the effect of these barriers on a random walker as opposed to a detailed statistical analysis. Prior to development of the rate equation method described below, Professor Hetherington [HETH93] formulated an equivalent, albeit more mathematical, scheme of determining the various movement probabilities. This formulation treats each walker as a Markov process and used the transfer matrix method [DOYL84] to find the relative movement probabilities. This Markov chain method was much more complicated than the rate equation approach and, thus, dropped in favor of a simpler, but equivalent, approach. As fate would have it, during the writing of this thesis yet another, even simpler, method was discovered. This scheme will be discussed briefly in Section 5.7.

Consider paths 1 and r as shown in Figure 5.2. This situation is shown along with a coordinate system in Figure 5.3. Path 1 involves movement of the black activated atom from $x = 0$ out onto the terrace and a subsequent return to $x = 0$. Path r, however, occurs if the atom makes it over the barrier at the step edge between $x = L - 1$ and $x = L$.

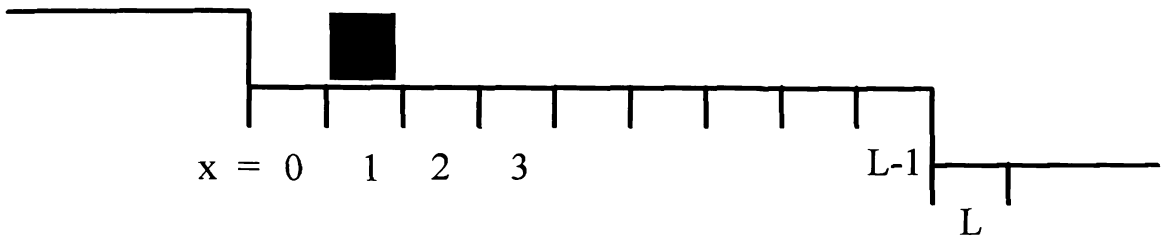

Figure 5.3 Coordinate system for an adatom on a terrace of width L.

I will now set up and solve the rate equations needed to find the movement probabilities for paths 1 and r. These probabilities are denoted by P_1 and P_r, respectively. Following activation of a kink site at x = 0 we have the case depicted in Figure 5.3. In determining the movement probabilities it is useful to envision a continuous stream of non-interacting atoms emanating from a source at x = 1 and walking amongst scattering centers at x = 1, 2,..., L − 1 prior to capture at x = 0 or x = L. The probabilities P_1 and P_r will be given by the fractions of atoms absorbed at the sinks, x = 0 and x = L, respectively. Let c denote the rate of walker production at x = 1. By N_i we represent the number of atoms arriving per unit time at x = i. The absorption rates at x = 0 and x = L are a_0 and a_L, respectively. Conservation of matter requires that $c = a_0 + a_L$. The probabilities are $P_r = O(a_L/c)$ and $P_1 = O(a_0/c)$ with O being the probability of activation onto the lower terrace as described earlier in this section. The rate equation for x = 0 is

$$a_0 = \frac{c}{2} + \frac{N_1}{2}. \tag{5.1}$$

This is because half of all the atoms at site x = 1 will move to x = 0. For x = 1 only atoms scattered from x = 2 are incident so that

$$N_1 = \frac{N_2}{2}. \tag{5.2}$$

For x = 2 we have

$$N_2 = \frac{c}{2} + \frac{N_1}{2} + \frac{N_3}{2}, \tag{5.3}$$

and for x = 3,

$$N_3 = \frac{N_2}{2} + \frac{N_4}{2}. \tag{5.4}$$

This pattern may be continued for subsequently higher values of x. The absorption rate at x = L is given by

$$a_L = \frac{N_{L-1}}{2}(1-k) \tag{5.5}$$

since only a fraction (1 − k) of atoms at site x = L − 1 make it to x = L. Equations (5.1) to (5.4) may be combined to yield the following recursion relation for N_i,

$$N_i = 2ia_0 - 2(i-1)c, \quad i = 2, 3, 4, ..., L - 1. \tag{5.6}$$

Insertion of (5.6) into (5.5) yields

$$a_L = (1-k)[(L-1)a_0 - (L-2)c]. \tag{5.7}$$

Finally, since $c = a_0 + a_L$, equation (5.7) may be solved for a_L/c,

$$\frac{a_L}{c} = \frac{1-k}{1+(1-k)(L-1)}. \tag{5.8}$$

This was for a general terrace of width L whereas in the simulations this width is denoted by L_r. If we now define $\eta_r = 1 - (1/L_r)$, and multiply equation (5.8) by O, then P_r may be expressed as

$$P_r = \frac{O}{L_r}\frac{(1-k)}{(1-\eta_r k)}. \tag{5.9}$$

Now, since $P_r + P_1 = O$, equation (5.9) may be used to find

$$P_1 = O\frac{\eta_r(1-k)+k(1-\eta_r)}{1-\eta_r k}. \tag{5.10}$$

Thus, we have the two probabilities involving kink site movement out onto the lower terrace. Using the procedure outlined above the probabilities for trajectories 2 and *l* in Figure 5.2 may also be calculated. These probabilities turn out to be

$$P_2 = U\frac{\eta_\ell(1-k)}{(1-\eta_\ell k)} \tag{5.11}$$

and

$$P_\ell = \frac{U}{L_\ell}\frac{1}{(1-\eta_\ell k)}. \tag{5.12}$$

Equations (5.9) to (5.12) obey $P_1 + P_2 + P_r + P_\ell = 1$ as they must.

Other environments occur in which an activated kink site atom does not have an environment such as that shown in Figure 5.2. For example, at the extrema of the corrugated surface atoms may, instead, be caught between two reflecting or two absorbing barriers as illustrated in Figure 5.4. These environments are simply taken care of in the rate equation approach by effectively changing the boundary conditions (similar to a_0 and a_L above).

Consider the two situations shown in Figure 5.4. The case on the left corresponds to activation of a kink site onto the topmost terrace, which subsequently moves down the step at the other end with a probability of

$$P_\ell = \frac{U}{1+k+(1-k)L_\ell}. \tag{5.13}$$

The case shown on the right of Figure 5.4 corresponds to a walker trapped between two absorbing barriers. In this case the movement probability is,

$$P_r = \frac{O}{L_r - 1}. \tag{5.14}$$

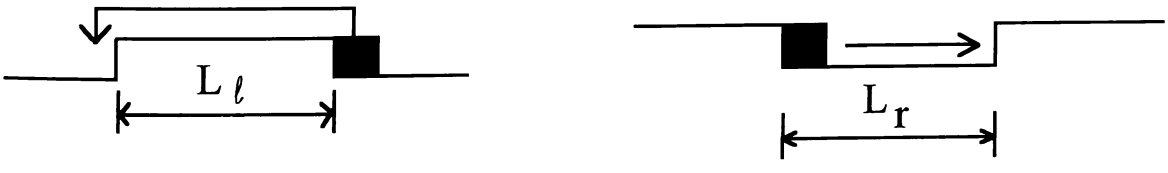

Figure 5.4 Environments of kink site atoms in the topmost (left) and bottom (right) terraces.

The final environment that must be considered is that of an isolated walker atop a terrace. This occurs as the final step in the disappearance of a terrace. When a dimer rests upon a terrace, eventually one of the two will be activated and may move away from its partner. When this happens, the single remaining atom on the terrace will immediately diffuse off the terrace as shown in Figure 5.5.

Here, the single walker is trapped between two reflecting barriers. Using the appropriate rate equations this single atom has a probability

$$P_r = \frac{1+L_\ell(1-k)}{2+(L_r+L_\ell)(1-k)} \tag{5.15}$$

of being incorporated at the step to its right. The walker will move to the left side step with probability $P_\ell = 1 - P_r$.

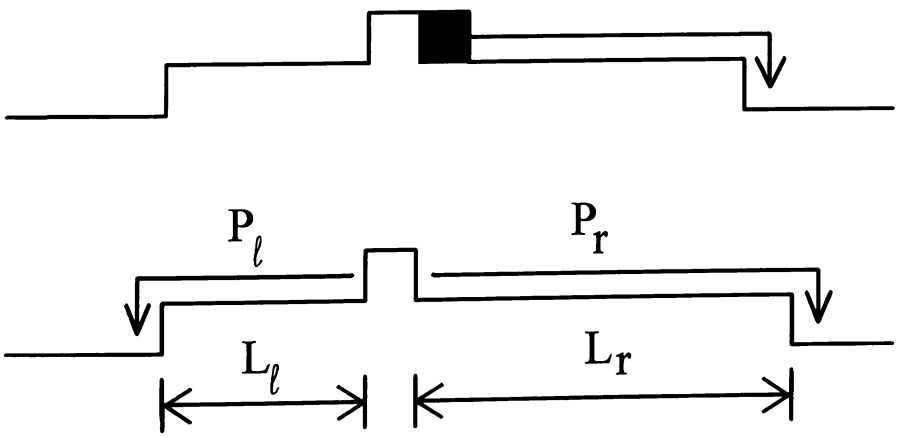

Figure 5.5 Creation and disappearance of an abandoned adatom on a top terrace.

Thus, all activated atom environments have been considered and the appropriate probabilities found. These probabilities, equations (5.9) to (5.15), govern the evolution of the entire system. For a given profile the only user-specified parameter in these probabilities is the step edge reflection coefficient k. The parameters O and U are only dependent upon k and are given by $O = 1/(2 - k)$ and $U = (1 - k)/(2 - k)$.

The profile does not always consist of widely spaced steps. Situations may arise, usually with the beginning profile, where narrow terraces exist. For example, the (11) face is a stepped surface with terraces of width one and steps of height one. These situations must be handled carefully. In these simulations the (10) face is stable since no embedded terrace atoms (those having two in-plane NN sites) are allowed to activate. The (11) face is taken to be stable as well in order to imitate the behavior of a triangular lattice. This also excludes formation of steps of height two which are energetically costly. Atoms diffuse over the (11) face just as they do over the (10) face. Thus, atoms lying entirely within the (11) face are not kink sites. These conditions result in this square lattice mimicking a triangular lattice. A schematic of the two equivalent lattices is shown in Figure 5.6. The two well sites have the same binding energy so that on average they will have equal occupation probabilities. Thus, with the (11) face stable, the probabilities of movement are not based on the distances to the nearest steps, but, rather to the nearest well site locations. That is, L_r and L_l are actually the distances from the activated site to the nearest well site.

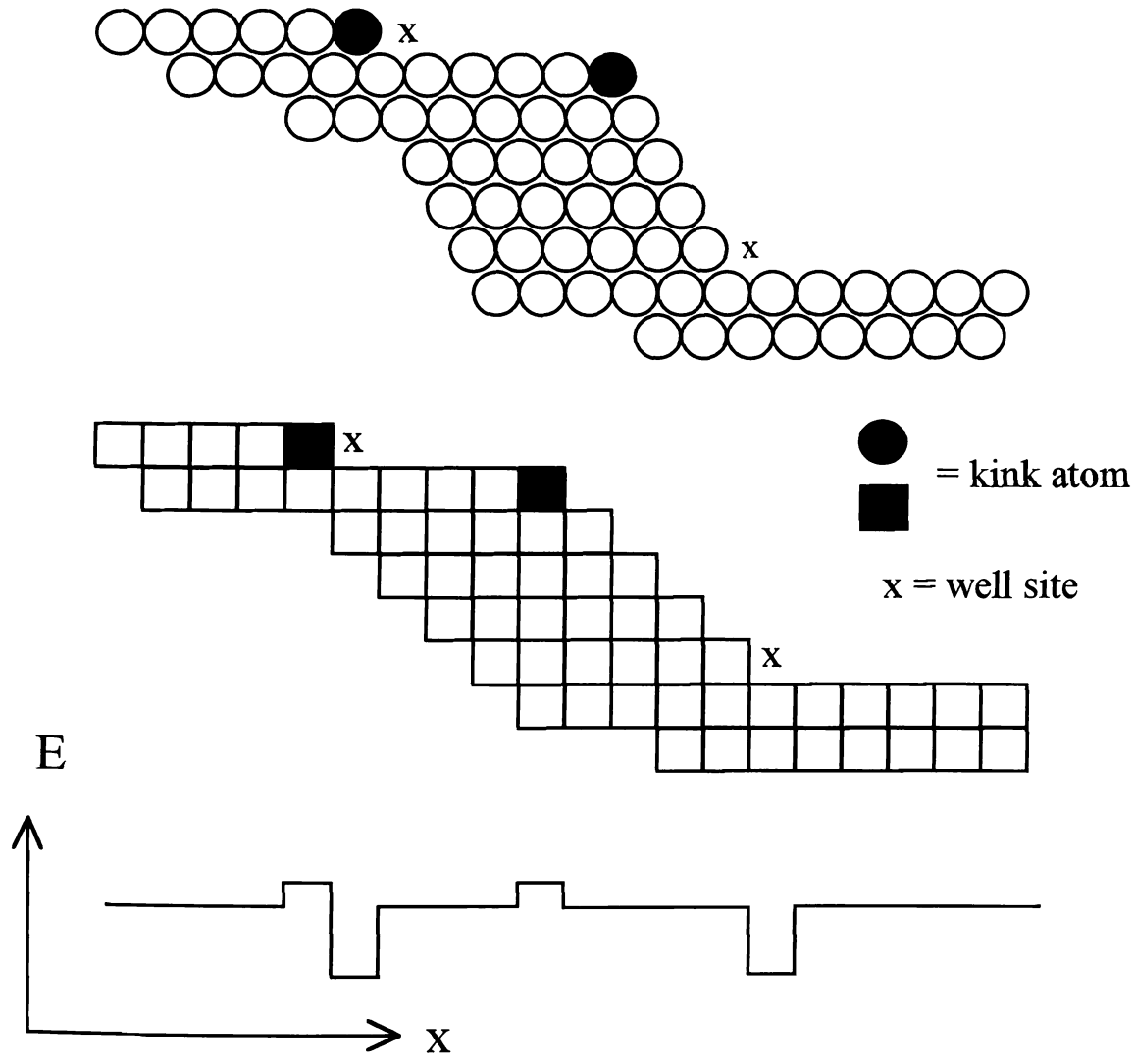

Figure 5.6 Equivalency of triangular and square lattices along with the respective adatom binding energy curves for each.

5.4 SIMULATION ALGORITHM

With the dynamical rules outlined above I now discuss the operational structure of the simulations. Briefly, an active kink site is chosen at random and given the opportunity to move. If the movement occurs the program updates the profile information and system time before another site is chosen. This continues until the profile's evolution is complete.

The program consists of two arrays containing all of the required information. The program begins by filling a profile array with the initial height vs. position information, $z(x, t = 0)$. In the environment array, all kink site and nearby well site positions are stored. This array has the following information for every kink site: the closest well site positions on each side of the kink atom and whether these well sites are up steps (absorbing barrier) or down steps (absorbing barrier after a step down). This is all the information needed to determine an atom's movement if chosen.

Once the initial information is determined, the system begins the evolution process. Using a very reliable random number generator [CHAW94], a kink site atom is chosen at random. The local environment of this site is found in the environment array and the probabilities for its available types of motion are calculated. A second random number, r, $0 < r < 1$, is generated to determine which trajectory the chosen atom follows. If $r < P_r$, path r is chosen, whereas if $r > 1 - P_l$ path l is taken. Otherwise the atom remains stationary (since paths 1 and 2 result in no movement). The chosen atom is then moved to its final position at $+L_r$ or $-L_l$. Two things happen prior to movement of the next atom. First, the position of the original kink position is deleted as a kink is no longer there and the final position is also removed as a well site since it is now occupied. Second, the environment array must be corrected to reflect the changes caused by the last movement. This includes updates for possible new kink and/or well sites near the initial and final positions. Regardless of movement, the simulation time is increased by τ = (number of kinks)$^{-1}$, which is the mean time between detachment events in the entire system in units

of the kink detachment time. After every movement a check occurs to see if the previous movement resulted in an abandoned atom being left on a terrace. If this is true, equation (5.15) is used to move this isolated atom and the arrays are updated as necessary. After these updates, and checking for abandoned adatoms, the system is ready to move another kink site. This cycle is repeated until the simulation is a) manually ended or b) the profile reaches a preset amplitude and stops automatically.

Periodically throughout the course of a run the profile is analyzed. The recorded information includes the average peak-to-peak amplitude and the Fourier transform coefficients of the average profile (both averaged over the m periods in each system), which were recorded at preset times along with the simulation time. The area difference between the profile and a flat surface as well as the system roughness are also recorded. In addition, the average profile is recorded at five different stages of the decay. These data provide the results presented in Section 5.6.

5.5 CONTINUUM MODEL AND PREVIOUS RESULTS

For systems above their roughening temperature a continuum approach may be used to solve the time dependence of the profile evolution. To promote matter transport a driving force must be present. For example, the driving force for heat conduction is a thermal gradient. In the case of surface diffusion the driving force is a gradient in the chemical potential or, equivalently, the surface curvature "seen" by a surface atom. By **J** we denote the surface current (number/cm$^2 \cdot$ s) of diffusing atoms. For an areal density (number/cm^2) n and an average drift velocity v we have the following relationship,

(5.16) $$\mathbf{J} = n\mathbf{v}.$$

Now, the drift velocity v can be related to the driving force **F** through

(5.17) $$\mathbf{v} = \mu_m \mathbf{F}$$

where μ_m is the particle mobility. The Nernst-Einstein relationship [FEYN63] relating the mobility to the diffusion constant and temperature is,

(5.18) $$D = \mu_m k_B T.$$

Thus,

(5.19) $$\mathbf{v} = (D / k_B T)\mathbf{F} = (D / k_B T)\nabla\mu$$

where μ is the position dependent chemical potential. As $\mathbf{v}$ refers to the average velocity of atoms over the surface, $\nabla\mu = d\mu/ds$ with s representing the coordinate along the surface. Since we are dealing with a closed system we must conserve matter. To do this, we begin with the continuity equation,

(5.20) $$\nabla \cdot \mathbf{J} + \frac{dn}{dt} = 0.$$

Applying equation (5.20) to equations (5.16) and (5.19) leads to

(5.21) $$\frac{Dn}{k_B T}\frac{d^2\mu}{ds^2} = -\frac{dn}{dt}.$$

It is possible to relate the chemical potential $\mu(x)$ to the surface curvature $K(x)$. The calculation [MULL63] uses a Lagrangian formalism to minimize the free energy for a given profile shape. Consider a two-dimensional curve, $z = z(x)$, its associated curvature $K(x)$, and surface energy $\gamma(\theta)$, where $\tan\theta = dz/dx$. The quantity minimized is $\int \gamma(s) \cdot ds$ where s is the coordinate along the surface. This energy is also expressed in terms of the integrated chemical potential per atom along the surface and the chemical potential $\mu = \mu(x)$ which minimizes this energy is calculated. The result is,

(5.22) $$\mu(x) = \Omega K(x)\left\{\gamma(\theta) + \frac{\partial^2\gamma(\theta)}{\partial\theta^2}\right\},$$

where Ω is the atomic volume. This result is just a special case of the result for the chemical potential of an ideal gas. For an ideal gas, the chemical potential is expressed using the Gibbs-Thomson result,

(5.23) $$\mu(x) = \mu_0 + \Omega K(x)\gamma(\theta),$$

where μ_0 is the constant chemical potential of a vapor above a flat (K(x) = 0) surface. Thus, for materials with isotropic $\gamma(\theta)$, such as liquids, the two expressions agree.

Since the profile height is the experimentally measured quantity we need to express the governing equations in terms of z(x) rather than $\mu(x)$. The curvature K(x) is, in terms of the function z(x),

$$K(x) = \frac{-z''}{(1+(z')^2)^{3/2}}. \tag{5.24}$$

where z' denotes the derivative of z with respect to x. Since the gradients of μ are with respect to the surface coordinate s we change variables from this coordinate to x by using the projection of a surface element onto the x-axis,

$$ds = dx\sqrt{1+(z')^2} \tag{5.25}$$

and the chain rule

$$\frac{d}{ds} = \left(\frac{dx}{ds}\right)\frac{d}{dx}. \tag{5.26}$$

Multiplying equation (5.21) by Ω and applying equations (5.24) to (5.26) we obtain the following differential equation describing the profile's evolution [BONZ84a]

$$\frac{\partial z}{\partial t} = \frac{nD\Omega}{k_B T}\frac{1}{\sqrt{1+(z')^2}}\left\{\frac{\partial^2 \mu}{\partial x^2} - \frac{z'z''}{(1+(z')^2)^{3/2}}\frac{\partial \mu}{\partial x}\right\}, \tag{5.27}$$

with $\mu(x)$ given by equation (5.22). This equation is, understandably, unsolvable in closed form for a reasonable choice of anisotropic $\gamma(\theta)$ let alone the simpler case of isotropic $\gamma(\theta)$. However, in the small slope approximation, $z' \ll 1$, and for the case of isotropic surface energy, $\gamma(\theta) = \gamma$, equation (5.27) simplifies to the following form,

$$\frac{\partial z}{\partial t} = \frac{nD\Omega^2\gamma}{k_B T}(-z'''') = -Bz''''. \tag{5.28}$$

The solution to this separable differential equation is a shape preserving exponential decay. For an initially sinusoidal profile, $z(x, t = 0) = A_0\sin(kx)$, z(x, t) is given by

$$z(x,t) = e^{-Bk^4 t}A_0\sin(kx) = z(x,0)e^{-Bk^4 t} \tag{5.29}$$

where $k = 2\pi/\lambda$ is the wavenumber and not the reflection coefficient. Thus, a plot of $\ln(A(t)/A_0)$ versus time t should result in a straight line of slope $-Bk^4$ so that the "decay time" scales as $\tau \sim \lambda^4$. Equation (5.28) can also be applied to other geometries by changing the boundary conditions. For example, this same exact method is used to derive the time dependent depth and width of a grain boundary groove under the action of surface diffusion and agrees with experimental observations.

Profile decay has received much more theoretical attention than experimental. The main reason for this discrepancy is that reliable surface diffusion measurements are very difficult to perform. Surface contamination and impurities are known to significantly effect surface diffusion rates and surface structure. Thus, stringent experimental conditions such as UHV and extensive sample cleaning are required. Experimental techniques such as *in situ* optical interference microscopy and laser light diffraction, as well as *ex situ* electron microscopy have been employed to observe profile relaxation. However, most of these experiments have been aimed at obtaining information on the static profile shape instead of quantitative information regarding the temporal dynamics. One instance where the decay time was observed to follow a λ^4 dependence was the laser light scattering experiment of Keefe *et al* [KEEF93]. Many of the theoretical treatments, but few experimental studies, have dealt with the case below T_R. As will be discussed below, the difficulties in properly treating the situation on a lattice are formidable and many problems remain.

Another important prediction of the continuum model is that the profiles are *shape preserving* as indicated by equation (5.29). That is, the initial profile shape should be completely preserved throughout the profile's evolution if only one wavelength is present. Profiles created on macroscopic surfaces both above and below their roughening temperatures have, indeed, exhibited shape preservation throughout the decay process. For example, Yamashita *et al* [YAMA81] studied gratings produced on the (110), (100), and (111) faces of a Ni crystal. The low density Ni(110) face has the largest surface

energy of these three and, thus, the lowest roughening temperature. Profiles prepared on the (110) face maintained their initially sinusoidal shape. In contrast, gratings prepared on the other two faces resulted in trapezoidal profiles with flattened tops and bottoms. The (100) and (111) macroscopic samples were studied below their respective roughening temperatures. The flattened tops and bottoms correspond to the macroscopic orientations which are also directions of lower surface energy. These same shapes were observed throughout the relaxation process.

The reason for the appearance of these flat portions is that different crystal faces possess different surface free energies. The low energy faces are represented by cusps in the Wulff plot. The Wulff plot [WULF01, HERR51, MULL63] is a polar plot of the surface free energy as a function of surface orientation. Certain orientations correspond to cusps in γ where the derivative $\partial\gamma(\theta)/\partial\theta$ becomes discontinuous. Since these orientations have a smaller contribution to the overall free energy of the sample, a crystal will preferentially form areas of these orientations which are as large as possible. These cusps, and hence, the facets, persist for temperatures up to the roughening temperature T_R of the face under consideration at which point facets of this orientation disappear. As T approaches T_R from below the facet size shrinks according to a Kosterlitz-Thouless type behavior [VANB87]. Above T_R the cusps in the surface free energy disappear in favor of blunted minima.

The presence of the cusps in the Wulff plot can be simply understood. Consider an atomically flat crystal surface (a facet) below the roughening temperature. This facet has a surface energy γ_0. In order to change the overall macroscopic orientation of this surface, a periodic spacing of steps must be created. The formation of such a vicinal surface requires an amount of energy proportional to the density and length of the steps. This energy is expressed in terms of an energy per unit length of the step edge. To produce a small orientation change (equivalent to a large step spacing) a non-zero amount of energy is required. This is the origin of the sharp cusp in the surface energy. The reason for the

disappearance of facets at T_R is due to the disappearance of the step free energy per unit length at T_R [WEEK80]. This means that steps of all lengths can be thermally excited with no affect on the system's surface free energy.

Below the roughening temperature the details of profile decay are not well understood. The discontinuity in $\partial\gamma(\theta)/\partial\theta$ leads to a singularity in $\partial^2\gamma(\theta)/\partial\theta^2$. This singularity makes equation (5.27) unsolvable. Bonzel *et al* shed much light on the profile shape below the roughening temperature in a series of papers [BONZ84a, 84b, PREU86]. Their approach was to handle the divergent $\partial^2\gamma(\theta)/\partial\theta^2$ singularity through a mathematical approximation. While they were able to explain the experimentally observed trapezoidal shapes they were unable to explain the observed relaxation dependence on wavelength. However, the observed relaxation of a faceted, trapezoidal, profile was found to be non-exponential and shape preserving.

This decay time dependence on λ^4 can be simply understood by recalling some of the results presented in Section 3.5 regarding the coalescence time for two spheres of radius R. The coalescence time τ_{coal} was proportional to R^4 so it is not surprising that here the time scale behaves as the fourth power of the typical length scale λ of the problem. The argument outlined above showed that theoretically the amplitude decays exponentially with a characteristic time $\tau \sim \lambda^4$ in the high temperature regime.

5.6 SIMULATION RESULTS

The time equal zero profile is a sinusoid: $z(x, t = 0) = CINT[A_0\sin(2\pi x/\lambda)]$ where A_0 is the initial amplitude and λ is the wavelength. The total system size is T and $0 \le x \le T-1$. The CINT(y) function takes the value y and rounds it off to the nearest integer value. For example, $CINT(-2.4) = -2$. Thus, the system consists of $m = T/\lambda$ periods. The initial amplitude A_0 is chosen so that no face steeper than the (11) face is present. This corresponds to a maximum slope of one. For a given wavelength λ the

maximum allowable amplitude consistent with this condition is $2\pi A_{max}/\lambda = 1$ so that $A_{max} = \lambda/2\pi$. The only other parameter specified is the step edge reflection coefficient k. This coefficient k is related to the temperature by $\Delta/(k_BT) = -\ln(1 - k)$, which comes from the relation $1 - k = e^{-\beta\Delta}$. Usually, the total system size T was 8192. The ratio of A_0/A_{max} studied was typically 1/4 to 1 for the wavelength range $32 \leq \lambda \leq 256$. This range of A_0/A_{max} was chosen to avoid initial profiles with amplitudes of one or two. For $\lambda = 256$ this range included $A_0/A_{max} \gtrsim 1/16$. Wavelengths larger than 256 were not used due to the intolerably long computation times required. With such a large system size our data is averaged over many periods. The reflection coefficient k used was generally 0.9 which corresponds to $k_BT = 0.434\Delta$. In the remainder of this section I will discuss the influences of A_0, λ, and k upon the system decay. I will also attempt to discuss some of these results and how they relate to other studies by various authors.

The most useful of the data is the peak-to-peak amplitude versus time. This amplitude will be denoted by $2A = 2A(t)$. The parameters A_0, λ, and k are all independent. This section will cover much of the available parameter space of these three variables. However, the main results presented cover the amplitude evolution as a function of time while varying λ and k.

One striking result of these simulations is shown by the data in Figure 5.7. This figure is a plot of the peak-to-peak amplitude vs. time/$\lambda^{3.5}$ for three different wavelengths λ and three different starting values of $A_0/A_{max} = 2\pi A_0/\lambda$ for k = 0.9. It is apparent from this figure that, at fixed ratio of initial amplitude to wavelength, all the curves collapse onto one "universal" curve as time/$(\lambda^{3.5\pm0.1})$. Figure 5.8 is the same data plotted vs. time/λ^4 which is the scaling prediction [MULL59] for the $T > T_{roughening}$ regime described in Section 5.5.

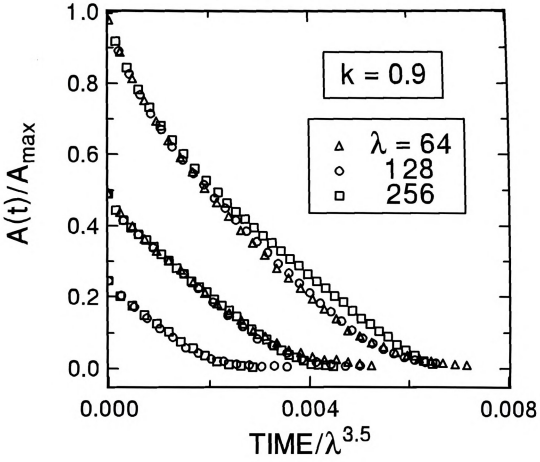

Figure 5.7 Amplitude decay, $A(t)/A_{max}$, vs. Time/$\lambda^{3.5}$ for step edge reflection coefficient $k = 0.9$ and wavelengths $\lambda = 64$, 128, and 256.

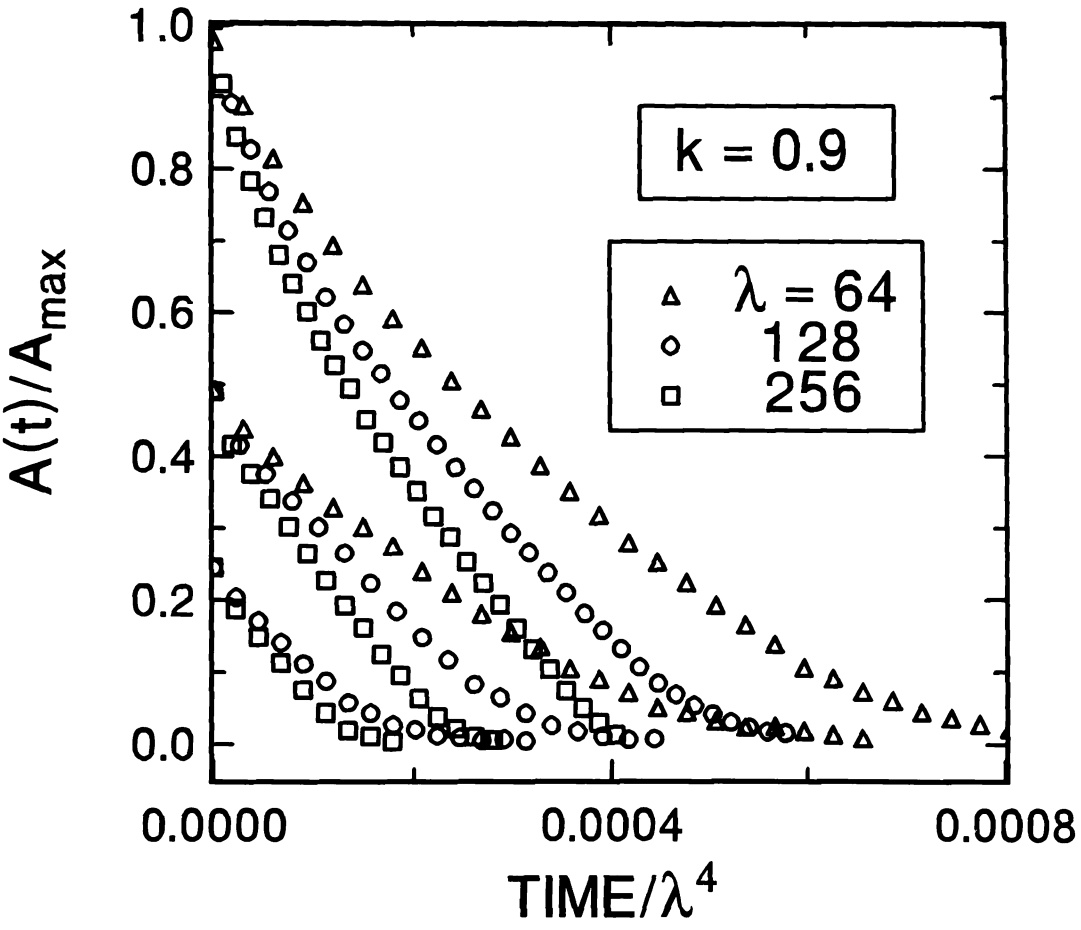

Figure 5.8 Amplitude decay, $A(t)/A_{max}$, vs. Time/$\lambda^{4.0}$ for step edge reflection coefficient k = 0.9 and wavelengths λ = 64, 128, and 256.

Figures 5.7, 5.9, and 5.10 show that our simulations exhibit a non-exponential decay of a trapezoidal shape which shows shape preservation as well. Figure 5.9 shows the time evolution of a sample profile. The shape preservation is exhibited in Figure 5.10. This plot shows curves 2 through 5 of Figure 5.9 scaled to have the same area. Since all five traces lie nearly atop one another, the trapezoidal shape is preserved throughout the decay process. The tops and bottoms of the profiles are flat to about one lattice constant over a width of roughly 20 lattice constants. As can be seen in Figure 5.9, the flat regions are smoothly joined to the sloped hillsides by rounded regions. The shapes near the edge of a flattened extrema follow a power law $z(\delta x) \sim (\delta x)^{\alpha}$ with $\alpha \approx 1.6$ over a distance of roughly 10 to 15 lattice constants. Experimental observations [HEYR87, METO89] indicate that faceted regions on equilibrium shaped metallic crystals meet at sharp corners only for temperatures near the roughening temperature of the facet. Below T_R the profile shape near the facet edge is found experimentally to behave as $z(\delta x) \sim (\delta x)^{\alpha}$ with $\alpha \approx 1.6$ [ROTT84, METO87] in agreement with our observed morphology. This prediction of $\alpha \approx 1.6$ may be derived from a surface energy function containing step-step interactions (the G_3 term mentioned below). Our simulations lack long-ranged interactions between steps and it is, thus, probably coincidental that near the edge of the flattened tops of our trapezoidal profiles we observe rounded regions which follow the $\alpha \approx 1.6$ prediction.

An important difference between our simulations and others [RETT88, OZDE90] is how step-step interactions are treated. Prior efforts include such interactions directly in the chemical potential and surface free energy expressions. These repulsive interactions provide a continuous driving force for profile decay. This can be seen by looking at the expression for the free energy per unit area projected on the x-y plane for the case of a (2+1)D system where $z = z(x, y)$. Let $\gamma(z')$ denote the free energy per unit area normal to the profile and $G(z')$ denote the projection of $\gamma(z')$ onto the x-y plane. Thus, $\gamma(z')$ is,

$$\gamma(z') = \frac{G(z')}{\sqrt{1+(z')^2}}. \tag{5.30}$$

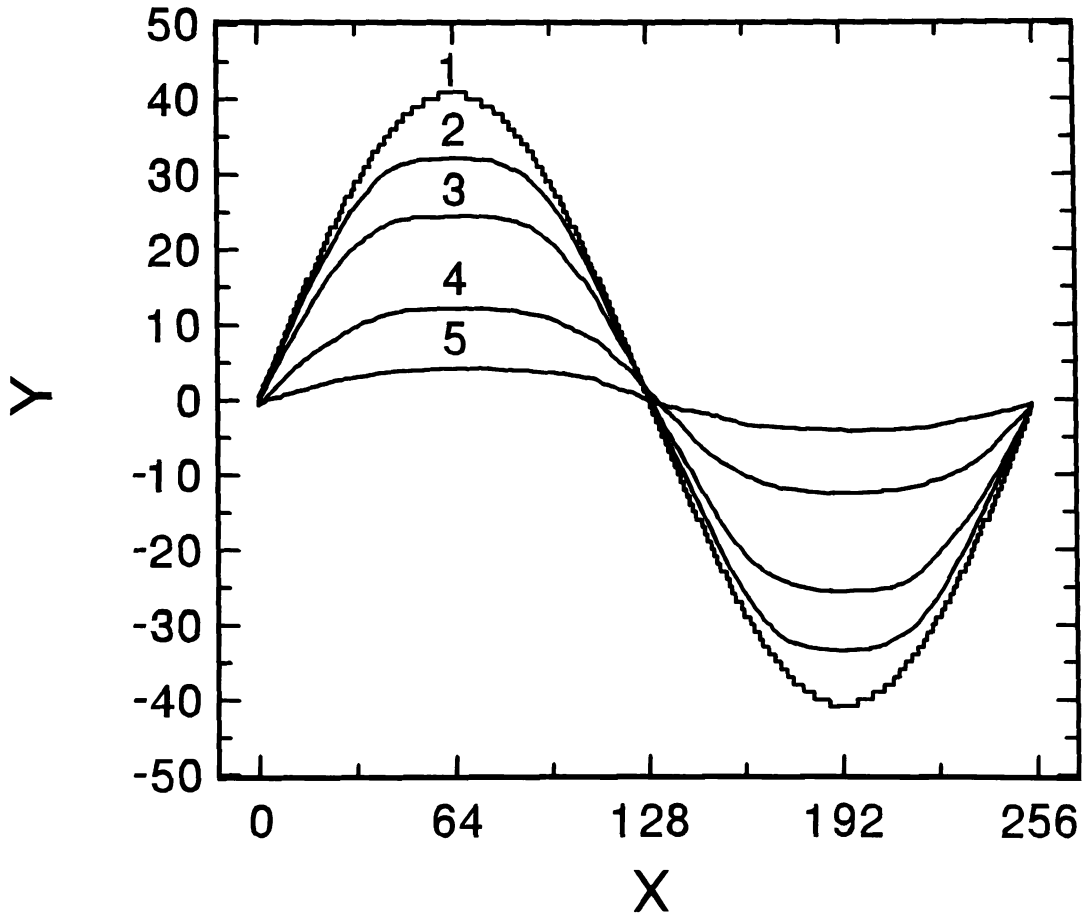

Figure 5.9 Time evolution of a system with $\lambda = 256$, $A_0 = 40.7$, and $k = 0.9$ shown at various stages of evolution. Each profile is the average of a system containing 32 periods. Beginning with curve one the simulation times of the different average profiles are 0, 1.35×10^5, 3.82×10^5, 9.80×10^5, and 1.45×10^6.

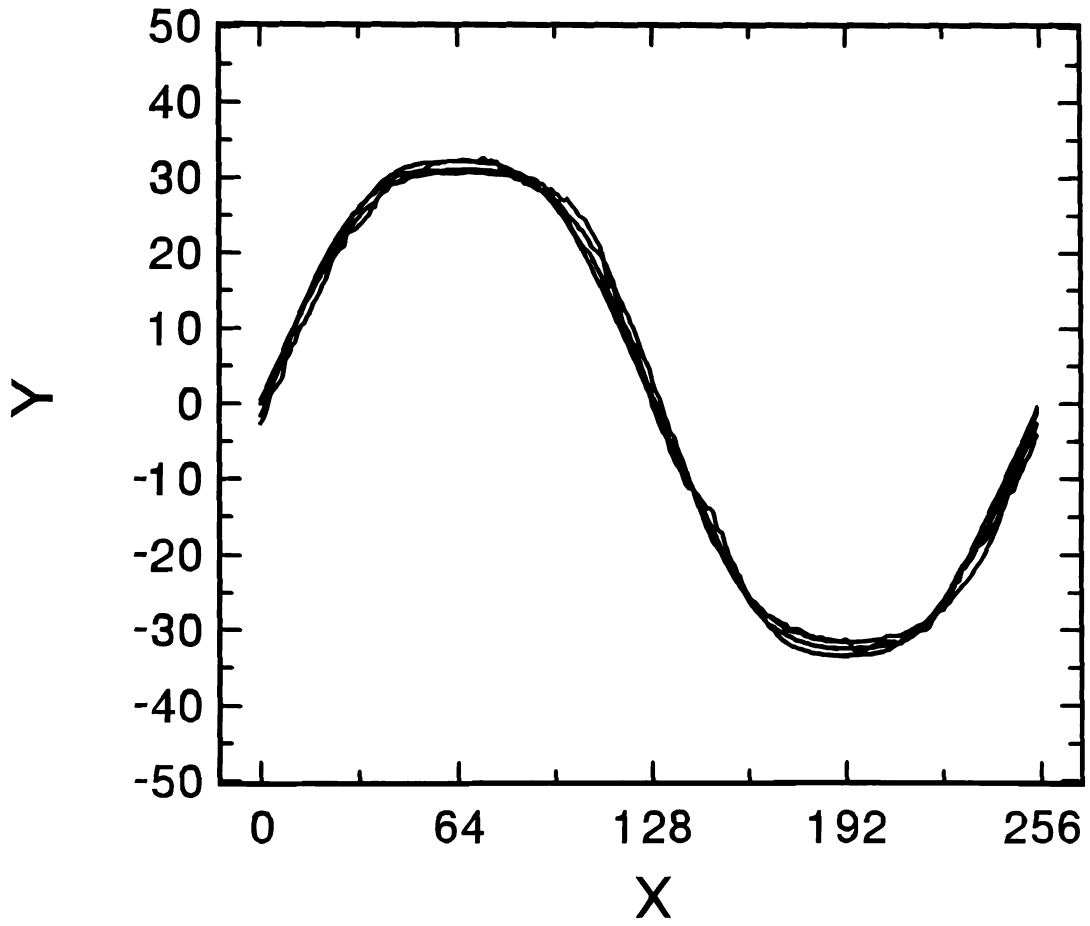

Figure 5.10 Curves two through five of Figure 5.9 normalized to have the same area as curve two in Figure 5.9. The self-similarity of the curves indicates the shape preservation quality of the profiles.

Below T_R, G(z') takes the Gruber-Mullins-Pokrovski-Talapov form [GRUB67, RETT88],

$$G(z') = G_0 + g|z'| + \frac{1}{3}G_3|z'|^3 + \ldots. \tag{5.31}$$

Here, G_0 is the free energy of the macroscopic (flat) surface. In the second term, g is the step energy per unit length and |z'| is the step density on the surface. The $|z'|^3$ term is the step-step interaction term. This term may be due to direct energetic interactions such as strain or dipole-dipole type interactions or in a (2+1)D system it also arises from *entropic repulsion* between steps. Consider the case of three steps of the same sign which are free to move about, but unable to cross, and free of direct energetic interactions. The center step has a higher entropy when the outer steps are far apart. This arises from the ability of the center step to wander, thus having a larger configurational entropy. With the y-direction into the page in Figure 5.2 this simply means that the step position x may vary with position y along the step edge. When the two outer steps are close, this available wandering of the center step is decreased. Since the free energy has the entropy in the form $-TS$, a larger entropy is energetically favorable. Thus, the outer two steps are effectively repelled. All previous simulations of profile decay have included this repulsive term which serves to drive the system to widely spaced steps, i.e. a flat surface. Experimental studies of terrace width distributions yield results which are consistent with the existence of repulsive interactions amongst steps with a $|z'|^3$ dependence [WILL91].

In the present simulations long-ranged interactions between steps are absent. However, there is a contact interaction between adjacent steps (for step separations of one lattice constant) since double height steps and overhangs are not allowed. Thus, two steps are unable to cross.

Consider two completely independent random walkers on a line which may pass through one another. The absolute value of their average separation (averaged over all possible paths) will increase as $(\text{time})^{1/2}$. Now, if these two walkers are restricted so that they cannot pass through one another (they simply bounce off one another like billiard

balls) then the average separation still increases as $(\text{time})^{1/2}$. This behavior is the same since the process of passing through one another and reflecting off each other are identical except for an exchange of identity labels.

Two adjacent steps which cannot pass through one another behave in a manner similar, but not identical, to random walkers. Simulations of the separation of two isolated steps (with $k = 0$) using the present algorithm yield an average terrace width between the two steps which grows as $(\text{time})^{1/3}$. This weaker time dependence results from the fact that often, when a kink site activates it returns to its original site after a random walk, and the step does not move. Only when the activated walker makes it to an adjacent step without returning home does the step move. This step movement becomes less frequent as the steps separate. The cause of the separation increase is that the separation is prohibited from being less than one lattice constant. This skews the likelihood of the steps to have a larger average separation. Occasionally, two steps collide and have no option but to increase their separation from one to two lattice constants. This effect is, however, small. So, while there is an entropic repulsion present in our simulations, it is a weak driving force for the profile decay. A long time is needed for adjacent steps to explore phase space and discover the effects of reflecting away from neighboring steps. Additionally, this step-step repulsion is only present on the sloping hillsides of the corrugated profile. Steps of unlike sign on the top terraces and bottom valleys do not have any repulsion since when two steps attempt to cross in these situations, they simply annihilate. This annihilation is irreversible. Once a terrace or valley disappears, it cannot re-form. Thus, although this small repulsive effect pushes the top terraces and bottom valleys to be eliminated, it is the lack of island nucleation which makes it permanent. We have been unable to relate the $(\text{time})^{1/3}$ spreading to the $\tau \sim \lambda^{3.5}$ decay time scaling.

As the exchange of atoms between any two terraces is random, we should expect the top terrace to decay in a random fashion. For a top terrace of width W, $\sim W^2$

exchanges should be needed before the top terrace disappears. This same behavior is true for the bottom terrace (which is filling in rather than decaying). This type of behavior is observed in our simulations. Since the simulations take place at low temperature island nucleation is forbidden. Once a terrace disappears, or fills in for the case of a layer at the bottom of the profile, it cannot reappear. With no energetic interactions, the system energy is determined entirely by the number of steps. The disappearance of a terrace reduces the number of steps by two. Thus, the energy decreases in a discontinuous manner until the zero energy, flat, state is reached.

As already noted a true continuum approach cannot be used below the roughening temperature due to the singularities in $\gamma(\theta)$. Instead, the problem must be treated on a lattice. This causes great difficulty in applying ideas such as derivatives and curvature. It is for this reason we were unable to formulate an analytical treatment describing the dynamics of our model. Such a treatment could help immensely in understanding the temporal behavior and the profile shape dependencies upon various parameters. Since no "energy based" concepts were used in these simulations this may be impossible. Thus, the rest of this section will discuss the remaining main results of these simulations and how they relate to some of the other analytical and numerical results of other investigators. No attempt at a full mathematical discussion such as those of [RETT88, OZDE90] will be made.

First I will discuss the scaling of the decay time with wavelength. Figure 5.7 shows that the amplitude decay scales as $\tau \sim \lambda^{3.5}$ in a non-exponential way. As noted earlier, Bonzel *et al* [BONZ84a, 84b, PREU86] attempted to solve the profile decay problem below the roughening temperature using a continuum approach. Their results consisted of a numerical solution of the following differential equation,

$$\frac{\partial z}{\partial t} = -\left(\frac{2n\Omega^2 D G_3}{k_B T}\right)\frac{\partial^2(|z'|z'')}{\partial x^2}. \tag{5.32}$$

Though not explicitly stated in the paper, the data in Figure 7 of [PREU86] yield a decay time which behaves as roughly $\lambda^{3.7}$. Additionally, their numerical solutions exhibited trapezoidal shapes similar to those shown in Figure 5.9.

Ozdemir and Zangwill [OZDE90] attempted to solve equation (5.32) numerically for the case of unidirectional grooves, $z(x, y, t = 0) = A_0\sin(2\pi x/\lambda)$. Using separation of variables, $z(x, y, t) = u(x)w(t)$, the temporal and spatial variations of $z(x, t)$ are solutions of the following equations

$$\frac{dw}{dt} = -\xi w^2, \tag{5.33}$$

and

$$\left(\frac{2n\Omega^2 DG_3}{k_B T}\right)\frac{d^2(|u'(x)|u''(x))}{dx^2} = \xi u(x). \tag{5.34}$$

The separation constant ξ parametrizes a family of solutions. Integration of the first of these equations yields,

$$z(x,t) = \frac{u(x)}{(1+\xi t)}. \tag{5.35}$$

Thus, the profile should decay with time as t^{-1} for $\xi t \gg 1$. Our simulations instead exhibit the temporal behavior shown in Figure 5.11 which is a plot of $A(t)/A_{max}$ vs. time for the case of $A_0/A_{max} = 0.25$, $k = 0.9$, and $\lambda = 256$. For the majority of the decay the amplitude behaves nearly as $(-\text{time})$ as shown by the straight line which has been offset from the data, although there is a slight curvature. The deviations of the data and a straight line are generally $\lesssim 0.01$. This behavior is also seen for other values of A_0/A_{max} and λ. Careful inspection of Figure 5.7 shows that this behavior occurs over the majority of the decay cycle for nearly all chosen values of λ and A_0/A_{max}, especially for smaller A_0/λ values.

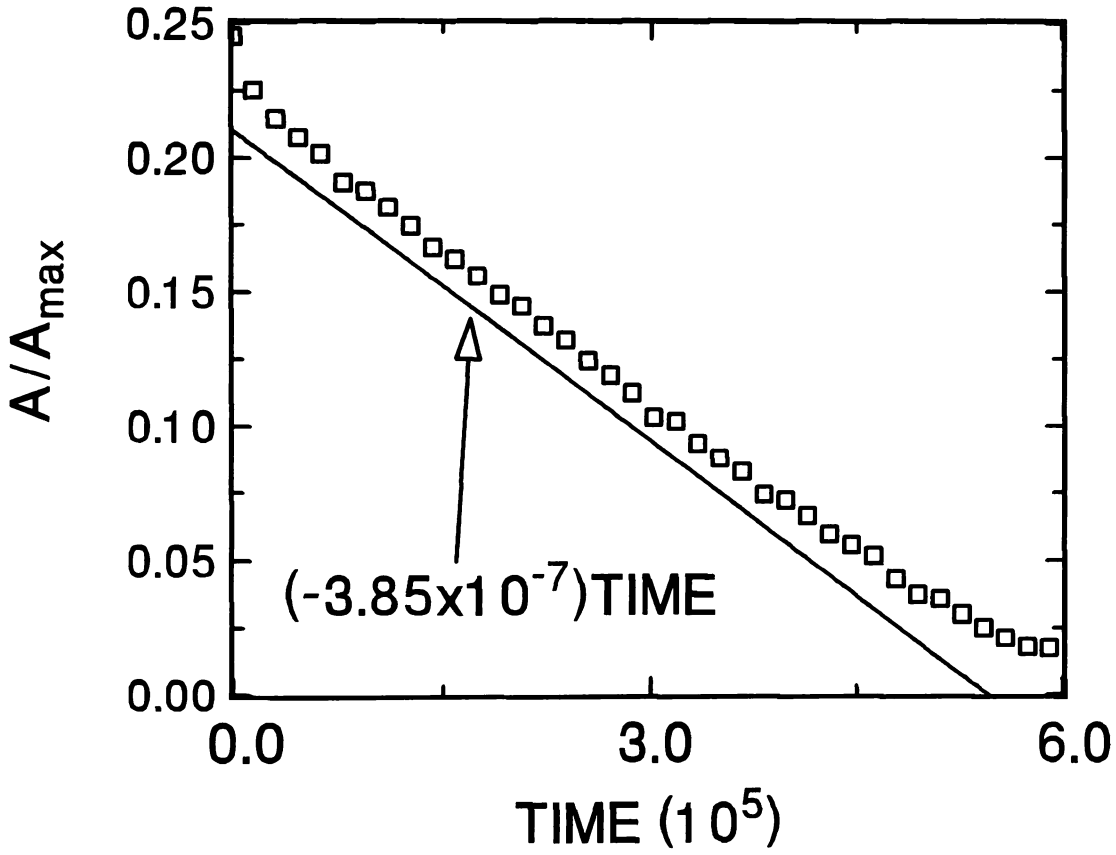

Figure 5.11 Amplitude decay, $A(t)/A_{max}$, vs. simulation time for a system with $\lambda = 256$, $A_0 = 10.2$, and $k = 0.9$ showing a decay which behaves nearly linearly with time. The solid line has a slope of -3.85×10^{-7}.

In addition to holding the ratio of initial amplitude to wavelength (A_0/λ) constant we have studied the behavior at constant initial amplitude A_0 and constant reflection coefficient value while varying the wavelength. The temporal evolution of this sequence should be different for two reasons. By holding the amplitude constant and varying λ the system is forced to change 1) the average terrace width and 2) the initial number of kink sites. At constant A_0/λ the average terrace width and number of initial kink sites is fairly constant for different λ's since the ratio A_0/λ determines the slope of the system. The scaling behavior of the amplitude decay at constant A_0 turns out to be significantly different than at constant A_0/λ. As shown in Figure 5.12 the data at different λ collapse to a single curve when scaled as time/$\lambda^{2.75\pm0.1}$. The two curves shown correspond to two different values of A_0. Each wavelength corresponds to averaging over a different number of periods since the total system size was always held constant at 8192. However, the standard deviations of A/A_0 were generally $\lesssim 0.01$ which is smaller than the symbol sizes used in Figure 5.12.

We can also look at the profile decay at constant A_0/A_{max} and λ while varying k. The major difference which results from varying k is the time taken to reach a given stage of evolution. It turns out that simply multiplying the time values by differing amounts leads to the A/A_0 curves falling very nearly atop one another when plotted versus time. This behavior is shown in Figure 5.13 which is a graph of A/A_0 vs. time with $\lambda = 128$, a constant $A_0 = 10.2$, and $k \in \{0, 0.7, 0.9, 0.997\}$. In making this graph, the time values of the lower k value plots have been scaled so the curves all nearly coincide with the $k = 0.997$ curve. The multiplication factors used were; 26.6 for $k = 0$, 30.0 for $k = 0.70$, 18.5 for $k = 0.90$, and 1.0 for $k = 0.997$. Thus, the runs using larger values of k required a much longer simulation time to complete. These runs also took significantly longer in total CPU time to complete as well.

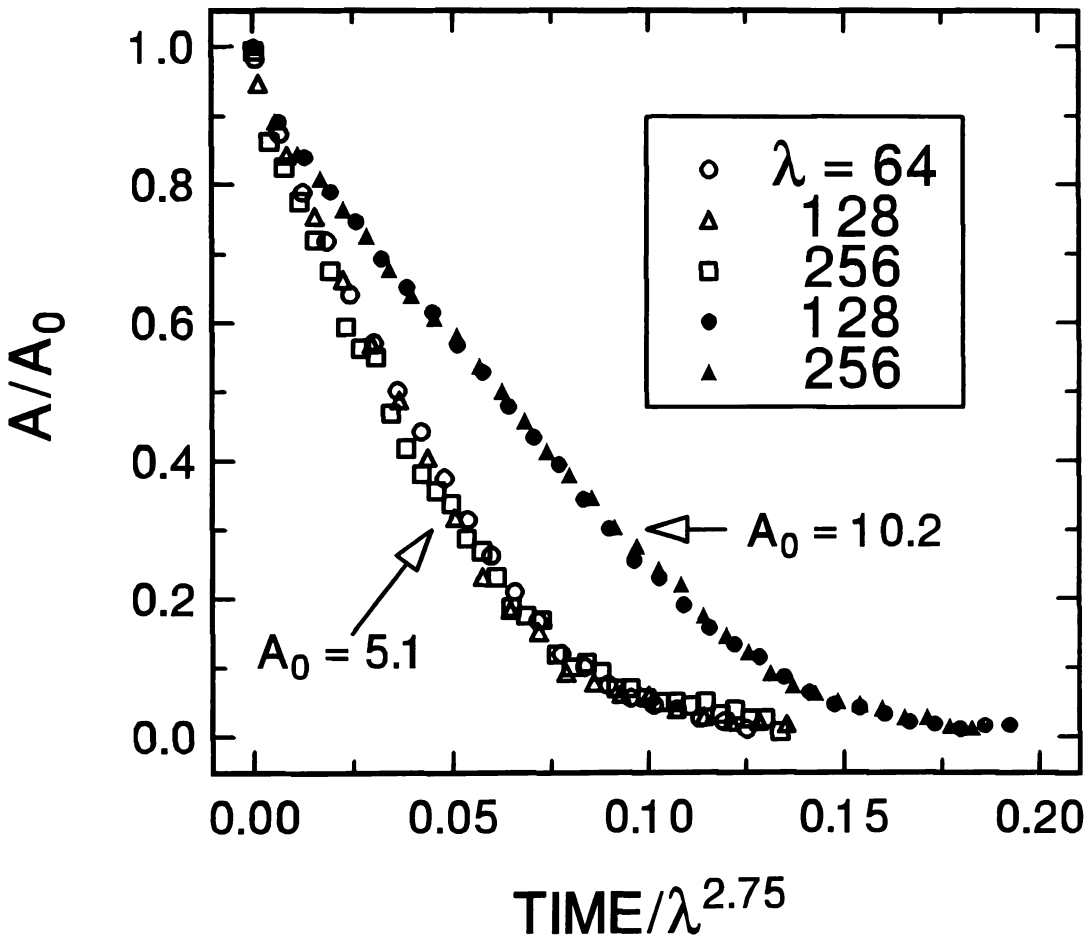

Figure 5.12 Amplitude fraction A/A_0 vs. Time/$\lambda^{2.75}$ for A_0 = 5.1 and 10.2 at various wavelengths λ.

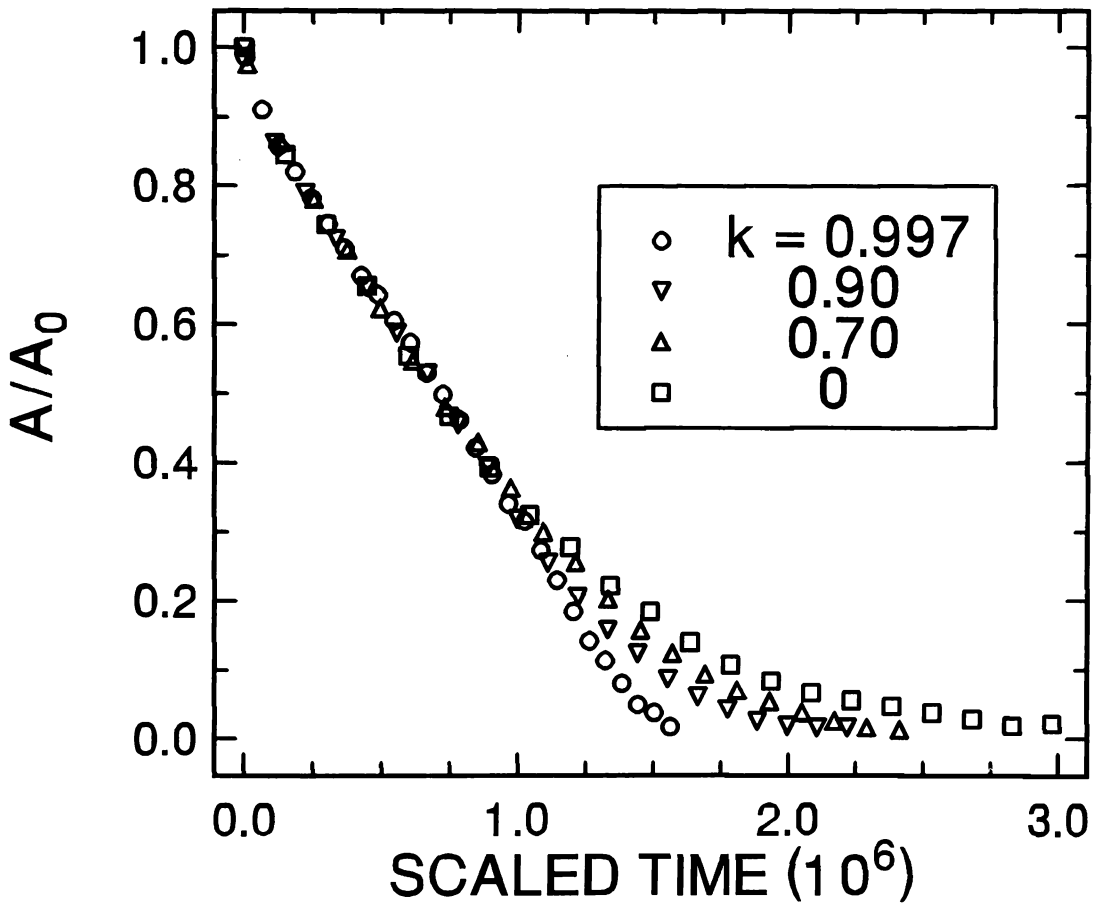

Figure 5.13 Amplitude fraction A/A_0 vs. scaled time at fixed $A_0/A_{max} = 1/2$ for $k \in \{0, 0.70, 0.90, 0.997\}$. The original time values were multiplied by 26.6, 30.0, 18.5, and 1.0 for the low to high values of k, respectively.

This behavior as well as other properties to be discussed can be qualitatively understood through an analysis of equations (5.9) through (5.12) which express the movement probabilities P_1, P_2, P_r, and P_l. In doing this I will assume the terrace widths L_r and L_l to be equal. While this is definitely not true during the decay it will allow us to gain some insight into the decay behavior. For this case $L_r = L_l$ and $P_r = P_l$, for all values of k. Since these are the only two movements which advance the system's decay, it is sufficient to investigate their behavior and not be concerned with P_1 and P_2 for the time being.

Figure 5.14 is a plot of P_r vs. terrace width L for different values of the reflection coefficient. One major feature of this plot is the k-dependence of P_r. For example, the $k = 0.99$ curve is very nearly independent of the terrace width L. This case is what I will call reflection coefficient limited. The L independence means that even for small terraces an atom is unlikely to strike the Schwoebel barrier $\sim$ 100 times (since $1 - k \sim 1/100$) without returning to its origin. The very small value of P_r ($\lesssim 1\%$) means that many more attempts are required for an atom to move away from its original position. This increase in number of attempts required explains why the $k = 0.997$ curve takes nearly 30 times longer to decay than the lower k runs in Figure 5.13. More generally we can understand the need for excessive times needed to complete these simulations. Many of the runs required anywhere from an hour up to 22 days of CPU time on a 486 class personal computer. This is because the total probability to move (path r or *l*) is, from Figure 5.14, in the range of 2 to 30%. Thus, the total probability to not move is generally $\gtrsim 70\%$. The majority of the time in the simulations is taken in giving various activated sites the *opportunity* to move without actually resulting in a movement. This is why sometimes 10^6 or more inquiries are needed to ultimately move $\sim 10^4$ atoms. An improvement in this respect could be provided by using a more efficient scheme for moving atoms [CHAS91]. In this algorithm, every movement is one which results in a movement away from the original site. However, the time increment is not just 1/N, but, rather, a properly weighted time. This weighted time accounts for the average time necessary for various movements

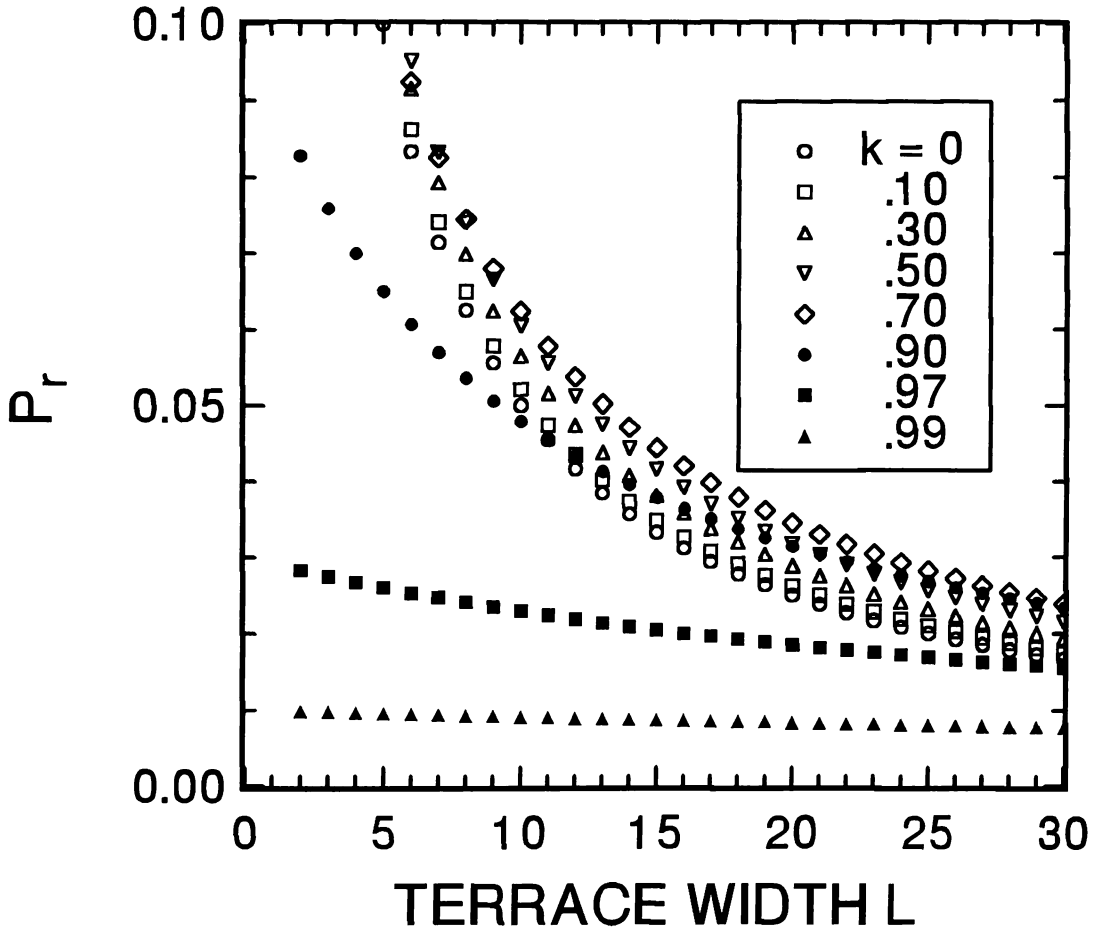

Figure 5.14 Movement probability P_r vs. terrace width L for various values of k.

to be successful. This scheme has been employed in the (2+1)D extension of this work [DUBS94b]. These three-dimensional simulations are still forced to track the entire random walk of the activated atom, however. If this system is run on a sinusoidal profile of width one (making it identical to our (1+1)D system), the amplitude decay is found to decay as time/$\lambda^{3.5}$ in agreement with Figure 5.7. While this three-dimensional system is also somewhat idealized, the agreement between the two methods is reassuring considering the significantly different algorithms used.

Another feature of Figure 5.14 results in the data shown in Figure 5.15. This latter figure shows the decay time as a function of $1 - k$ at constant $\lambda = 128$ and $A_0 = 10.2$. The decay time is defined as the simulation time when A/A_0 has fallen to one quarter of its initial value. For a system of wavelength λ and amplitude A we can define an average terrace width $L_{avg} = \lambda/4A$ since there are 4A terraces in a length λ. At $A/A_0 = 1/4$, this yields $L_{avg} \approx 13$. In Figure 5.14, with $L = 13$, P_r has a maximum for the case $k = 0.7$. Figure 5.15 indicates that the minimum decay time occurs for $k \approx 0.7$. These two results are in agreement. The higher value of P_r means a slightly higher probability for an atom to move than for $k = 0$, for example. Moving down the values of $P_r(L = 13)$ in Figure 5.14 we see that the highest P_r ($k = 0.7$) corresponds to the lowest decay time in Figure 5.15. On the other hand, higher k values lead to smaller P_r and longer decay times. A smaller value of P_r leads to more atoms being interrogated (i.e. given a chance to move) before a fluctuation occurs which is large enough for a terrace to decay or fill in, thus moving the decay process further along. Not too surprisingly, the ratio between P_r at two different k values from Figure 5.15 is, to within about 10%, the same as the inverse ratio of the two decay times from Figure 5.14 for the same two k values. As mentioned earlier, the higher values of k correspond to the case of reflection coefficient limited motion. The three curves in Figure 5.14 for $k \geq 0.9$ are nearly independent of L, especially above $L = 10$. Thus, we might expect the decay time to depend upon the transmission coefficient $1 - k$ for these values of k. The three high k points in Figure 5.15 follow a $\tau_{decay} \sim (1 - k)^{-a}$

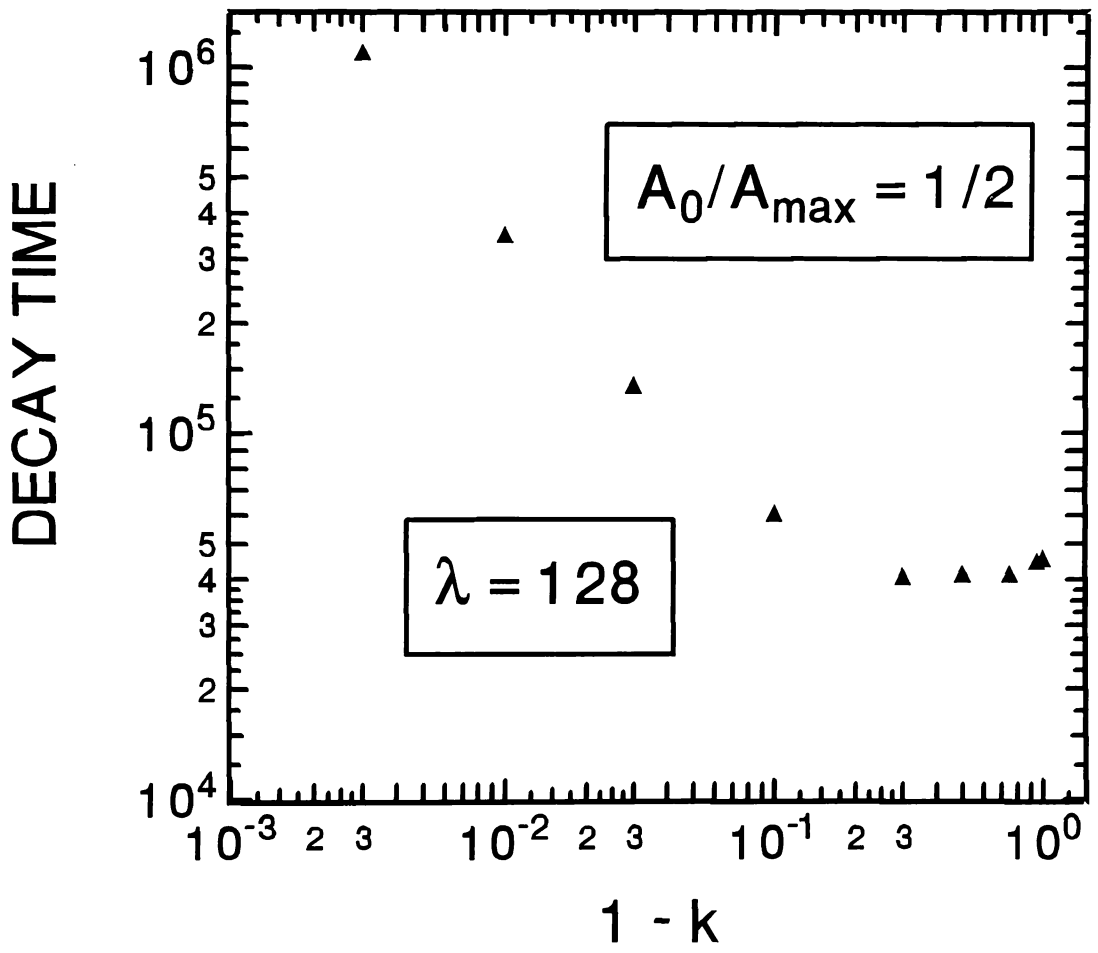

Figure 5.15 Decay time plotted vs. $1 - k$ for $A_0/A_{max} = 1/2$ and $\lambda = 128$. The decay time is defined as the time at which $A/A_0 = 1/4$.

behavior with a $\approx$ 0.9. This non-linear behavior differs from the linear behavior, a = 1, one might expect if the decay were not random in nature. The slight upturn of the decay time when k approaches one is also explained by Figure 5.14. Comparing the curves for k = 0 and k = 0.1 we see that P_r (and thus the total probability to move away from the original site) increases as k becomes non-zero. This increase in movement likelihood results in a decrease in the decay time. As is evident from Figure 5.15 this effect is small, but noticeable.

5.7 PARALLEL RESISTOR MODEL FOR P_1, P_2, P_r, AND P_ℓ

While writing this thesis a method even simpler in nature than the rate equation approach was discovered. It can be shown [DOYL84] that a random walker trapped between two absorbing barriers, possibly with repulsive barriers in between, is identical to an electrical circuit problem consisting of a battery and a set of appropriately chosen resistors. The principal idea of this method is to place a resistor (with a resistance which is dependent upon the site's neighbors) between adjacent surface sites and determine the amount of current flowing in the appropriate directions. This current is generated by a battery connected to the site of the activated kink atom. The nearest well sites on either side of the activated kink atom are connected to ground. The amount of current flowing in a particular direction is directly related to the probability of a random walker to move in that direction. Terrace sites with two in-plane NN atoms (such as x = 2 and x = 3 in Figure 5.3) are connected by a unit resistance. The connection between the top side of a step and the well site on the terrace below (x = L − 1 and x = L in Figure 5.3) is given a resistance of $(1 - k)^{-1}$, where k is still the step edge reflection coefficient. The reason for this choice of resistance values is related to the movement probability between adjacent sites. On an open terrace with two equivalent neighboring sites a walker is equally likely to move right or move left. Movement down a step occurs with a transmission probability

of $1 - k$. As will be explained below, the resistance is reciprocal in nature to the movement probability, thus the $(1 - k)^{-1}$ value of a step edge resistor.

When the kink site atom in Figure 5.1 activates it first moves to a position one lattice constant away from its starting site. These positions are shown in Figure 5.3 as $x = 1$ for activation out onto the lower terrace or what would be labeled as position $x = -1$ if the atom activates onto the upper terrace. With the site-to-site resistance values designated as above, we imagine the following scenario. At position $x = 1$ or $x = -1$ (depending upon which direction was chosen for activation) we connect a battery at some voltage V_0. The adjacent well sites are connected to ground. The movement probabilities we seek are precisely determined by the ratio of the currents which flow through either path to ground. However, this method can't take care of the activation probabilities O and U. Given that the atom activates, for example, onto the lower terrace this method determines the probabilities of return to $x = 0$ or to move to the adjacent terrace.

As a simple illustration of this method consider the situation of paths 1 and r involving activation onto the lower terrace. The adjacent site pairs (0,1), (1,2), (2,3) ..., $(L - 2, L - 1)$ are all connected by unit resistors. The $(L - 1, L)$ pair has a resistance of $(1 - k)^{-1}$. The resistance between $x = 1$ and $x = 0$ is, thus, $R_- = 1$ and that between $x = 1$ and $x = L$ is $R_+ = (L - 2) + (1 - k)^{-1}$. Defining $P_1 = O(p_1)$ and $P_r = O(p_r)$ the ratio p_1/p_r is given by R_+/R_-. This is because the probabilities p_1 and p_r are just the currents I_1 and I_r, respectively, which will flow in the plus or minus directions. Since the voltage drop between $x = 1$ and $x = 0$ is the same as that between $x = 1$ and $x = L$, the reciprocal relation exists. Ohm's law leads to $I_1R_- = I_rR_+$ which is precisely the same relationship. Thus, the probabilities p_1 and p_r are related by the following equation

$$\frac{p_r}{p_1} = L - 2 + \frac{1}{1-k} = L - 1 + \frac{k}{1-k}. \tag{5.36}$$

Combining this result with $p_l + p_r = 1$ and multiplying by the activation factor O we find the same results for p_r and p_l as those in equations (5.9) and (5.10). This method may also be used for all other environments discussed in Section 5.3. This method, however, is much simpler and more intuitive than the rate equation approach.

Computationally this scheme would not offer any increase in efficiency since the same equations are being calculated and compared to random numbers. However, it is a third method which yields the same results for the movement probabilities. This method is not easily extended to the full three-dimensional case mentioned earlier. The mathematical problem of determining the resistance between an interior point and any perimeter point on a complicated surface is presently unsolved. Even in cases of simple geometry and/or symmetry this is generally true.

5.8 SUMMARY

This chapter has dealt with extensive simulation results of the surface diffusion controlled decay of a corrugated surface at low temperature. The results show qualitative agreement with previous theoretical and experimental studies. The idealized system used could be extended to the high temperature region by including two effects: island nucleation and embedded terrace atom activation. The difficulties involved in extending the algorithm to three dimensions have been discussed and require some ingenuity to overcome.

An analytical treatment of the decay process was avoided for various reasons. Appropriate differential equations are difficult to formulate on a lattice. Even if this could be done, the random nature of the decay would be troublesome to take into account. Finally, no direct energy concepts such as surface energy or chemical potentials were used in the course of this work. Without these concepts, formulation of a driving force which would be necessary for a proper analytical treatment, might be impossible to achieve.

One area of possible future exploration using this algorithm might be to study film growth by applying the rules to deposited atoms. Quantities such as island size and density could be compared to other theoretical and experimental results of epitaxial growth. To obtain non layer-by-layer growth would require inclusion of island nucleation atop an existing island or the substrate. This would also necessitate extension to three dimensions. While not at all easy, this could prove useful, especially in light of the tremendous amount of work presently dealing with surface diffusion and various metal film growth modes.

CHAPTER 5 REFERENCES

BART93 N. C. Bartelt, J. L. Goldberg, T. L. Einstein, Ellen D. Williams, J. C. Heyraud, and J. J. Metois, Phys. Rev. B **48**, 15453 (1993).

BONZ84a H. P. Bonzel, E. Preuss, and B. Steffen, Appl. Phys. A **35**, 1 (1984).

BONZ84b H. P. Bonzel, E. Preuss, and B. Steffen, Surf. Sci. **145**, 20 (1984).

BOTT92 Michael Bott, Thomas Michely, and George Comsa, Surf. Sci. **272,** 161 (1992).

CHAN43 S. Chandrasekhar, Rev. Mod. Phys. **15**, 1 (1943), reprinted in *Selected Papers on Noise and Stochastic Processes,* edited by N. Wax, (Dover, New York, 1954).

CHAS91 E. Chason and B. W. Dodson, J. Vac. Sci. Technol. A **9**, 1545 (1991).

CHAW94 M. S. Chawla, M. Kalke, and M. A. Dubson, preprint, to appear in Phys. Rev. E (1994).

DOYL84 P. G. Doyle and J. L. Snell, *Random Walks and Electric Networks*, (The Mathematical Association of America, 1984).

DUBS94a M. A. Dubson and G. Jeffers, Phys. Rev. B **49**, 8347 (1994).

DUBS94b M. A. Dubson and E. Krastev, unpublished.

EHRL66a G. Ehrlich and F. G. Hudda, J. Chem. Phys. **44**, 1039 (1966).

EHRL66b G. Ehrlich, J. Chem. Phys. **44**, 1050 (1966).

FEYN63 R. P. Feynman, R. B. Leighton, and M. Sands, *The Feynman Lectures on Physics*, (Addison-Wesley, Reading, 1963), Volume I, Chapter 43.

FINK84 H. W. Fink and G. Ehrlich, Surf. Sci. **143**, 125 (1984).

GRUB67 E. E. Gruber and W. W. Mullins, J. Phys. Chem. Solids **28**, 875 (1967).

HERR51 C. Herring, Phys. Rev. **82**, 87 (1951).

HETH93 J. Hetherington (private communication).

HEYR87 J. C. Heyraud and J. J. Metois, J. Crystal Growth **82**, 269 (1987).

JIAN89 Z. Jiang and C. Ebner, Phys. Rev. B **40**, 316 (1989).

KEEF93 M. E. Keefe, C. C. Umbach, and J. M. Blakely, Bull. Am. Phys. Soc. **38**, (1) 567 (1993).

KUNK90 Ralf Kunkel, Bene Poelsema, Laurens K. Verheij, and George Comsa, Phys. Rev. Lett. **65**, 733 (1990).

LIU92 C. Liu and J. B. Adams, Surf. Sci. **265**, 262 (1992).

LIU93 C. Liu and J. B. Adams, Surf. Sci. **294**, 197 (1993).

METO87 J. J. Metois and J. C. Heyraud, Surf. Sci. **180**, 647 (1987).

METO89 J. J. Metois and J. C. Heyraud, Ultramicroscopy **31**, 73 (1989).

MULL59 W. W. Mullins, J. Appl. Phys. **30**, 77 (1959).

MULL63 W. W. Mullins, in *Metal Surfaces: Structure, Energetics, and Kinetics,* (American Society for Metals, Metals Park, Ohio, 1963), p. 17.

OZDE90 M. Ozdemir and A. Zangwill, Phys. Rev. B **42**, 5013 (1990).

PASH66 D. W. Pashley and M. J. Stowell, J. Vac. Sci. Technol. **3**, 156 (1966).

POEN92 M. Poensgen, J. F. Wolf, J. Frohn, M. Giesen, and H. Ibach, Surf. Sci. **274**, 430 (1992).

PREU86 E. Preuss, N. Freyer, and H. P. Bonzel, Appl. Phys. A **41**, 137 (1986).

RETT88 A. Rettori and J. Villain, J. Phys. France **49**, 257 (1988).

ROTT84 C. Rottman, M. Wortis, J. C. Heyraud, and J. J. Metois, Phys. Rev. Lett. **52** 1009 (1984).

SCHW66 Richard. L. Schwoebel and Edward. J. Shipsey, J. Appl. Phys. **37**, 3682 (1966).

SCHW69 Richard. L. Schwoebel, J. Appl. Phys. **40**, 614 (1969).

SELK93 W. Selke and T. Bieker, Surf. Sci. **281**, 163 (1993).

TSON72 Tien Tzou Tsong, Phys. Rev. B **6**, 417 (1972).

VANB87 H. van Beijeren and I. Nolden, in *Structure and Dynamics of Surfaces II,* edited by W. Schommers and P. von Blanckenhagen, (Springer-Verlag, Berlin, 1987).

WANG91 S. C. Wang and Gert Ehrlich, Phys. Rev. Lett. **67**, 2509 (1991).

WANG93a S. C. Wang and Gert Ehrlich, Phys. Rev. Lett. **70**, 41 (1993).

WANG93b S. C. Wang and Gert Ehrlich, Phys. Rev. Lett. **71**, 4174 (1993).

WEEK80 J. D. Weeks, in *Ordering in Strongly Fluctuating Condensed Matter Systems,* edited by T. Riste, (Plenum, New York, 1980), p. 293-317.

WILL91 Ellen D. Williams and N. C. Bartelt, Science **251**, 393 (1991).

WULF01 G. Wulff, Z. Krist. Mineral. **34**, 449 (1901).

YAMA81 K. Yamashita, H. P. Bonzel, and H. Ibach, Appl. Phys. **25**, 231 (1981).